SOME POTENTIAL APPLICATIONS OF DIGITAL IMAGE PROCESSING TECHNIQUES IN CLINICAL RADIOTHERAPY

by

Kurt B. Luchka

A Thesis

Submitted to the Faculty of Graduate Studies

in Partial Fulfillment of the Requirements

for the Degree of

MASTER OF SCIENCE

Department of Physics

University of Manitoba

Winnipeg, Manitoba

ISBN 0-612-13320-6

Canada

Name ____

Dissertation Abstracts International and *Masters Abstracts International* are arranged by broad, general subject categories. Please select the one subject which most nearly describes the content of your dissertation or thesis. Enter the corresponding four-digit code in the spaces provided.

Medical Biophysics

SUBJECT TERM

0760

SUBJECT CODE

UMI

Subject Categories

THE HUMANITIES AND SOCIAL SCIENCES

COMMUNICATIONS AND THE ARTS
Architecture 0729
Art History 0377
Cinema 0900
Dance 0378
Fine Arts 0357
Information Science 0723
Journalism 0391
Library Science 0399
Mass Communications 0708
Music 0413
Speech Communication 0459
Theater 0465

EDUCATION
General 0515
Administration 0514
Adult and Continuing 0516
Agricultural 0517
Art 0273
Bilingual and Multicultural 0282
Business 0688
Community College 0275
Curriculum and Instruction 0727
Early Childhood 0518
Elementary 0524
Finance 0277
Guidance and Counseling 0519
Health 0680
Higher 0745
History of 0520
Home Economics 0278
Industrial 0521
Language and Literature 0279
Mathematics 0280
Music 0522
Philosophy of 0998
Physical 0523
Psychology 0525
Reading 0535
Religious 0527
Sciences 0714
Secondary 0533
Social Sciences 0534
Sociology of 0340
Special 0529
Teacher Training 0530
Technology 0710
Tests and Measurements 0288
Vocational 0747

LANGUAGE, LITERATURE AND LINGUISTICS
Language
- General 0679
- Ancient 0289
- Linguistics 0290
- Modern 0291

Literature
- General 0401
- Classical 0294
- Comparative 0295
- Medieval 0297
- Modern 0298
- African 0316
- American 0591
- Asian 0305
- Canadian (English) 0352
- Canadian (French) 0355
- English 0593
- Germanic 0311
- Latin American 0312
- Middle Eastern 0315
- Romance 0313
- Slavic and East European 0314

PHILOSOPHY, RELIGION AND THEOLOGY
Philosophy 0422
Religion
- General 0318
- Biblical Studies 0321
- Clergy 0319
- History of 0320
- Philosophy of 0322

Theology 0469

SOCIAL SCIENCES
American Studies 0323
Anthropology
- Archaeology 0324
- Cultural 0326
- Physical 0327

Business Administration
- General 0310
- Accounting 0272
- Banking 0770
- Management 0454
- Marketing 0338

Canadian Studies 0385
Economics
- General 0501
- Agricultural 0503
- Commerce-Business 0505
- Finance 0508
- History 0509
- Labor 0510
- Theory 0511

Folklore 0358
Geography 0366
Gerontology 0351
History
- General 0578
- Ancient 0579
- Medieval 0581
- Modern 0582
- Black 0328
- African 0331
- Asia, Australia and Oceania 0332
- Canadian 0334
- European 0335
- Latin American 0336
- Middle Eastern 0333
- United States 0337

History of Science 0585
Law 0398
Political Science
- General 0615
- International Law and Relations 0616
- Public Administration 0617

Recreation 0814
Social Work 0452
Sociology
- General 0626
- Criminology and Penology 0627
- Demography 0938
- Ethnic and Racial Studies 0631
- Individual and Family Studies 0628
- Industrial and Labor Relations 0629
- Public and Social Welfare 0630
- Social Structure and Development 0700
- Theory and Methods 0344

Transportation 0709
Urban and Regional Planning 0999
Women's Studies 0453

THE SCIENCES AND ENGINEERING

BIOLOGICAL SCIENCES
Agriculture
- General 0473
- Agronomy 0285
- Animal Culture and Nutrition 0475
- Animal Pathology 0476
- Food Science and Technology 0359
- Forestry and Wildlife 0478
- Plant Culture 0479
- Plant Pathology 0480
- Plant Physiology 0817
- Range Management 0777
- Wood Technology 0746

Biology
- General 0306
- Anatomy 0287
- Biostatistics 0308
- Botany 0309
- Cell 0379
- Ecology 0329
- Entomology 0353
- Genetics 0369
- Limnology 0793
- Microbiology 0410
- Molecular 0307
- Neuroscience 0317
- Oceanography 0416
- Physiology 0433
- Radiation 0821
- Veterinary Science 0778
- Zoology 0472

Biophysics
- General 0786
- Medical 0760

EARTH SCIENCES
Biogeochemistry 0425
Geochemistry 0996
Geodesy 0370
Geology 0372
Geophysics 0373
Hydrology 0388
Mineralogy 0411
Paleobotany 0345
Paleoecology 0426
Paleontology 0418
Paleozoology 0985
Palynology 0427
Physical Geography 0368
Physical Oceanography 0415

HEALTH AND ENVIRONMENTAL SCIENCES
Environmental Sciences 0768
Health Sciences
- General 0566
- Audiology 0300
- Chemotherapy 0992
- Dentistry 0567
- Education 0350
- Hospital Management 0769
- Human Development 0758
- Immunology 0982
- Medicine and Surgery 0564
- Mental Health 0347
- Nursing 0569
- Nutrition 0570
- Obstetrics and Gynecology 0380
- Occupational Health and Therapy 0354
- Ophthalmology 0381
- Pathology 0571
- Pharmacology 0419
- Pharmacy 0572
- Physical Therapy 0382
- Public Health 0573
- Radiology 0574
- Recreation 0575
- Speech Pathology 0460
- Toxicology 0383

Home Economics 0386

PHYSICAL SCIENCES
Pure Sciences
Chemistry
- General 0485
- Agricultural 0749
- Analytical 0486
- Biochemistry 0487
- Inorganic 0488
- Nuclear 0738
- Organic 0490
- Pharmaceutical 0491
- Physical 0494
- Polymer 0495
- Radiation 0754

Mathematics 0405
Physics
- General 0605
- Acoustics 0986
- Astronomy and Astrophysics 0606
- Atmospheric Science 0608
- Atomic 0748
- Electronics and Electricity 0607
- Elementary Particles and High Energy 0798
- Fluid and Plasma 0759
- Molecular 0609
- Nuclear 0610
- Optics 0752
- Radiation 0756
- Solid State 0611

Statistics 0463

Applied Sciences
Applied Mechanics 0346
Computer Science 0984
Engineering
- General 0537
- Aerospace 0538
- Agricultural 0539
- Automotive 0540
- Biomedical 0541
- Chemical 0542
- Civil 0543
- Electronics and Electrical 0544
- Heat and Thermodynamics 0348
- Hydraulic 0545
- Industrial 0546
- Marine 0547
- Materials Science 0794
- Mechanical 0548
- Metallurgy 0743
- Mining 0551
- Nuclear 0552
- Packaging 0549
- Petroleum 0765
- Sanitary and Municipal 0554
- System Science 0790

Geotechnology 0428
Operations Research 0796
Plastics Technology 0795
Textile Technology 0994

PSYCHOLOGY
General 0621
Behavioral 0384
Clinical 0622
Developmental 0620
Experimental 0623
Industrial 0624
Personality 0625
Physiological 0989
Psychobiology 0349
Psychometrics 0632
Social 0451

Nom _____

Dissertation Abstracts International est organisé en catégories de sujets. Veuillez s.v.p. choisir le sujet qui décrit le mieux votre thèse et inscrivez le code numérique approprié dans l'espace réservé ci-dessous.

_____ ☐☐☐ U·M·I

SUJET — CODE DE SUJET

Catégories par sujets

HUMANITÉS ET SCIENCES SOCIALES

COMMUNICATIONS ET LES ARTS
Architecture 0729
Beaux-arts 0357
Bibliothéconomie 0399
Cinéma 0900
Communication verbale 0459
Communications 0708
Danse 0378
Histoire de l'art 0377
Journalisme 0391
Musique 0413
Sciences de l'information 0723
Théâtre 0465

ÉDUCATION
Généralités 515
Administration 0514
Art 0273
Collèges communautaires 0275
Commerce 0688
Économie domestique 0278
Éducation permanente 0516
Éducation préscolaire 0518
Éducation sanitaire 0680
Enseignement agricole 0517
Enseignement bilingue et multiculturel 0282
Enseignement industriel 0521
Enseignement primaire. 0524
Enseignement professionnel 0747
Enseignement religieux 0527
Enseignement secondaire 0533
Enseignement spécial 0529
Enseignement supérieur 0745
Évaluation 0288
Finances 0277
Formation des enseignants 0530
Histoire de l'éducation 0520
Langues et littérature 0279
Lecture 0535
Mathématiques 0280
Musique 0522
Orientation et consultation 0519
Philosophie de l'éducation 0998
Physique 0523
Programmes d'études et enseignement 0727
Psychologie 0525
Sciences 0714
Sciences sociales 0534
Sociologie de l'éducation 0340
Technologie 0710

LANGUE, LITTÉRATURE ET LINGUISTIQUE
Langues
- Généralités 0679
- Anciennes 0289
- Linguistique 0290
- Modernes 0291

Littérature
- Généralités 0401
- Anciennes 0294
- Comparée 0295
- Médiévale 0297
- Moderne 0298
- Africaine 0316
- Américaine 0591
- Anglaise 0593
- Asiatique 0305
- Canadienne (Anglaise) 0352
- Canadienne (Française) 0355
- Germanique 0311
- Latino-américaine 0312
- Moyen-orientale 0315
- Romane 0313
- Slave et est-européenne 0314

PHILOSOPHIE, RELIGION ET THÉOLOGIE
Philosophie 0422
Religion
- Généralités 0318
- Clergé 0319
- Études bibliques 0321
- Histoire des religions 0320
- Philosophie de la religion 0322

Théologie 0469

SCIENCES SOCIALES
Anthropologie
- Archéologie 0324
- Culturelle 0326
- Physique 0327

Droit 0398
Économie
- Généralités 0501
- Commerce-Affaires 0505
- Économie agricole 0503
- Économie du travail 0510
- Finances 0508
- Histoire 0509
- Théorie 0511

Études américaines 0323
Études canadiennes 0385
Études féministes 0453
Folklore 0358
Géographie 0366
Gérontologie 0351
Gestion des affaires
- Généralités 0310
- Administration 0454
- Banques 0770
- Comptabilité 0272
- Marketing 0338

Histoire
- Histoire générale 0578
- Ancienne 0579
- Médiévale 0581
- Moderne 0582
- Histoire des noirs 0328
- Africaine 0331
- Canadienne 0334
- États-Unis 0337
- Européenne 0335
- Moyen-orientale 0333
- Latino-américaine 0336
- Asie, Australie et Océanie 0332

Histoire des sciences 0585
Loisirs 0814
Planification urbaine et régionale 0999
Science politique
- Généralités 0615
- Administration publique 0617
- Droit et relations internationales 0616

Sociologie
- Généralités 0626
- Aide et bien-être social 0630
- Criminologie et établissements pénitentiaires 0627
- Démographie 0938
- Études de l' individu et de la famille 0628
- Études des relations interethniques et des relations raciales 0631
- Structure et développement social 0700
- Théorie et méthodes. 0344
- Travail et relations industrielles 0629

Transports 0709
Travail social 0452

SCIENCES ET INGÉNIERIE

SCIENCES BIOLOGIQUES
Agriculture
- Généralités 0473
- Agronomie. 0285
- Alimentation et technologie alimentaire 0359
- Culture 0479
- Élevage et alimentation 0475
- Exploitation des pâturages 0777
- Pathologie animale 0476
- Pathologie végétale 0480
- Physiologie végétale 0817
- Sylviculture et faune 0478
- Technologie du bois 0746

Biologie
- Généralités 0306
- Anatomie 0287
- Biologie (Statistiques) 0308
- Biologie moléculaire 0307
- Botanique 0309
- Cellule 0379
- Écologie 0329
- Entomologie 0353
- Génétique 0369
- Limnologie 0793
- Microbiologie 0410
- Neurologie 0317
- Océanographie 0416
- Physiologie 0433
- Radiation 0821
- Science vétérinaire 0778
- Zoologie 0472

Biophysique
- Généralités 0786
- Medicale 0760

SCIENCES DE LA TERRE
Biogéochimie 0425
Géochimie 0996
Géodésie 0370
Géographie physique 0368
Géologie 0372
Géophysique 0373
Hydrologie 0388
Minéralogie 0411
Océanographie physique 0415
Paléobotanique 0345
Paléoécologie 0426
Paléontologie 0418
Paléozoologie 0985
Palynologie 0427

SCIENCES DE LA SANTÉ ET DE L'ENVIRONNEMENT
Économie domestique 0386
Sciences de l'environnement 0768
Sciences de la santé
- Généralités 0566
- Administration des hôpitaux 0769
- Alimentation et nutrition 0570
- Audiologie 0300
- Chimiothérapie 0992
- Dentisterie 0567
- Développement humain 0758
- Enseignement 0350
- Immunologie 0982
- Loisirs 0575
- Médecine du travail et thérapie 0354
- Médecine et chirurgie 0564
- Obstétrique et gynécologie 0380
- Ophtalmologie 0381
- Orthophonie 0460
- Pathologie 0571
- Pharmacie 0572
- Pharmacologie 0419
- Physiothérapie 0382
- Radiologie 0574
- Santé mentale 0347
- Santé publique 0573
- Soins infirmiers 0569
- Toxicologie 0383

SCIENCES PHYSIQUES
Sciences Pures
Chimie
- Généralités 0485
- Biochimie 487
- Chimie agricole 0749
- Chimie analytique 0486
- Chimie minérale 0488
- Chimie nucléaire 0738
- Chimie organique 0490
- Chimie pharmaceutique 0491
- Physique 0494
- PolymÈres 0495
- Radiation 0754

Mathématiques 0405
Physique
- Généralités 0605
- Acoustique 0986
- Astronomie et astrophysique 0606
- Électronique et électricité 0607
- Fluides et plasma 0759
- Météorologie 0608
- Optique 0752
- Particules (Physique nucléaire) 0798
- Physique atomique 0748
- Physique de l'état solide 0611
- Physique moléculaire 0609
- Physique nucléaire 0610
- Radiation 0756

Statistiques 0463

Sciences Appliqués Et Technologie
Informatique 0984
Ingénierie
- Généralités 0537
- Agricole 0539
- Automobile 0540
- Biomédicale 0541
- Chaleur et thermodynamique 0348
- Conditionnement (Emballage) 0549
- Génie aérospatial 0538
- Génie chimique 0542
- Génie civil 0543
- Génie électronique et électrique 0544
- Génie industriel 0546
- Génie mécanique 0548
- Génie nucléaire 0552
- Ingénierie des systèmes 0790
- Mécanique navale 0547
- Métallurgie 0743
- Science des matériaux 0794
- Technique du pétrole 0765
- Technique minière 0551
- Techniques sanitaires et municipales 0554
- Technologie hydraulique 0545

Mécanique appliquée 0346
Géotechnologie 0428
Matières plastiques (Technologie) 0795
Recherche opérationnelle 0796
Textiles et tissus (Technologie) 0794

PSYCHOLOGIE
Généralités 0621
Personnalité 0625
Psychobiologie 0349
Psychologie clinique 0622
Psychologie du comportement 0384
Psychologie du développement 0620
Psychologie expérimentale 0623
Psychologie industrielle 0624
Psychologie physiologique 0989
Psychologie sociale 0451
Psychométrie 0632

SOME POTENTIAL APPLICATIONS OF DIGITAL IMAGE PROCESSING TECHNIQUES IN CLINICAL RADIOTHERAPY

BY

KURT B. LUCHKA

A Thesis submitted to the Faculty of Graduate Studies of the University of Manitoba in partial fulfillment of the requirements of the degree of

MASTER OF SCIENCE

Abstract

The main goal of external beam radiotherapy is the destruction of malignant tissue while minimizing the dosage to as much of the surrounding normal tissue as possible. Treatment verification is conventionally performed using film but more recently electronic portal imaging devices (EPIDs) have been used. The rapid availability of digital data associated with electronic images makes them ideal candidates for digital enhancement. This thesis investigates digital image processing techniques specialized for use on portal images. A composite enhancement technique called sequential processing has been optimized by considering characteristics common to portal images and the results show dramatic improvements in image quality. A pilot study was also conducted to determine the effectiveness of routine treatment verification on an obese patient undergoing radiation therapy for cancer of the cervix. It was found that setup displacements of 10 mm or greater were not uncommon and could easily be verified with the use of an EPID. Radio-opaque implanted markers have recently been used to help delineate boundaries of target tissues during radiotherapy. An algorithm has been developed which can detect the position of the markers with high precision and is perhaps the first step towards complete automation in treatment verification. Digital processing techniques can also be applied to simplify quality assurance procedures on treatment linacs. As an example, radiation light field congruence can be checked by acquiring an image of a specially designed test phantom. The results of a rigorous testing procedure indicate that this automated method has a submillimeter accuracy and is comparable to the conventional method.

Acknowledgments

The work presented in this thesis involved contributions from a number of people all of whom I would like to thank at this time.

Firstly, I would like to thank my supervisor Dr. Shlomo Shalev, who always had the time to answer my questions, no matter how absurd and to provide assistance with any problem, no matter how trivial. Never before has anyone worked so hard to make me successful.

Many thanks also go to my co-supervisor Dr. Richard Gordon, who introduced me to life outside of pure physics. Your enthusiasm and cheerfulness brightened many a day and will be fondly remembered.

I would also like to thank the other members of my examining committee, Drs. Samy El Sayed and Norm Davison for reading my thesis and providing their invaluable comments.

To my friends and colleagues, Drs. Georgi Gluhchev, Demeng Chen, Satyapal Rathee, John Lewis, Yuri Mandelzweig and David Viggars, the intellectually stimulating conversions we shared made it a pleasure to come to work each day.

Thanks to Dr. Rasika Rajapakshe, whose friendship and support throughout my program never wavered. Some of my most vivid memories are of the many good times we shared working on various projects over the past couple years.

Special thanks go to Brian Myslicki and Bob Miller who spent endless hours working with me on the linacs and to Randall Roels and Jim Fedorowich, who kept my computer working. I would also like to thank Ian Paul and Ed Maisey for their technical support throughout this project.

I would also like to thank, Heather Jory, Margaret Stewart, Chris Zeller, Julie Halfdanson, Karen Wedlake and the rest of the radiation therapists at the Manitoba Cancer Foundation for their assistance in this project.

Most of all I would like to thank my parents, Edward and Emily, who encouraged me to continue during times of crisis and who provided me with a stable foundation throughout my years. You have set the "gold standard" to which all parents are compared.

Table of Contents

Abstract ii

Acknowledgements iii

Table of Contents v

Chapter 1: The application of image processing in clinical radiotherapy

1.1 Main goal of radiotherapy 1

1.2 Analog and Digital Treatment Verification 5

1.3 The quality of portal images 8

1.4 Digital image processing techniques 13

1.5 Thesis overview 16

References 18

Figures 25

Chapter 2: A figure of merit for optimization of sequential processing

2.1 Introduction 33

2.2 Sequential processing 34

2.3 Figure of merit 36

2.4 FOM optimization for sequential processing 39

2.5 Clinically significant results 40

2.6 Conclusions 41

References 43

Chapter 2: (cont.)

Figures 45

Chapter 3: Pelvic irradiation of the obese patient: A treatment strategy involving megavoltage simulation and intra-treatment corrections

3.1. Introduction 50

3.2. Methods 51

3.2.1. Radiotherapy Prescription and Megavoltage Simulation 51

3.2.2. Intra-treatment Corrections 53

3.2.3. Image Calibration 54

3.2.4. Field Displacements 55

3.3. Results 56

3.3.1. Determination of the Action Level 56

3.3.2. Transverse Displacements (X_T vs. Z_T) in Course I 57

3.3.3. Transverse Displacements (X_T vs. Z_T) in Course II 59

3.3.4. Coronal Displacements (X_T vs. Y_T) in Course II 59

3.3.5. Saggital Displacements (Y_T vs. Z_T) in Course II 60

3.3.6. Consistency Tests 60

3.3.7. Measurement Error 61

3.3.8. Correction Error 63

3.3.9. Results of Corrective Intervention 63

3.3.10. Treatment Time 64

Chapter 3: (cont.)

3.4. Conclusions 64

Appendix 67

References 69

Tables 71

Figures 78

Chapter 4: Tumor localization through the detection of radio-opaque implanted markers

4.1 Introduction 90

4.2 Materials and methods 94

4.3 The marker detection algorithm 97

4.4 Results 101

4.4.1 Reproducibility 102

4.4.2 Marker Positional Accuracy 103

4.4.3 False Marker Detection 103

4.4.4 Clinically Significant Results 104

4.5 Conclusions 105

References 108

Tables 112

Figures 115

Chapter 5: Routine daily testing of radiation and light field congruence

5.1 Introduction 122

5.2 Materials and methods 124

5.3 Image analysis 125

5.3.1 Algorithm I 126

5.3.2 Algorithm II 128

5.4 Results 130

5.4.1 Reproducibility 130

5.4.2 Noise Sensitivity 131

5.4.3 Positional Accuracy 132

5.4.4 Daily Tests 133

5.4.5 The Conventional Film Method 134

5.5 Conclusions 135

References 136

Tables 138

Figures 141

Chapter 6: Summary 144

Chapter 1

The application of image processing in clinical radiotherapy

1.1 Main goal of radiotherapy

The main goal of external beam radiotherapy is the destruction of malignant tissue while minimizing the dosage to the surrounding normal tissue. This is accomplished during radiotherapy by delivering a dose of ionizing radiation to the diseased tissue. ICRU report 50[1] defines three specific target volumes which enable the definition of actual treated area. The first is called the gross tumor volume (GTV) and is defined by the extent of the clinically or radio-biologically detectable malignant growth. Unfortunately, a tumor mass does not have well defined borders and it often infiltrates the normal tissue in a complex manner. Therefore a second volume, called the clinical target volume (CTV) is defined as the volume containing the GTV and all subclinical microscopic malignancies which must be eliminated. The third volume is called the planning target volume (PTV) and is defined by considering the net effect of all possible geometric uncertainties that may occur during delivery of the treatment, such as organ movement, tissue variation in size and shape, patient movement and setup inaccuracies. To account for these uncertainties, the PTV is made geometrically larger than the CTV to ensure that the target receives the prescribed dose during treatment. However, the size of the margin is limited by the radiation tolerance of the surrounding normal tissue and must be set to some acceptable size.

A typical tumor mass consists of a spheroidal conglomeration of cells which are characterized by their abnormally rapid doubling time. The mass of cells may contain a

necrotic center surrounded by a region of hypoxic cells and a thin outer layer of well oxygenated cells.

The destructive effect of photon radiation originates in its ability to ionize atoms in the diseased tissue. The ionized atoms undergo chemical reactions with H_2O molecules in the cells to form hydroxyl free radicals. The hydroxyl radicals interact with a cell's DNA ultimately impeding its clonogenic ability. The effects of oxygen concentration on irradiated cells have been studied in vitro[2,3] and the cell survival curves comparing hypoxic and aerated tissue irradiated with x-ray photons show a marked difference as shown in Fig. 1-1. The hypoxic core of the tumor is much less sensitive to ionizing radiation producing a serious problem as the target volume may contain both aerated normal and hypoxic diseased tissue.

The increased resistance of the diseased tissue to ionizing radiation is lessened by applying the radiation in fractionated doses[4]. The effect of fractionation is shown in Fig. 1-2 where the rest period between dose fractions allows the lethally exposed cells at the periphery of the tumor to be flushed away, the intermediate region of hypoxic cells to become aerated and sublethal damage incurred in the normal tissue to be repaired therefore improving the probability of tumor cure and ensuring viability and prolonged survival of the surrounding normal tissue. However, increasing the number of fractionated doses in a treatment requires that each delivered dose be reproducible and accurately aligned to the prescribed target volume on each treatment day.

A fractionated radiotherapy treatment may consist of 20-30 individual fractions spread out over several weeks. During this period, a number of situations can arise that compromise the geometric accuracy of target volume irradiation and hence alter the dose distribution to the tumor volume and surrounding normal tissue. On any particular day,

field placement errors may occur due to incorrect alignment of the treatment beam to the target volume. The patient may also gain or lose weight as the treatment progresses while skin marks, used for alignment in the treatment beam, were set at or just prior to the first treatment fraction. The underlying bony anatomy of the patient shifting with respect to the skin marks is a problem that often occurs in obese patients and in target sites where organs may vary in size due to rectal or bladder filling. Machine parameter errors also occur such as misalignment between the radiation and light field, deviations in back pointer and laser alignment and asymmetry in gantry and collimator rotation to name a few and are a result of limited mechanical tolerances of the treatment machines. Accuracy is also reduced by human error, an example of which is incorrectly placed or missing shielding blocks and improper collimator or timer settings. All of these factors lead to a change in the dose distribution to the target volume the result of which has been shown to decrease local tumor control[5,6] and increase normal tissue complication[7]. Studies conducted to determine the precision required in dose delivery[8,9] have prompted ICRU report 24[10] to conclude that dose distributions to the target volume must be no larger than ±5% if the desired result is eradication of the primary tumor.

The effectiveness of a radiotherapy treatment depends on whether the target volume was adequately covered therefore field placement and gross errors pose a major problem as they can adversely affect the outcome of the treatment[11,12]. A substantial reduction in the number of field placement errors has been demonstrated[13-17] by introducing regular treatment verification using portal film or electronic portal imaging devices (EPIDs).

It is desirable to deliver higher doses of radiation to the tumor volume and to reduce margins through the application of conformal beams[18,19] or dynamic arc treatments, where the collimator jaws or multileaf collimators conform to the target volume as the beam orientation changes with respect to the patient during irradiation. Adaptations of

conventional therapy may also be attempted as a recent study by Yan et al.[20] suggests. This study focuses on altering the treatment plan by monitoring setup error for each individual patient. Feedback from the initial few fractions is used to predict the systematic and random field displacements for a particular patient. This information is used to score the therapeutic gain of the initial treatment plan by considering the normal tissue complication probability (NTCP) and tumor control probability (TCP). The therapeutic gain is then optimized by reducing field margins and escalating tumor dose whenever possible resulting in greater tumor control while limiting normal tissue damage. Although patient setup is not adjusted, routine treatment verification is necessary to classify setup displacement errors which ultimately determines the most suitable course of action to be taken.

Treatment verification has been shown to be useful in reducing field placement as well as gross errors encountered in conventional radiotherapy. It has become apparent that treatment verification is essential with the development of new more sophisticated treatment techniques. Conventional analog methods of monitoring treatment accuracy are cumbersome and impractical to be used on a routine basis while EPIDs offer a convenient and reliable means to do this. As with portal films, electronic portal images suffer from poor contrast and low spatial resolution which make analysis difficult. Since electronic images are stored in digital form, digital image processing techniques can be used to extract the most information possible out of an image. With smaller margins and dynamically changing fields, less anatomical information is situated inside the treatment field and therefore enhancement becomes as essential as routine verification itself.

1.2 Analog and Digital Treatment Verification

Portal film verification is, at present, the method of choice to verify patient setup accuracy at most centers. A single emulsion photographic film is placed in contact with a metal screen and both are exposed to the megavoltage beam that passes through the patient. High energy photons strike the metal plate and are converted to electrons which subsequently track into the film and form a projection image of the patient's anatomy contained within the treatment port.

There are three commonly used types of portal film radiographs called localization, verification and double exposure films[21] and all can be used to verify patient position as well as being a permanent record of the treatment.

A "localization film" is a highly sensitive film that forms an image by exposure to a small fraction of the daily treatment dose. Once the film has been exposed, the treatment is stopped and the film is developed and analyzed for field placement or gross errors, allowing setup correction before completion of the treatment. However, the procedure of exposing, developing and analyzing a localization film is time consuming and makes this technique unsuitable for routine daily monitoring of patient setup.

A "verification film" is a less sensitive film that forms an image by exposure to the entire treatment dose. The film is then processed and analyzed for field placement or gross errors prior to the next treatment fraction. This technique is less time consuming than localization films, as verification films may be developed and analyzed before the next treatment. However verification films do not allow the immediate detection of field placement or gross errors and corrections to patient set up, if required, can only be applied prior to the following treatment.

A "double exposure film" is similar to a localization film in that it uses a very sensitive film but images are formed by applying two short exposures of the treatment beam. The first exposure is formed with a small fraction of the treatment dose on a large unblocked field, thereby deliberately exposing parts of the patient's anatomy outside of the target volume. The second exposure is taken with the prescribed field settings, including blocks, wedges and compensators and is superimposed on the image formed by the first exposure. The advantage of a double exposure film is that surrounding parts of the patient's anatomy can be identified with respect to the prescribed field. Double exposure films may be necessary for small fields containing little anatomical information useful for determining patient position. However, double exposure films create the greatest work load for the therapists and, like localization films, they are rarely used to correct patient setup except during the first fraction.

Portal film verification is expensive in human and material resources, and has limited value as a treatment verification tool due to the lengthy periods of time (>15 min.) required to process and analyze a film. Ideally, films should be acquired and analyzed for every field of every fraction of treatment but the delays caused by film development and analysis would require the patient to remain absolutely stationary for lengthy periods of time as well as substantially increasing the treatment time and introducing an increased workload to the therapists. Therefore it is common practice to verify the first fraction and possibly one on a weekly basis thereafter during the remainder of the treatment. Mitine et al.[22] compared acceptable first treatment session portal films for 10 head & neck patients to port films acquired during ensuing treatment fractions. The results indicate that on average about 20% of the following fractions showed unacceptable displacements (>5 mm) when compared to the simulator film reference.

To address the problems associated with analog film verification, a variety of EPIDs have been developed[23,24] which facilitate routine monitoring of patient treatments. Video based electronic portal imaging devices (VEPIDs), shown in Fig. 1-3, are the most common[25-27] and although video cameras or phosphor screens may differ, their basic structural design is the same. The x-ray photons transmitted through the patient strike the metal plate and produce high energy electrons which track into the phosphor backing. Collisional interactions between the secondary electrons and phosphor lattice produce a visible projection image of the patient's anatomy contained within the treatment port which is viewed by a video camera through a 45° front surface mirror. The video signal from the camera is digitized and an image is displayed on a monitor. The advantage VEPIDs have over film is their ability to produce acceptable quality portal images that can be viewed in near real time with a fraction of the daily dose of radiation. The ability to display an image in near real time allows immediate corrective intervention to those treatment fractions with unacceptable setup displacements or gross errors. Several studies have used VEPIDs to correct patient setup position and the results show definite improvements to overall treatment accuracy[28-31].

The purpose of monitoring patient setup is to reduce the number and magnitude of field placement errors with the intent to preserve the prescribed dose distribution to the target volume. Images or films acquired of a treatment port can be compared to a simulator film and corrective intervention can be applied in one of two ways as shown in Fig. 1-4.

With the intra-treatment correction technique, an image or film is acquired with a fraction of the daily dose, at which time the treatment is stopped. The image is compared to a simulator film and a decision is made as to the accuracy of patient setup. If the setup is deemed acceptable, the remainder of the treatment dose is delivered. If the setup is

deemed unacceptable, the patient is repositioned in the treatment beam and a second image is acquired.

With the inter-treatment correction technique, an image or film is acquired with the entire daily dose and if the patient setup is deemed unacceptable, a correction is made at the start of the next treatment. This is the common approach taken at those centers that use film to verify patient setup.

If VEPIDs are to replace film as the conventional means of treatment verification, the quality of digital portal images must be as good or better than analog images acquired on film. Digital and analog portal images share many of the same qualities both of which are infamous for having poor contrast and low spatial resolution. Contrast enhancement of portal films by gamma multiplication[32] has been shown to improve contrast in portal films but the additional processing time required makes this technique of little value if intra-treatment intervention is desired. The availability of digital electronic images, however, allows rapid contrast enhancement using techniques ideally suited to implementation on a personal computer. Although portal films can be digitized and enhanced[34-36] much the same way as electronic portal images, the digitization process adds yet another step in the already lengthy chain of procedures associated with film. The advantage of digital data, intrinsic to the electronic images, is that it can be easily accessed and processed within seconds after image acquisition.

1.3 The quality of portal images

Portal films and electronic portal images both suffer from poor image quality which can be attributed to a number of factors. In the range 1 to 10 MeV, x-ray attenuation in bone and soft tissue is proportional to the electron density of the scattering medium as the

dominant mode of interaction is Compton scattering. Photoelectric interactions dominate at diagnostic energies where attenuation is proportional to the cube of the atomic number. Therefore bone and soft tissue, having relatively similar electron densities ($\rho_e \approx 3 \times 10^{23}$ e/g)[36], are difficult to differentiate in portal images whereas at diagnostic energies, bone ($Z \approx 12$) and soft tissue ($Z \approx 7$) are easily discernible, having linear attenuation coefficients of 0.25 and 0.60 cm^{-1} respectively[37].

Webb[38] has modeled radiographic contrast using the simple geometry shown in Fig. 1-5. An anatomical structure with attenuation coefficient μ_2 and thickness x is embedded in a uniform block of tissue, with linear attenuation coefficient μ_1. Point source x-rays are incident normally to the surface of the block. If I_1 and I_2 are the x-ray exit fluences along line A and B respectively, then radiographic contrast is given by,

$$C = \frac{1 - e^{-(\mu_2 - \mu_1)x}}{1 + SPR} \tag{1}$$

where SPR is the ratio of scattered to primary x-ray flux. The SPR has been found to be a complicated function of energy through the diagnostic and megavoltage energy range[39-41]. Contrast at megavoltage energies is degraded due to the strong forward scattering of photons of higher energy that easily penetrate the block of tissue. For simplicity, in the following only the primary component of transmitted x-ray fluence will be considered by setting $SPR = 0$ in Eqn. (1) resulting in an equation for primary contrast given by,

$$C_p = 1 - e^{-(\mu_2 - \mu_1)x} \tag{2}$$

Figure 1-6 shows a plot comparing primary contrasts of bone and air embedded in a block of soft tissue as a function of energy as calculated from Eqn. (2). The linear attenuation

coefficient data for bone, air and soft tissue used in Fig. 1-6 were taken from Attix[36]. Figure 1-6 shows that contrast is reduced by a factor of three as incident photon energy is increased from 100 keV to 1 MeV. Figure 1-7a is a diagnostic energy x-ray film acquired at a x-ray tube voltage of 75 kVp and shows the prescribed target volume for a 37 year old male being treated for Hodgkin's disease of the nasopharynx and cervical nodes. Figure 1-7b shows the corresponding treatment image acquired at an energy of 6 MV where the decrease in contrast is quite evident.

Image blurring associated with a large source size also contributes to a degradation of image quality by decreasing spatial resolution. Medical accelerators have a finite source size[42-44] but this problem is most apparent in ^{60}Co treatment machines due to the large amount of isotope and therefore large source size required to produce a clinically suitable dose rate. Figure 1-8 is a schematic diagram showing how the finite source size effects the spatial resolution in the detector plane. A point P in the patient plane is imaged by a finite source of width a, where d_1 and d_2 are the distances between the three planes as shown in Fig. 1-8. The point P will be projected onto the detector plane with a finite size P' given by,

$$P' = a\frac{d_2}{d_1} \tag{3}$$

The geometric unsharpness described by Eqn. (3) is called image penumbra and has the effect of blurring anatomical structures as well as field edges in portal images. The source size is dependent on the design of the medical accelerator or ^{60}Co unit and clinically useful source to axis (SAD) distances are usually fixed between 80 and 100 cm. Therefore the only way that the penumbra can be reduced is by placing the detector plane

as close as possible to the patient plane but this reduces magnification resulting in a loss of spatial resolution in a portal image.

Other factors also effect spatial resolution in portal images such as patient movement during image acquisition which, in some cases cannot be avoided, an example being movement of the lungs during a long film exposure. It has also been found[45] that resolution is limited by the type of phosphor screen used in the detector of an VEPID.

A large contributing factor to poor image quality is simply poor acquisition technique. Over or under exposure of portal film reduces the amount of anatomical information recorded on a film whereas for a VEPID, improper camera or frame grabber setting can lead to suboptimal imaging performance. Proper film exposure is a difficult problem to overcome because of the variety of sites and patient separations encountered in radiotherapy, the optimal settings for good quality films being different for every patient. A similar problem exists in electronic portal imaging where camera gain and offset must be optimized for each patient to get adequate image quality although this limitation can be overcome by increasing the pixel depth of the standard 8 bit A/D converters to 10 or 12 bits.

Random noise also contributes to the poor quality of portal images by decreasing the perceptibility of fine detail making visualization of anatomical details difficult. Portal films demonstrate x-ray mottle resulting from the statistical nature of the incident x-ray flux. VEPIDs are effected by quantum and electronic noise. Quantum noise is similar to x-ray mottle in that it arises due to the statistical nature of the incident x-rays but also includes the conversion of x-rays to light in the metal / phosphor detector and image formation on the target of the video camera. Electronic noise arises in the circuits of the

video camera as well as all the other electronic components which is passed down the imaging chain and adds noise to the image.

All of these factors degrade the quality of megavoltage images and reduce the accuracy with which patient setups can be evaluated. Direct access to digital data from an electronic portal image or indirectly from digitization of a film, allows contrast enhancement using any of a number of standard image processing techniques. Of course electronic images have a distinct advantage over film as digital data is accessible immediately after acquisition of the image. Nevertheless, both electronic and film images may be processed to increase the perceptibility of pictorial information thus making detection of field placement errors much easier for the viewer to discern.

The need for image processing in clinical radiotherapy is not only limited to the enhancement of poor quality portal images. Image processing techniques are useful in reducing the workload of routine quality assurance procedures performed on the treatment accelerators, one example being the radiation light field congruence test. Conventionally, the congruence test consists of placing a portal film at isocenter in the beam path and imprinting the radiation and light field directly on the film. After processing and mapping of the 50% dose contour, field coincidence is judged by visual inspection of the film. This highly qualitative procedure is time consuming and results can vary depending on the experience of the dosimetrist. Digital image processing techniques can be applied to electronic images of the radiation and light field, determining coincidence automatically and significantly reducing the workload of the dosimetrist.

1.4 Digital image processing techniques

Portal images are subject to poor contrast, low spatial resolution and high levels of noise. Therefore, the most common digital image processing techniques applied to portal images are contrast enhancement, image sharpening and noise reduction.

Digital contrast enhancement techniques, in general, remap pixel intensities of an original image with the intent to increase contrast in the processed image. This may be achieved simply by windowing the pixel intensities in an image or by applying more sophisticated procedures such as global or adaptive histogram equalizations.

The global histogram equalization method remaps pixels using a transformation function derived from the gray level distribution over an entire image[46]. This technique has found limited use in the enhancement of portal images as it is usually desired to enhance contrast over small areas within the treatment portal. These small neighborhoods will have little influence on the determination of the global transformation function while the large background found outside the treatment portal contributes substantially to the transformation function. Therefore contrast enhancement at the desired location inside the field is not guaranteed.

A variety of adaptive histogram equalization methods attempt to correct this problem. In particular, local histogram equalization[46] (LHE) determines a transformation function for each pixel in an image by considering only those pixels in a small neighborhood about each pixel. Remapped pixels show much better contrast as only local regions contribute to the transformation function while distant pixels outside the region have no effect. Although this method performs well on portal images, it is computationally expensive and tends to over-enhance noise in homogeneous regions of the image.

To overcome the computational burden of LHE, Pizer et al[47] have developed an interpolated adaptive technique that generates transformation functions at regular grid points in an image. Pixels in the image are then remapped by interpolating the transformations from the four nearest grid points surrounding the pixel. This method produces a considerable time saving as the number of transformation functions that have to be calculated is dramatically reduced. Although this method speeds up the time required to process an image, it is still sensitive to noise and has prompted the development of a contrast limited adaptive histogram equalization[47] (CLAHE).

In CLAHE, contrast enhancement is limited by restricting the slope of the cumulative distribution function (CDF). The histogram of the image is simply the derivative of the CDF, therefore limiting the slope of the CDF is equivalent to clipping the height of the histogram. Large peaks in a histogram are associated with large uniform areas of similar intensity in an image. Standard AHE maps these relatively small peaks in the histogram to a wide range of output values and therefore has a tendency to over-enhance noise. CLAHE limits the intensity range over which these pixels can be displayed, therefore limiting the enhancement of noise in the image. While CLAHE is a definite improvement over the standard AHE techniques in terms of speed and image quality, it causes field edges to be blurred in portal images. This is an undesirable side effect as treatment verification relies on the position of anatomical landmarks in relation to the field edge.

Leszczynski et al.[48] have developed a selective contrast limited adaptive histogram equalization (SCLAHE) technique that eliminates the blurring of field edges caused by CLAHE. In the SCLAHE method, the field edge of the treatment image is detected and only those pixels that lie inside the field are processed via the CLAHE technique.

Due to the high levels of noise found in portal images, it is often desirable to reduce noise by applying a smoothing filter in the spatial domain. Linear spatial noise reduction techniques[46,49] alter intensity variations in an image by determining a weighted average over a small predefined convolution mask for each pixel in an image. The mask weights for a mean filter are all unity, while mask weighting for Gaussian filters is determined by sampling the distribution of a Gaussian which has parameters specified by the user. One of the problems associated with linear smoothing operations is the edge blurring they induce. This problem can be overcome with the use of the non-linear median filter. A median filter replaces the gray level intensity of a pixel with the median intensity found from the pixels in a small surrounding neighborhood. The main benefit of the median filter is it's ability to reduce salt and pepper noise while preserving edges in an image. This make median filters particularly useful in reducing noise in portal images as the field edges are preserved.

Due to the low spatial resolution found in portal images, it is often beneficial to sharpen an image to improve it's quality. Spatial sharpening filters can be applied in much the same way as smoothing filters but instead of reducing the high frequency components in an image, the low frequency components are suppressed. The objective of sharpening is to improve the visibility of fine detail in an image or enhance detail that has been blurred. All high frequency components in an image will be enhanced, including noise, therefore sharpening filters have found limited use for processing of raw portal images. In combination with other techniques such as smoothing and SCLAHE, sharpening filters have shown good results in the enhancement of fine anatomical details in a portal image.

A composite enhancement technique is currently under development[50,51] which consists of applying the combination of SCLAHE, median filtration and edge sharpening. This

method, called sequential processing, has been found to perform better than any of the previously described methods mainly due to it's ability to reduce noise in the image while preserving edges which are subsequently sharpened with a custom filter.

1.5 Thesis overview

The sequential processing technique is described in chapter 2 and a figure of merit (*FOM*) is introduced to optimize the parameters of this technique for portal images. The *FOM* is formed by considering characteristics common to portal images such as spatial resolution and contrast to noise ratio (*CNR*). Enhancement parameters such as mask size and clipping level were then adjusted to optimize the *FOM*.

Chapter 3 analyzes the application of intra-treatment corrections to the treatment of an obese patient for whom setup by skin marks was impractical. The delivery of the treatment was further complicated as the patient could not be simulated in the conventional sense due to weight restrictions on the simulator couch. An VEPID was used to acquire a megavoltage "simulation image" of the patient during the first treatment fraction. All subsequent treatment fractions were compared to the "simulation image" and adjustments to patient set up were made, if necessary.

Chapter 4 describes a digital image processing algorithm that has been developed for detecting radio-opaque markers in megavoltage portal images. A phantom was constructed into which the markers were embedded and treatment conditions were simulated by enclosing the phantom in a tissue equivalent buildup material. A range of phantom images were acquired with different doses of radiation and each was analyzed for accuracy in marker location using a computer algorithm designed specially for this purpose.

Chapter 5 describes a method to test radiation light field congruence of treatment accelerators. This method consists of aligning a specially designed test phantom in the light field of a treatment linac and acquiring an electronic portal image. A computer program then automatically analyzes the image and determines the degree of congruence between the two fields. The final result of the test is a "**go**", "**warning**" or "**no go**" decision depending on the extent of misalignment between the light and radiation fields.

To conclude, a summary of the results is given in chapter 6.

References

1. ICRU Report 50, *Prescribing, Recording, and Reporting Photon Beam Therapy*, (International Commission on Radiation Units and Measures, Washington, D.C., 1992).

2. G. W. Barendsen, C. J. Koot, Kersen G.R., D. K. Bewley, S. B. Field and C. J. Parnell, "The effect of oxygen on impairment of the proliferative capacity of human cells in culture by ionizing radiations of different LET," Int. J. Rad. Biol. **10,** 317-27 (1966).

3. J. J. Broerse, G. W. Barendsen and Kersen G.R., "Survival of cultured human cells after irradiation with fast neutrons of different energies in hypoxic and oxygenated conditions," Int. J. Radiat. Biol. **13,** 559-72 (1967).

4. E. J. Hall, *Radiobiology for the radiologist, Fourth Edition,* (J.B. Lippincott Company, Philadelphia, 1994).

5. M. Goitein and J. Busse, "Immobilization error: Some theoretical considerations," Radiology **177,** 407-12 (1975).

6. A. Dutreix, "When and how can we improve precision in radiotherapy," Radiother. Oncol. **2,** 275-92 (1984).

7. K. Mah, J. VanDyk, T. Keane and P. Y. Poon, "Acute radiation-induced pulmonary damage: A clinical study on the response to fractionated radiation therapy," Int. J. Radiat. Oncol. Biol. Phys **13,** 179-88 (1987).

8. J. G. Stewart and A. W. Jackson, "The steepness of the dose response curve both for tumor cure and normal tissue injury," Laryngoscope **85,** 1107 (1975).

9. P. Svensson, P. Westling and L. G. Larsson, "Radiation-induced lesions of the brachial plexus correlated to the dose-time-fraction schedule," Acta Radiol. **14,** 288 (1975).

10. ICRU Report 24, *Determination of absorbed dose in a patient irradiated by beams of X or Gamma rays in radiotherapy procedures*, (International Commission on Radiation Units and Measurements, Washington, D.C., 1976).

11. J. E. Marks, A. G. Haus, H. G. Sutton and M. L. Griem, "Localization error in the radiotherapy of hodgkin's disease and malignant lymphoma with extended mantle fields," Cancer **34,** 83-90 (1974).

12. J. E. White, T. Chen, J. McCracken, P. Kennedy, H. G. Seydel, G. Hartman, J. Mira, M. Khan, F. Y. Durance and O. Skinner, "The influence of radiation therapy quality control on survival, response and sites of relapse in oat cell carcinoma of the lung," Cancer **50,** 1084-90 (1982).

13. R. W. Byhardt, J. D. Cox, A. Hornburg and G. Liermann, "Weekly localization films and detection of field placement errors," Int. J. Radiat. Oncol. Biol. Phys. **4,** 881-87 (1978).

14. I. Rabinowitz, J. Broomberg, M. Goitein, K. McCarthy and J. Leong, "Accuracy of radiation field alignment in clinical practice," Int. J. Radiat. Oncol. Biol. Phys. **11,** 1857-67 (1985).

15. H. Huizenga, P. C. Levendag, P. M. Z.R. De Porre and A. G. Visser, "Accuracy in radiation field alignment in head and neck cancer: A prospective study," Radiother. Oncol. **11,** 181-87 (1988).

16. S. E. Griffiths, G. G. Khoury and A. Eddy, "Quality control of radiotherapy during pelvic irradiation," Radiother. Oncol. **20,** 203-6 (1991).

17. J. E. Marks, A. G. Haus, H. G. Sutton and M. L. Griem, "The value of frequent treatment verification films in reducing localization error in the irradiation of complex fields," Cancer **37,** 2755-61 (1976).

18. H. D. Suit, J. Becht, J. Leong, M. Stracher, W. C. Wood, L. Verhey and M. Goitein, "Potential for improvement in radiation therapy," Int. J. Radiat. Oncol. Biol. Phys. **14,** 777-86 (1988).

19. J. P. Gerard, "High dose-high precision in radiation oncology," Radiother. Oncol. **29,** 167-8 (1993).

20. D. Yan, J. Wong, J. Michalski, C. Pan, A. Frazier, W. Bosch and A. Martinez, "Inter-treatment compensation of treatment setup variation to enhance the radiotherapeutic ratio", Proceedings of the 37th Annual ASTRO Meeting, 1995.

21. L. E. Reinstein, H. I. Amols, P. J. Biggs, R. T. Droege, A. B. Filimonov, W. R. Lutz and S. Shalev, *Radiotherapy portal imaging quality: Report of AAPM task group No. 28,* (American Institute of Physics, New York, 1988).

22. C. Mitine, G. Leunens, J. Verstraete, N. Blanckaert, J. Van Dam, A. Dutreix and E. van der Schueren, "Is it necessary to repeat quality control procedures for head and neck patients?," Radiother. oncol. **21,** 201-10 (1991).

23. A. L. Boyer, L. Antonuk, M. Van Herk, H. Meertens, P. Munro, L. E. Reinstein and J. Wong, "A review of electronic portal imaging devices (EPIDS)," Med. Phys. **19,** 1-16 (1992).

24. P. Munro, "Portal imaging technology: Past present and future," Seminars in Radiation Oncology **5,** 115-33 (1995).

25. P. Munro, J. Rawlingson and A. Fenster, "A digital fluoroscopic imaging device for radiotherapy localization," Int. J. Radiother. Oncol. Biol. Phys. **18,** 641-49 (1990).

26. A. Visser, H. Huizenga, V. Althof and B. Swanenberg, "Performance of a prototype fluoroscopic radiotherapy imaging system," Int. J. Radiother. Oncol. Biol. Phys. **18,** 43-50 (1990).

27. S. Shalev, T. Lee, K. Leszczynski, S. Cosby, T. Chu, L. Reinstein and A. Meek, "Video techniques for on-line portal imaging," Computerized Medical Imaging and Graphics **13,** 217-226 (1989).

28. L. Cionini and M. Bucciolini, "Role of portal imaging in clinical radiotherapy: Florence experience," Radiother. Oncol. **29,** 230-36 (1993).

29. A. A. H. El-Gayed, A. Bel, R. Vijlbrief, H. Bartelink and J. V. Lebesque, "Time trend of patient setup deviations during pelvic irradiation using electronic portal imaging," Radiother. Oncol. **26,** 162-71 (1993).

30. W. De Neve, F. van den Heuvel, M. Coghe, D. Verellen, M. De Beukeleer, A. Roelstraete, P. De Roover, L. Thon and G. Storme, "Interactive use of on-line portal imaging in pelvic radiation," Int. J. Radiat. Oncol. Biol. Phys. **25,** 517-524 (1993).

31. C. L. Creutzberg, G. M. Althof, H. Huizenga, A. G. Visser and P. C. Levendag, "Quality assurance using portal imaging: The accuracy of patient positioning in irradiation of breast cancer," Int. J. Radiat. Oncol. Biol. Phys. **25,** 529-539 (1993).

32. L. E. Reinstein and C. G. Orton, "Contrast enhancement of high-energy radiotherapy films," B.J.R. **52,** 880-887 (1979).

33. I. Crooks and B. G. Fallone, "PC-based selective histogram equalization for contrast enhancement of portal films," Med. Phys. **18,** 618 (1991).

34. G. W. Sherouse, J. Rosenman, H. L. McMurray, S. M. Pizer and E. L. Chaney, "Automatic digital contrast enhancement of radiotherapy films," Int. J. Radiat. Oncol. Biol. Phys. **13,** (1987).

35. J. Leong, "A digital image processing system for high energy x-ray portal images," Phys. Med. Biol. **29,** 1527-1535 (1984).

36. Frank H. Attix, *Introduction to Radiological Physics and Radiation Dosimetry,* (John Wiley & Sons, New York, 1986).

37. H. E. Johns and J. H. Cunningham, *The Physics of Radiology,* (Charkes C Thomas Publishers, Springfield, 1969).

38. S. Webb, *The physics of medical imaging,* (The Bath Press, Avon, Great Britain, 1988).

39. D. A. Jaffray, J. J. Battista, A. Fenster and P. Munro, "X-ray scatter in megavoltage transmission radiography: Physical characteristics and influence on image quality," Med Phys. **21,** 45-60 (1994).

40. W. Swindell, E. J. Morton, P. M. Evans and D. G. Lewis, "The design of megavoltage projection imaging systems: Some theoretical aspects," Med. Phys. **18,** 1-16 (1991).

41. S. W. Smith and R. A. Kruger, "A signal processing model of diagnostic x-ray scatter," Med. Phys. **13,** 831-835 (1986).

42. D. Jaffray, J. Battista, A. Fenster and P. Munro, "X-ray sources of medical linear accelerators: Focal and extra-focal radiation," Med. Phys. **20,** 1417-1427 (1993).

43. E. Loewenthal, E. Loewinger, E. Bar-Avraham and G. Barnea, "Measurement of the source size of a 6- and 18-MV radiotherapy linac," Med. Phys. **19,** 687-690 (1992).

44. P. Munro, J. Rawlinson and A. Fenster, "Therapy imaging: source sizes of radiotherapy beams," Med. Phys. **15,** 517-24 (1988).

45. B. Wowk and S. Shalev, "Thick phosphor screens for on-line portal imaging," Med. Phys. **21,** 1269-1276 (1994).

46. W. K. Pratt, *Digital image processing,* (Wiley, New York, 1991).

47. S. M. Pizer, E. P. Amburn, J. D. Austin, R. Cromartie, A. Geselowitz, T. Greer, B. Romeny, J. B. Zimmerman and K. Zuiderveld, "Adaptive histogram equalization and its variations," Comput. Vision Graphics Image Process **39,** 355-368 (1987).

48. K. Leszczynski, S. Shalev and S. Cosby, "The enhancement of radiotherapy verification images by an automated edge detection technique," Med. Phys. **19,** 611-622 (1992).

49. R. C. Gonzalez and R. E. Woods, *Digital Image Processing,* (Addison-Wesley Publishing Company, New York, 1992).

50. G. Gluhchev and S. Shalev, "Combined approach for portal image enhancement", Proc. of European Congress of Medical Physics, Tenerife, 1993.

51. G. Gluhchev and S. Shalev, "Portal image enhancement: A comparison of techniques", The 3rd International Workshop on Electronic Portal Imaging: Clinical Applications of Electronic Portal Imaging, San Francisco, 1994.

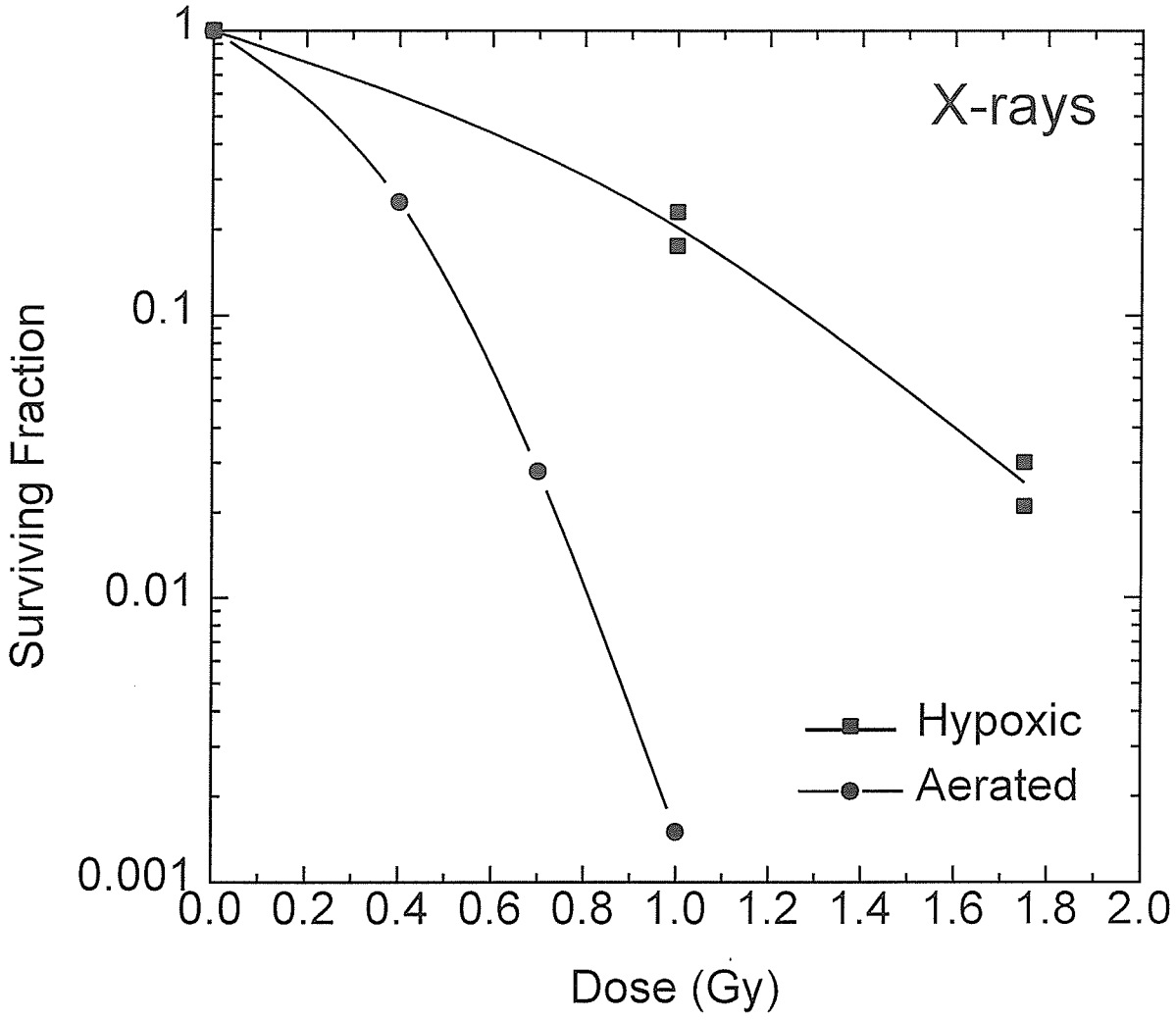

Figure 1-1 The effect of oxygen concentration on cultured human cells irradiated in vitro. Data taken from Broerse, J. J., G. W. Barendsen and G. R. Kersen 1967. Survival of cultured human cells after irradiation with fast neutrons of different energies in hypoxic and oxygenated conditions. Int. J. Radiat. Biol. 13:559-72.

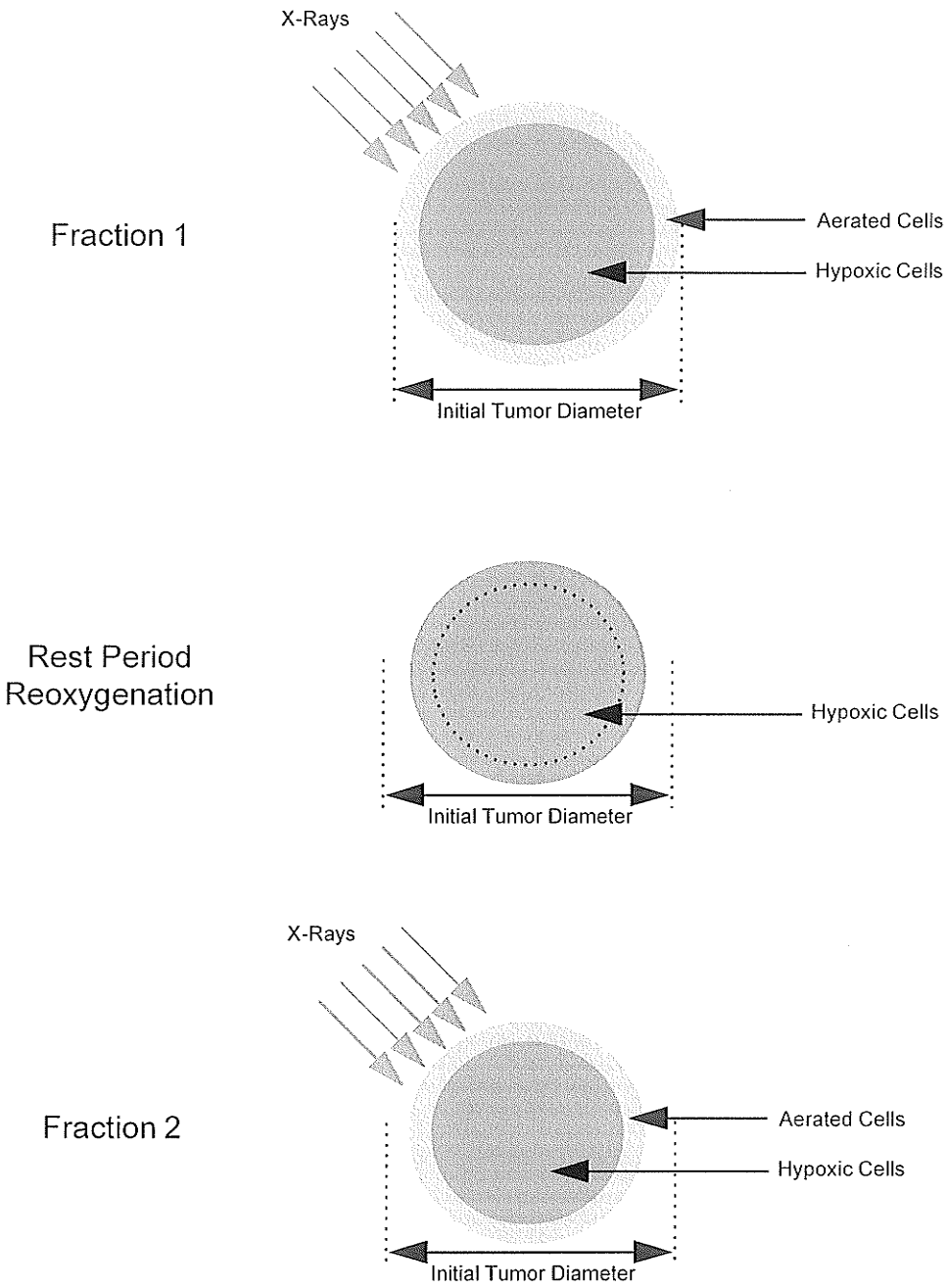

Figure 1-2 The effect of dose fractionation on aerated and hypoxic tumor cells. During fraction 1, the aerated tumor cells are lethally exposed. During the rest period, the outer layer of dead cells is stripped away exposing hypoxic tumor cells oxygen and sublethal damage incuured in the normal tissue is repaired.

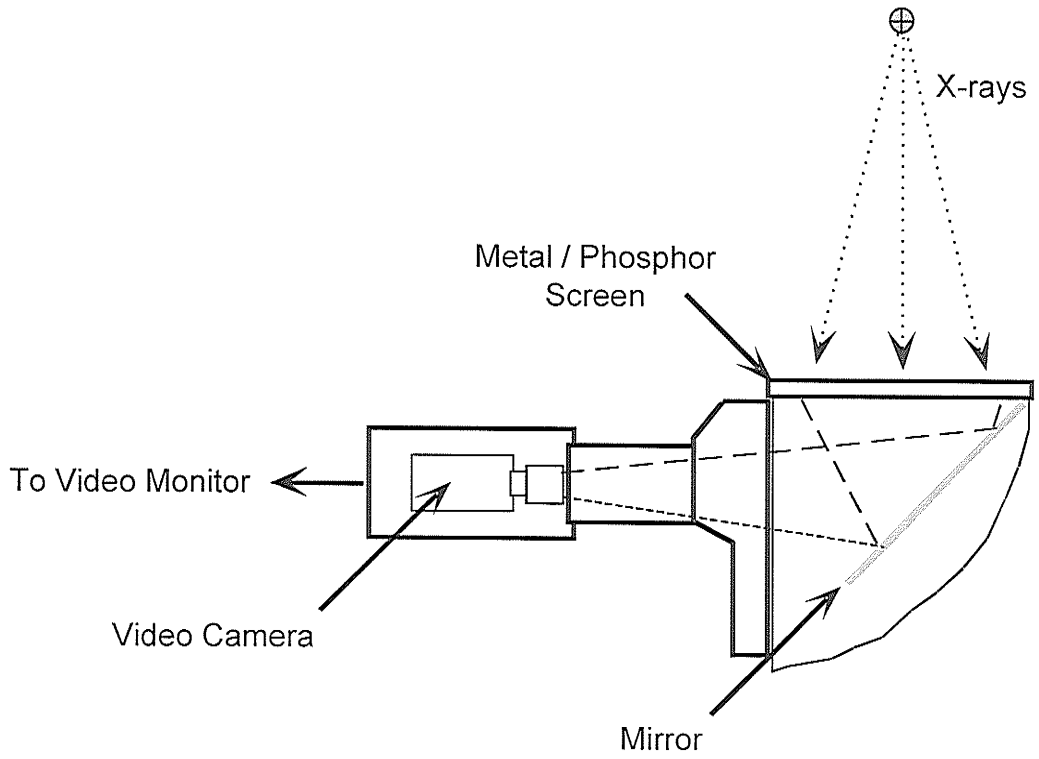

Figure 1-3 A schematic diagram of a video based electronic portal imaging device.

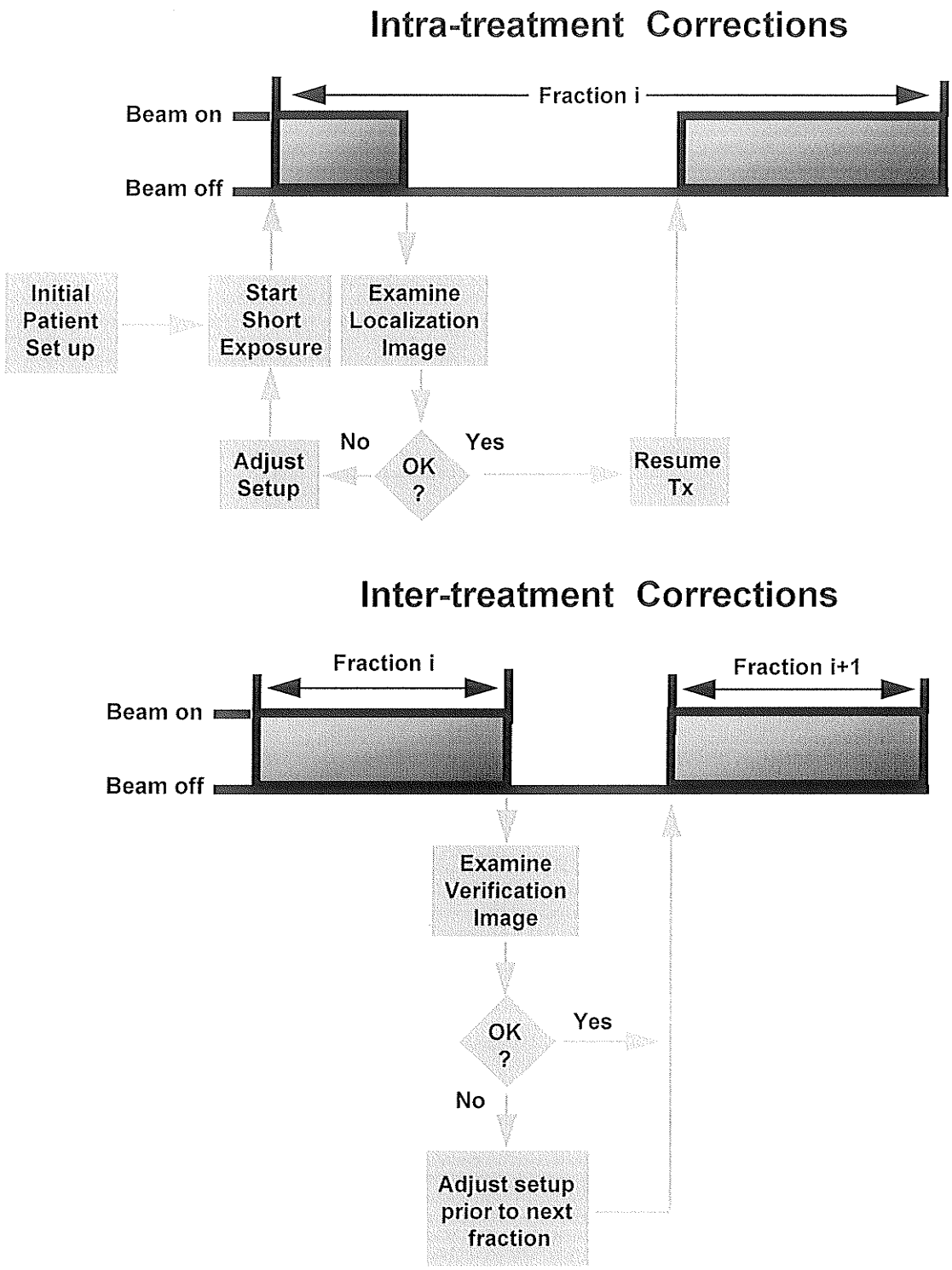

Figure 1-4 A schematic diagram showing the principles of the inter-treatment and intra-treatment correction techniques.

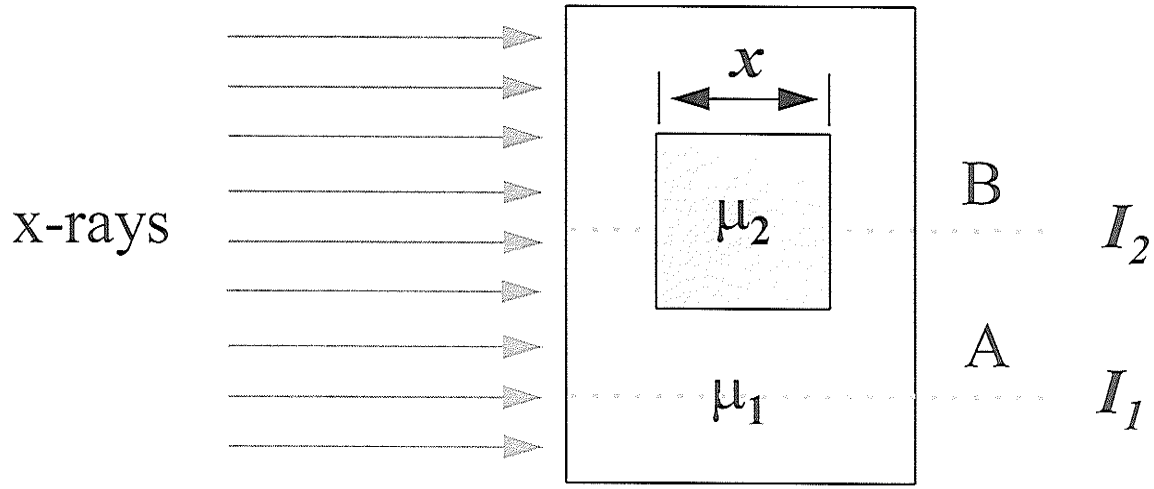

Figure 1-5 A schematic diagram of a model used to derive radiological contrast.

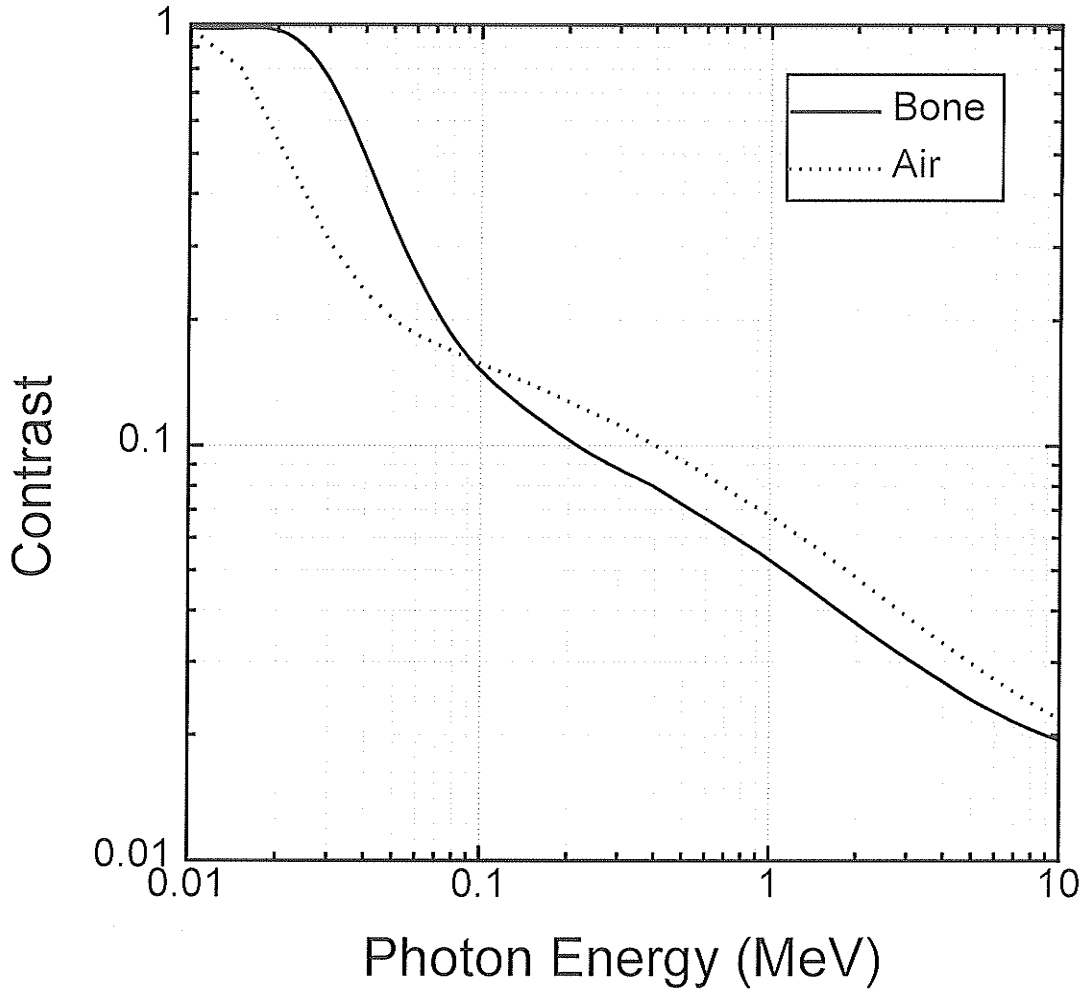

Figure 1-6 The contrast for a 1 cm section of bone and air embedded in a uniform block of soft tissue. Contrast decreases rapidly as a function of increasing energy.

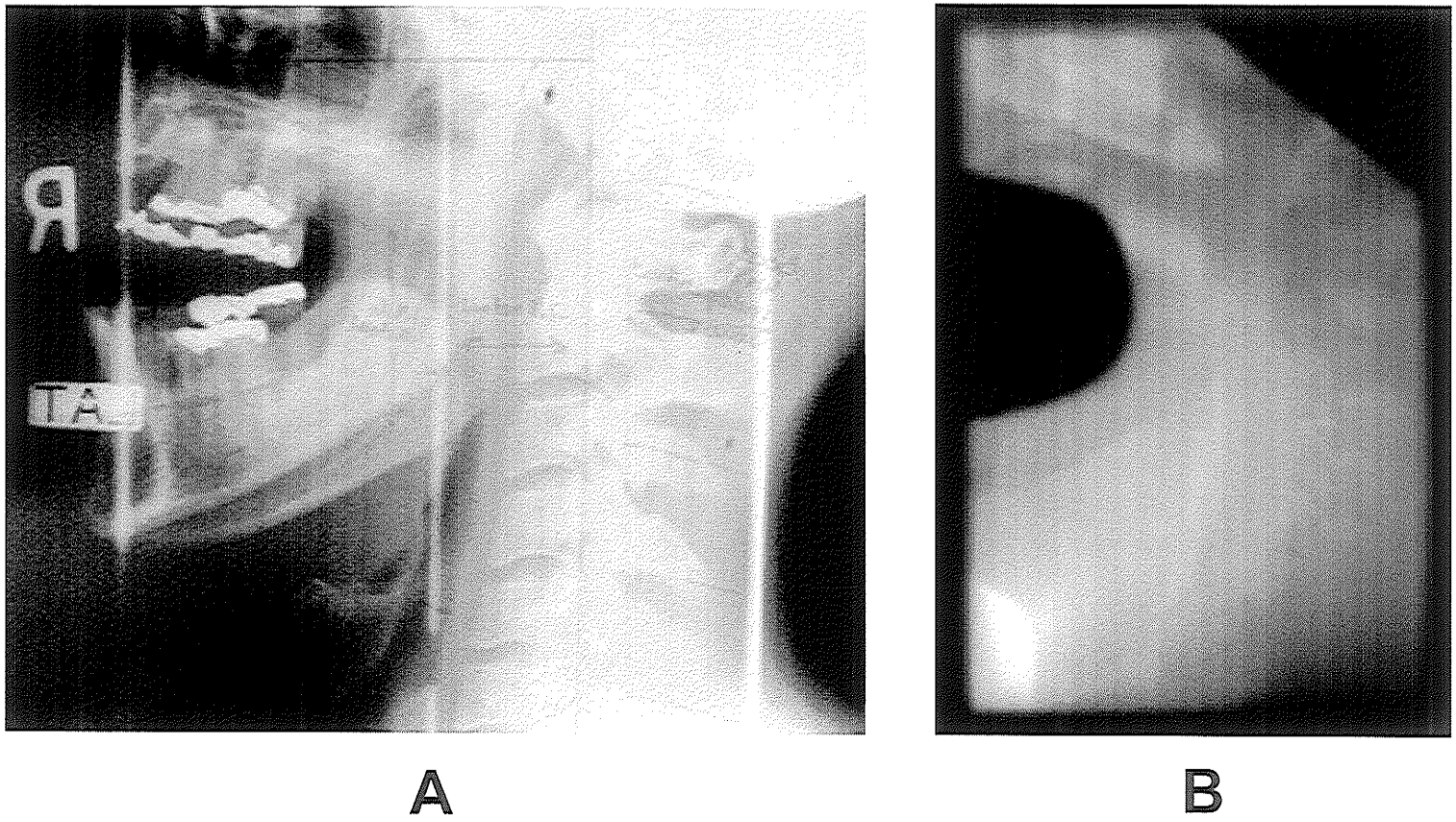

Figure 1-7 (A) A left lateral simulator film acquired at a tube voltage of 75 kVp. (B) The corresponding portal image acquired at an energy of 6 MV. The difference in contrast between the two images is quite evident.

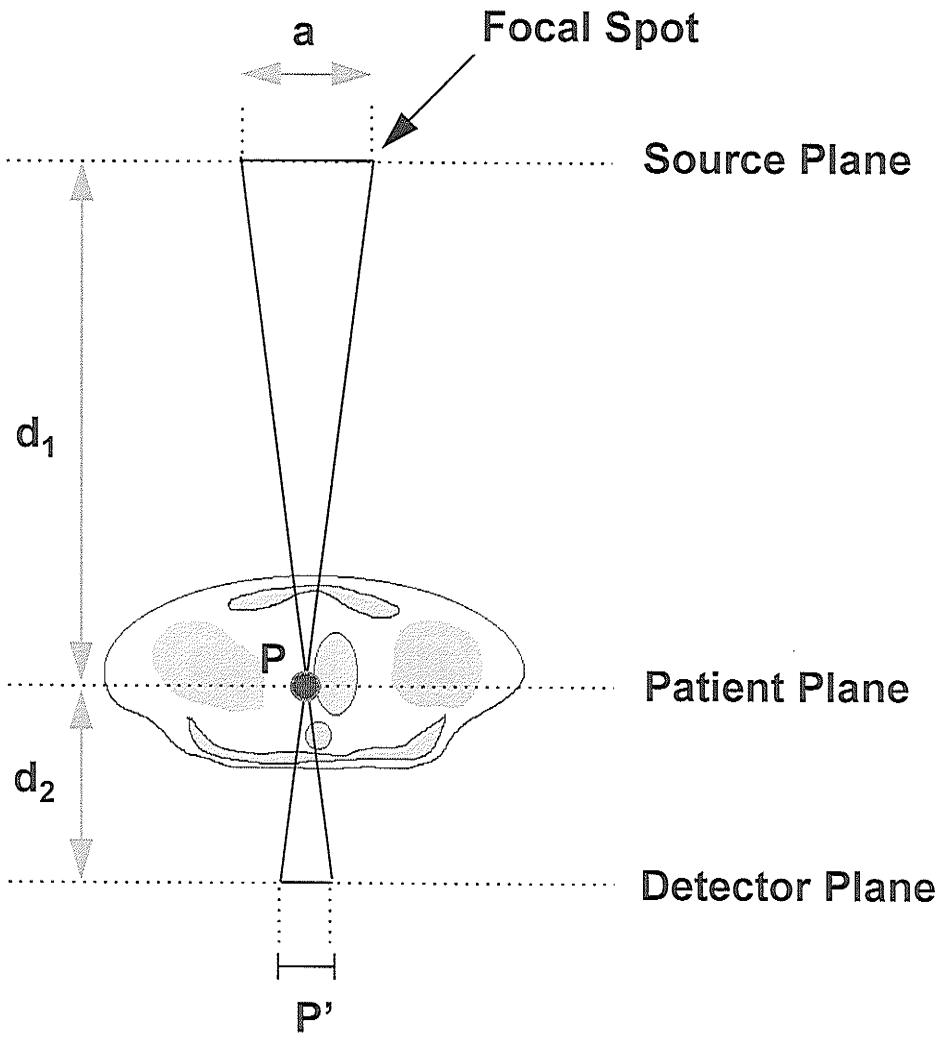

Figure 1-8 A penumbra arises due to the source size of the treatment machine. A point P is then projected to the detector plane with an increased size P'.

Chapter 2

A figure of merit for optimization of sequential processing

2.1 Introduction

Digital enhancement of portal images and films stems mainly from the need for improved contrast and noise reduction which allow observers to extract more information from the images. One of the simplest methods of image enhancement is intensity windowing which linearly remaps a small range of pixel values to the full range of intensities. This method has limited application to portal images, however, as pixels outside the window are mapped to the maximum or minimum pixel values; therefore one part of the image may show good contrast while another part will be saturated. This poses a major problem in the visualization of portal images as field boundary locations, used as reference points for treatment verification, depend on the window level and may be distorted as a result of the windowing. Global histogram equalization techniques also offer little advantage in the enhancement of portal images as information contained outside the treatment field is included in the pixel mapping function, often obscuring the anatomical details inside. A family of adaptive techniques[1,2] have shown promise in the enhancement of diagnostic images but the application to portal images has been limited by their tendency to blur field edges and over enhance noise. One particular variation called selective contrast limited adaptive histogram equalization (SCLAHE), developed by Leszczynski et al[3], is particularly suited to the enhancement of portal images as it eliminates the blurring of field edges associated with the other adaptive techniques. In the SCLAHE method, the field edge of the treatment image is detected and only those pixels that lie inside the contour are processed using a contrast limited adaptive technique[1]. Although SCLAHE performs well, noise inside the field contour is still enhanced, degrading image quality.

2.2 Sequential processing

In an attempt to improve the earlier techniques, a composite enhancement procedure has been developed by Gluhchev and Shalev[4,5], which consists of applying an adaptive enhancement technique in combination with noise reduction and edge sharpening filters. This method, called sequential processing, has been found to perform better than any of the previously described methods mainly due to its ability to limit noise amplification introduced by the standard adaptive enhancement techniques while preserving and sharpening edges in the image.

The first stage of the composite technique employs the SCLAHE algorithm and is followed by a noise reduction filter through the application of a fast two-dimensional median filter developed by Huang et al.[6]. The algorithm of the median filter is based on a histogram updating scheme which is less computationally expensive than the conventional median filter. The fast median filter requires $O(n)$ operations to perform a specific task whereas the conventional median filter performs the same task in $O(n^2)$ operations (n is the size of the convolution mask). Fast median filtering of a 512 x 480 image requires about 10 seconds on a 486 computer and is only mildly dependent on mask size.

The edge sharpening segment of the algorithm transforms pixel gray level p at coordinate (i,j) according to the formula,

$$p'(i,j) = p(i,j) + f \cdot \Delta P \tag{1}$$

where $p'(i,j)$ is the transformed pixel gray level, f is a floating point scaling factor whose value is between 0 and 1. ΔP is a custom sharpening operator given by,

$$\Delta P = \begin{cases} \Delta P^x, & \left(\left|\Delta P^x > \Delta P^y\right|\right) \\ \Delta P^y, & otherwise \end{cases} \tag{2}$$

$$\Delta P^x = p(i,j) - \frac{\left(p(i-m,j) + p(i+m,j)\right)}{2} \tag{3}$$

$$\Delta P^y = p(i,j) - \frac{\left(p(i,j-m) + p(i,j+m)\right)}{2} \tag{4}$$

$$m = \frac{n-1}{2} \tag{5}$$

where n is the size of the convolution kernel.

A objective assessment of image quality in general is difficult to attain and is therefore usually defined subjectively by displaying images to a number of observers and assigning them recognition-based tasks. Image quality is then based on the observers' ability to perform the assigned task. More complex techniques[7] simulate the response of an ideal observer to a binary task and calculate a test statistic on the assumption that signal and noise in the image are known exactly. This artificial situation is rarely achievable in radiological imaging as the contrast of target lesions is highly variable and usually superimposed on a background of anatomical structure, questioning the validity of these tests in comparison to typical clinical conditions.

The remainder of this chapter discusses a figure of merit (*FOM*) useful for optimizing the sequential processing technique for application to portal images and does not attempt to objectively assess image quality in general. The *FOM* is formed by considering characteristics common to portal images such as spatial resolution and contrast to noise ratio (*CNR*). Local maxima may then be found in the *FOM* suggesting optimal parameters for use in the sequential processing technique.

2.3 Figure of merit

A figure of merit (*FOM*) was constructed by considering the three properties common to portal images, these being poor contrast, low spatial resolution and high levels of noise. The form of the figure of merit is given by,

$$FOM = M_f \times CNR \tag{6}$$

where M_f is the relative modulation at frequency f and *CNR* is the contrast to noise ratio.

A method to determine spatial resolution in a digital imaging system was developed by Droege[8,9] for use with CT scanners and required the acquisition of images of a specially designed phantom. This procedure was later implemented for monitoring the performance of electronic portal imaging devices (EPIDs) by Rajapakshe[10] using the phantom shown in Fig. 2-1. The phantom consists of five high contrast rectangular bar patterns of varying frequency and lead contrast blocks. The bar patterns situated under ROIs 1 to 5 have frequencies of 0.758, 0.417, 0.246, 0.195 and 0.100 lp/mm respectively all of which can be analyzed to determine a relative modulation transfer function (M_f) which is given by,

$$M_f = \frac{\sqrt{\left(\sigma_{m_f}^2 - \sigma_n^2\right)}}{\sqrt{\left(\sigma_{m_1}^2 - \sigma_n^2\right)}} \tag{7}$$

where σ_n^2 is the pixel intensity variance due to random noise, $\sigma_{m_f}^2$ is the total variance measured from the ROI overlying the bar pattern frequency with f and $\sigma_{m_1}^2$ is the total variance measured in ROI 1.

The random noise component of an image is determined by subtracting a pair of similar images which effectively removes contributions from low frequency background variations in pixel intensity and fixed pattern noise[11]. Pixel variations in ROI 1 of the subtracted image are then analyzed assuming that noise is the same for all ROIs and is given by,

$$\sigma_{sub}^2 = \sigma_1^2 + \sigma_2^2 \tag{8}$$

where σ_1^2 and σ_2^2 are the noise variances associated with image 1 and 2 respectively. If the two images are acquired under the same conditions, the variances, σ_1^2 and σ_2^2 in Eqn. (8) can be assumed equal giving,

$$\sigma_1^2 = \sigma_2^2 = \sigma_n^2 \tag{9}$$

and using Eqn. (8), the random noise is given by,

$$\sigma_n = \frac{\sigma_{sub}}{\sqrt{2}} \tag{10}$$

Image contrast is determined by examining the average pixel intensities contained within ROI 1 and ROI 6 which is superimposed over a region of the phantom containing a lead contrast block as shown in Fig. 2-1. The *CNR* is therefore given by,

$$CNR = \frac{I_1 - I_6}{\sigma_n} \tag{11}$$

where I_1 and I_6 are the average pixel intensities measured from ROIs 1 and 6 respectively and σ_n is the random noise found from Eqn. (10).

The *FOM* given in Eqn. (6) is optimized for each stage of the sequential processing technique to determine the optimal parameters for portal image enhancement. The first step involves optimizing the clipping level associated with the SCLAHE technique. The clipping level determines the strength of contrast enhancement by limiting the slope of the cumulative distribution function of the image. Large clipping levels will give a strong contrast enhancement but noise is amplified in the process. Low clipping levels may limit the amplification of noise but offer limited contrast enhancement so optimization of this parameter finds the best combination between contrast and noise in an image.

The second and third stages of the process suggest the optimal size of the applied convolution mask for the median and the edge sharpening filters. Although median filters are effective in removing noise while preserving field edges, extended regions of high frequency information may be degraded depending on the size of the convolution mask. Likewise, the degree of edge sharpening is highly dependent on the mask size of the filter. Other parameters such as contextual region size and gain factor are held constant at values of 32 x 32 and 1 respectively and were not optimized in this study.

2.4 FOM optimization for sequential processing

The purpose of portal image processing is to increase the visibility of anatomical structures providing an enhanced perception of field placement with respect to the target volume. Anatomical structures used for treatment verification in portal images are typically about 2 or 3 mm in width, therefore spatial frequency optimization of the sequential processing technique is ideally carried out using bar patterns with frequency equal to 0.195 lp/mm which corresponds to 5.1 mm/lp or 2.56 mm per bar.

The *FOM* optimization described here is specific to each EPID and/or linac that is used to acquire the images. Furthermore, optimization may be specific to treatment site and may vary for different patients. Therefore a general set of optimization parameters does not exist and must be determined for each specific application.

To demonstrate how the *FOM* may be optimized for a specific case, consider Figs. 2-2a and 2-2b which show typical phantom images acquired at energies of 6 and 23 MV respectively. SCLAHE was applied to each image using varying degrees of clipping (1.4 to 2.6) and each image was analyzed to determine the relative modulation at a frequency of 0.195 lp/mm ($M_{0.195}$) and *CNR* as outlined in the previous section. Figure 2-3a shows a plot of the *FOM* versus clipping level for the SCLAHE processed images. The optimal clipping levels were found to be 1.8 and 1.4 for the 6 and 23 MV images respectively.

The optimal clipping levels were applied to both the 6 and 23 MV images which were subsequently median filtered with convolution kernels ranging in size from 3 x 3 to 9 x 9. The *FOM* was calculated for each image and is plotted in Fig. 2-3b versus the mask size of the filter. The optimal size of the convolution kernel was found to be 5 x 5 for both the 6 and 23 MV images.

With the optimal SCLAHE clipping level and median filter applied, the phantom images were convolved with edge sharpening filters ranging in size from 2 x 2 to 9 x 9. Figure 2-3c shows a plot of the *FOM* versus mask size and it was found that the optimal mask sizes were 7 x 7 and 5 x 5 for the 6 and 23 MV images respectively.

Therefore the optimized procedure for the 6 MV images consists of applying; (a) SCLAHE with clipping level of 1.8, (b) median filter with mask size 5 x 5 and (c) edge sharpening filter with a mask size of 7 x 7. For the 23 MV phantom images, the optimal procedure consists of applying; (a) SCLAHE with clipping level of 1.4, (b) median filter with a mask size of 5 x 5 and (c) edge sharpening filter with mask size of size 5 x 5.

Figures 2-2c and 2-2d show phantom images acquired at 6 and 23 MV each processed with the optimized sequential technique as outlined above. Structures vaguely visible in the original images show good contrast with minimal noise amplification after enhancement. Also note that the field edges show no distortion or blurring as a result of the processing, unlike the standard adaptive techniques.

2.5 Clinically significant results

Figure 2-4 shows the results of applying the parameter optimized sequential technique to typical clinical images acquired at megavoltage energies. Figure 2-4a shows a typical right lateral portal image of a head and neck treatment acquired at an energy of 6 MV. No bony landmarks are visible in this image but after processing with the optimized sequential technique, shown in Fig. 2-4b, the vertebrae as well as the mandible are clearly visible. Figure 2-4c shows a typical anterior portal image of a patient being treated for cancer of the cervix and was acquired at an energy of 23 MV. The enhanced image,

shown in Fig. 2-4d, clearly shows the edge of the pelvic rim allowing target volume to be identified in the enhanced image. Figure 2-5a shows an above average quality left lateral portal image of a 37 year old male being treated for Hodgkin's disease of the nasopharynx and cervical nodes at an energy of 6 MV. The cervical spine is barely visible but after processing with the optimized sequential technique, shown in Fig. 2-5b, the vertebrae are well defined and their position with respect to the field edge can easily be verified. Figure 2-5c shows an above average quality anterior portal image of a patient being treated for cancer of the prostate at an energy of 23 MV. The pelvic rim and symphysis pubis show little contrast making target volume verification difficult in this image. The same image after processing is shown in Fig. 2-5d and has much better contrast than the original image. Although the tumor itself cannot be seen in Fig. 2-5d, it's position is known with respect to anatomical features present in the image which after processing are easily distinguishable.

2.6 Conclusions

A composite processing technique has been developed that consists of applying SCLAHE, median filtering and edge sharpening in a successive fashion and has shown encouraging results when applied to megavoltage images. By acquiring and processing images of a specially designed high contrast spatial resolution phantom, each stage of the sequential technique can be optimized by calculating a figure of merit that is based on characteristics common to portal images. The figure of merit can be optimized for a particular spatial frequency by analyzing the corresponding ROI for relative modulation. In this way, anatomical structures of a particular size can be preferentially enhanced. The figure of merit employed in this study was basic in form and only considered the product of the relative modulation at a single frequency and CNR. A complex but

possibly more useful figure of merit could be derived incorporating a combination of frequencies and / or other image characteristics.

Optimization is also necessary for both energies of dual energy machines due to the different imaging characteristics associated with the different energies. This is also true for the various EPIDs on the market and may be true for the EPIDs produced by the same manufacturer.

Although definite improvements in the visibility of anatomical structures are apparent in the processed clinical images as compared to the originals, further evaluation of the sequential technique is necessary to see if it provides a clinical advantage, which ultimately determines the quality of images produced.

References

1. S. M. Pizer, E. P. Amburn, J. D. Austin, R. Cromartie, A. Geselowitz, T. Greer, B. Romeny, J. B. Zimmerman and K. Zuiderveld, "Adaptive histogram equalization and its variations," Comput. Vision Graphics Image Process **39,** 355-368 (1987).

2. R. Cromartie and S. M. Pizer, "Structure-sensitive adaptive contrast enhancement methods and their evaluation," Image Vision Comput. **11,** 460-467 (1993).

3. K. Leszczynski, S. Shalev and S. Cosby, "The enhancement of radiotherapy verification images by an automated edge detection technique," Med. Phys. **19,** 611-622 (1992).

4. G. Gluhchev and S. Shalev, "Combined approach for portal image enhancement", Proc. of European Congress of Medical Physics, Tenerife, 1993.

5. G. Gluhchev and S. Shalev, "Portal image enhancement: A comparison of techniques", The 3rd International Workshop on Electronic Portal Imaging: Clinical Applications of Electronic Portal Imaging, San Francisco, 1994.

6. T. S. Huang, G. J. Yang and G. Y. Tang, "A fast two-dimensional median filtering algorithm," IEEE Trans. Acoust., Speech, Signal Processing **ASSP-27,** 460-465 (1979).

7. H. H. Barrett, T. Gooley, K. Girodias, J. Rolland, T. White and J. Yao, "Linear discriminants and image quality," Image Vision Comput. **10,** 451-460 (1992).

8. R. T. Droege and R. L. Morin, "A practical method to measure the MTF of CT scanners," Med. Phys. **9,** 758-760 (1982).

9. R. T. Droege, "A practical method to routinely monitor resolution in digital images," Med. Phys. **10,** 337-343 (1983).

10. P. R. D. Rajapakshe, *Optimization of a real-time portal imaging system for quantitative imaging,* (Ph.D. Thesis, University of Manitoba, Winnipeg, Manitoba, 1995).

11. R. Rajapakshe and S. Shalev, "Noise analysis in real-time portal imaging. I. Quantization noise," Med. Phys. **21,** 1263-1268 (1994).

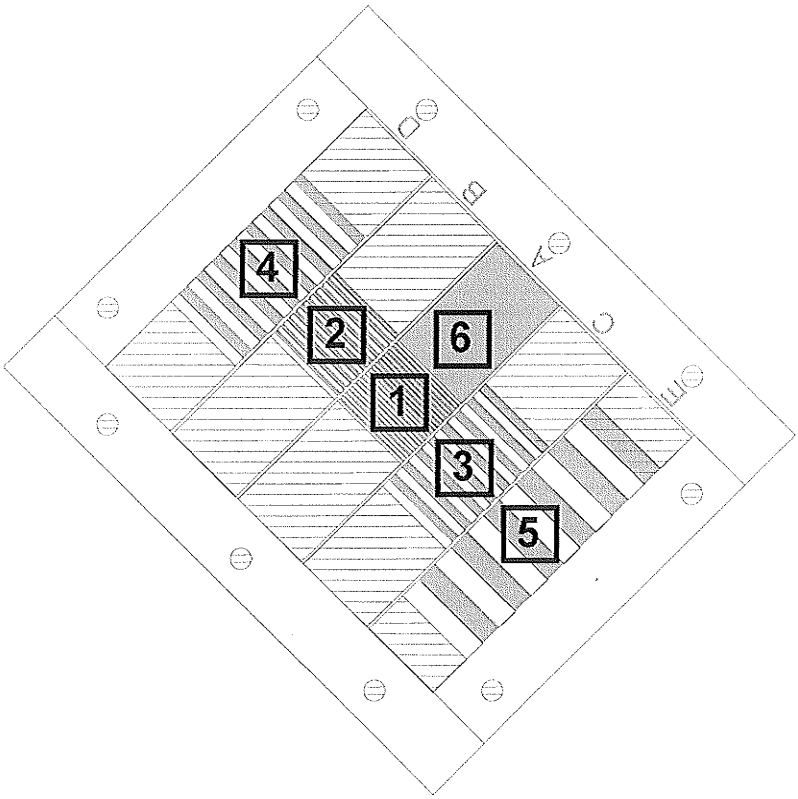

Figure 2-1 A schematic diagram of a high contrast spatial resolution phantom originally used for performance evaluation of electronic portal imaging devices.

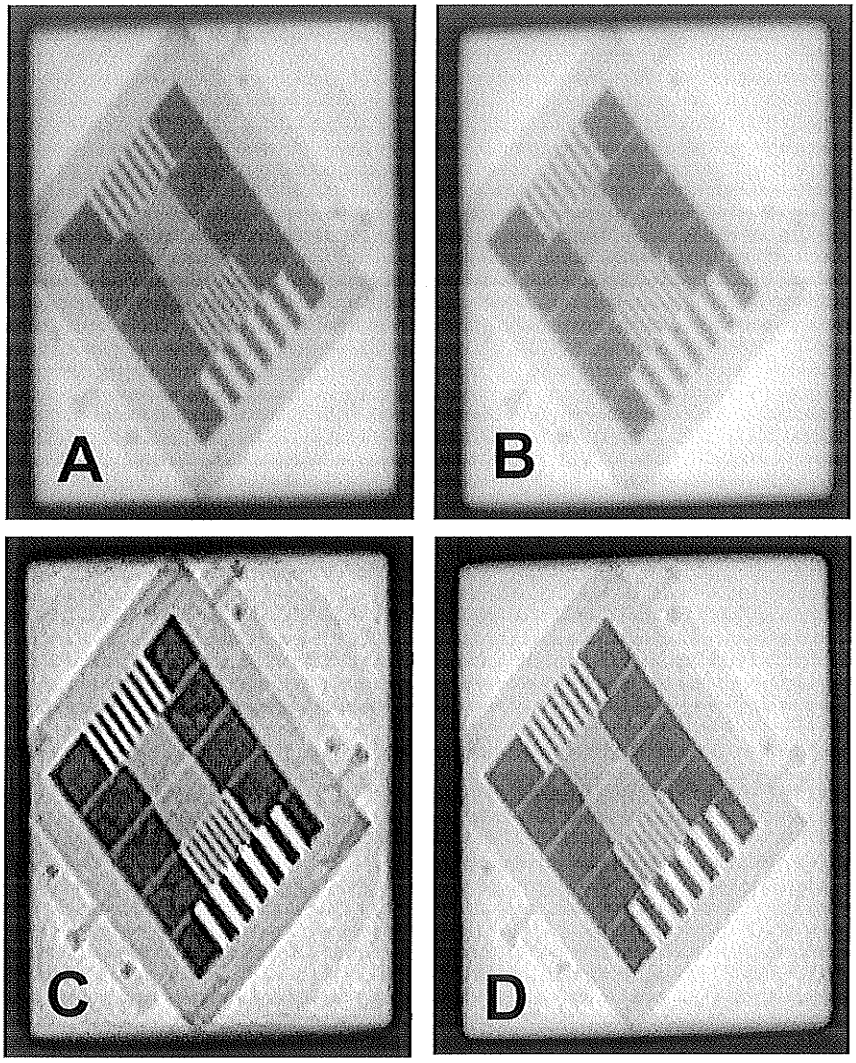

Figure 2-2 Original phantom images acquired at energies of (A) 6 MV and (B) 23 MV. Images (C) and (D) are the corresponding optimized sequential processed images.

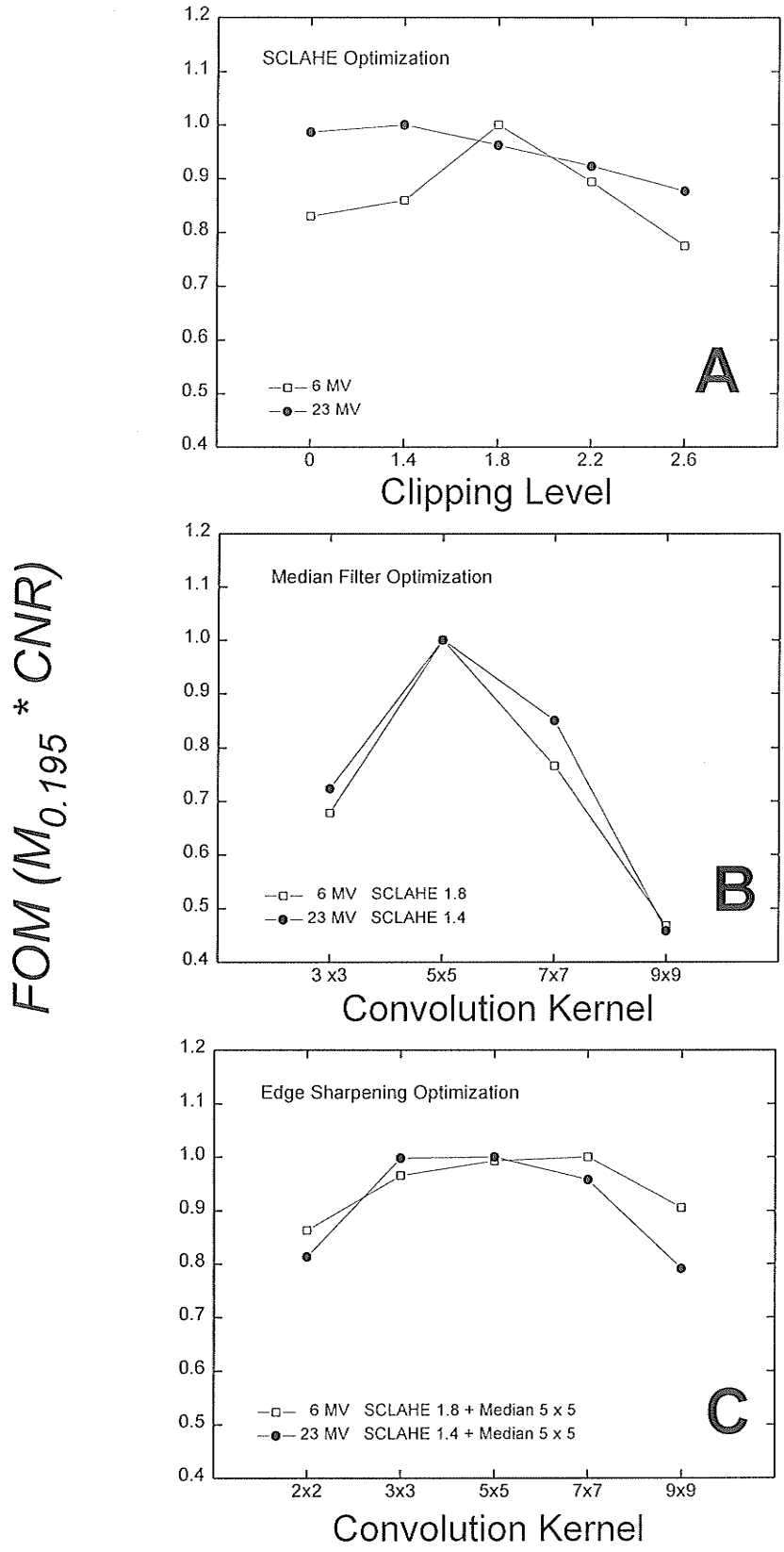

Figure 2-3 Optimization of sequential processing

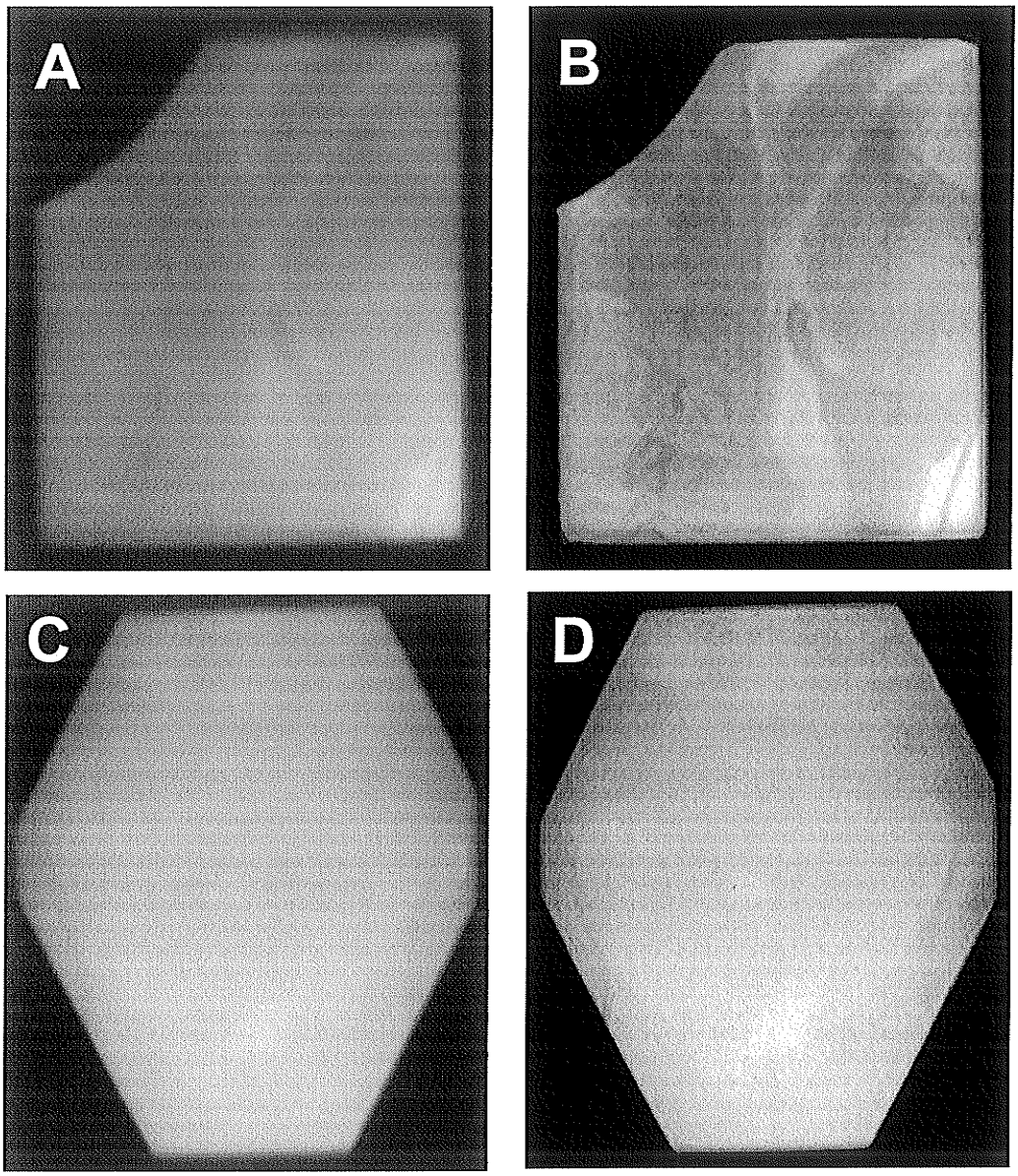

Figure 2-4 (A) A typical right lateral head and neck image acquired at 6 MV and (B) the sequential processed image. (C) A typical image of an anterior pelvic treatment at 23 MV and (D) the sequential processed image.

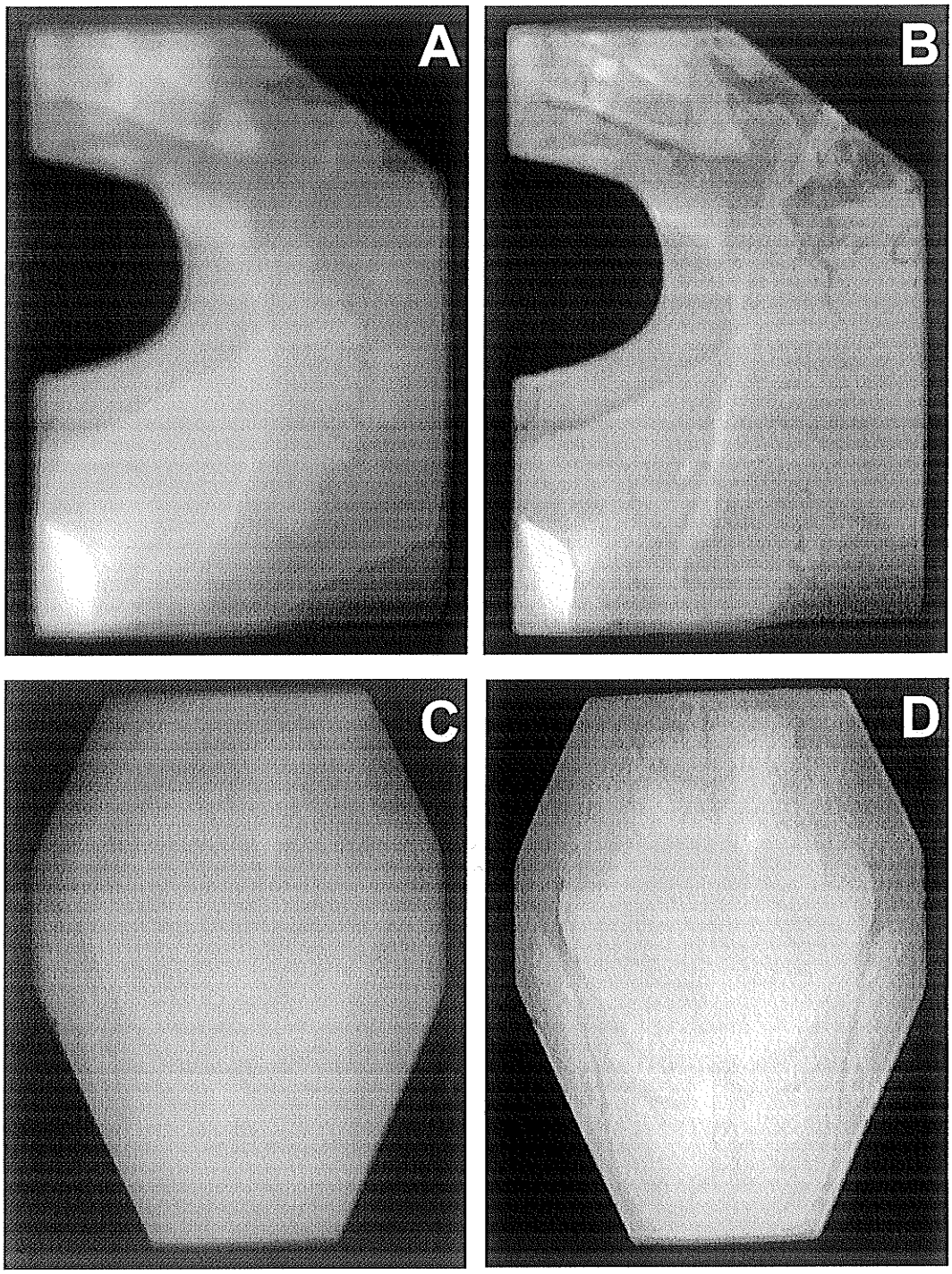

Figure 2-5 (A) A high quality left lateral head and neck image acquired at 6 MV and (B) the sequential processed image. (C) A high quality image of an anterior pelvic treatment at 23 MV and (D) the sequential processed image. Less than 10% of all portal images acquired have an unprocessed quality as high as images (A) and (C).

Chapter 3

Pelvic irradiation of the obese patient: A treatment strategy involving megavoltage simulation and intra-treatment setup corrections

3.1 Introduction

Conventional external beam radiation therapy is characterized by seven basic stages: (a) diagnostic imaging to locate the tumor in relation to anatomical landmarks; (b) radiography with a simulator or CT scanner to locate the tumor and/or anatomical landmarks in relation to the gantry coordinate system; (c) treatment planning to prescribe the target volume and beam parameters; (d) simulation of the treatment setup to establish field marks on the patient's skin or cast; (e) setup of the patient in the treatment room; (f) delivery of the treatment; and (g) verification of treatment accuracy. In some centers these stages are modified by the use of virtual simulation[1-2] or CT-simulation[3-5], or other permutations according to local practice and experience. But it is generally the case that at stage (e) two essential conditions apply: the beam's eye view (BEV) projections of each treatment field have been specified on film (or digital reconstructed radiographs), and marks have been established on the patient and/or cast for aligning the light field projections or the laser beams used in patient setup. Portal films or electronic portal images can then be compared with the simulator films or DRRs to verify treatment accuracy and to determine whether a correction should be applied to the patient setup.

For obese patients exceeding the loading limit of the simulator couch, simulation is not possible, and there is a problem in setting up the patient on the treatment couch in the absence of field or laser locating marks. Furthermore, without simulation films there is no prescription image for comparison with portal images. It was also apparent that the patient could not be set up accurately and consistently on a daily basis, and that intra-treatment

corrections would have to be applied. This implies that a localization portal image would be acquired at the start of each field at every treatment session, and that setup corrections would be applied (if necessary) before delivery of the remainder of the dose. This situation was handled by acquiring "megavoltage simulation images" during the first fraction and comparing them to electronic portal images acquired during subsequent fractions. Intra-treatment corrections were applied when the radiation therapist considered that a significant field placement error was present, and electronic portal images were acquired for the corrected patient position. Off-line analysis of the images provided a wealth of information on the potential field placement errors that would have occurred in the absence of intra-treatment corrections, and on the treatment accuracy attained for this patient as a result of the interventional verification strategy.

The application of intra-treatment setup corrections is not new. Several studies using film[6] and electronic portal imaging devices[7-12] have demonstrated its value in reducing random field placement errors. Although the present study involves only a single patient, the experimental and analytical methods reported here can be used in other situations when simulation films are unavailable and intra-treatment corrections are required.

3.2 Methods

3.2.1 Radiotherapy Prescription and Megavoltage Simulation

The subject of this study was a 42 year female diagnosed with stage IIb cancer of the cervix who weighed 150 kg and had lateral and A/P separations of 48 cm and 37 cm respectively. A total dose of 6000 cGy was prescribed to be distributed to an AP, PA and two lateral fields using a four field box technique. The prescribed energy for treatment was 23 MV (dose rate 300 mu/min) and was delivered with a Siemens KD2 linear

accelerator equipped with a BEAMVIEW^{PLUS} portal imaging system[†]. Phase I of treatment had a prescribed dose of 4000 cGy in 20 fractions while phase II had a total dose of 2000 cGy in 10 fractions. Field sizes and positions were prescribed by the radiation oncologist during the first treatment fraction using megavoltage simulation and are listed in Table 3-1. A radio-opaque marker was inserted next to the cervix and the patient was placed supine on the treatment couch in what was estimated to be the correct location. A short localization portal image was acquired, treatment was halted, and the field size and position were evaluated visually on the monitor by the radiation oncologist. The treatment couch was then moved to correct the patient setup, and a second localization image was acquired and evaluated. When an acceptable localization image was obtained, skin and laser marks were placed on the patient's skin, and the remainder of the first fraction was delivered. This procedure was repeated for all four fields. The verification images acquired for each field during the first fraction became the prescription images for subsequent comparison with portal images during later fractions. The cervical marker was removed for subsequent fractions and patient set up was verified by monitoring the position of the bony landmarks with respect to the field edges for the remainder of the treatment.

Figures 3-1a and 3-1b are images acquired of the anterior field from the first (simulation) fraction of course I, and the cervical marker is clearly visible in both images. Figure 3-1a was acquired with a dose of about 10 cGy. After review by the oncologist and correction of the patient setup, a second localization image was acquired, shown in Fig. 3-1b, which then served as the "prescription image" for all subsequent treatment fractions for the anterior field for course I. The posterior, right and left lateral fields were prescribed and monitored in the same manner as were all four fields in course II of treatment.

[†] Siemens Medical Systems, Concord, CA.

Throughout both courses of treatment the anterior field was treated first followed by the left lateral, posterior and right lateral fields.

3.2.2 Intra-treatment Corrections

Figure 3-2 shows the sequence of steps followed for the intra-treatment correction procedure. After initial patient setup, a short exposure is given and the treatment is stopped. If necessary, patient setup is adjusted and a second image is acquired and analyzed before delivering the remainder of the treatment dose.

The action level to initiate a correction to the patient setup was defined as a field displacement of 5 mm or greater. However, no software measuring tools were available for the therapist to use on the monitor screen, and in practice the therapist was obliged to estimate the observed displacement and make a subjective decision if it was greater than the prescribed action level.

Measured displacements for anterior and posterior fields of course I, prior to and after intra-treatment correction, are illustrated in Fig. 3-3. The solid and hollow squares are the reference displacements as measured from the megavoltage simulation images for the anterior and posterior fields respectively and all other displacements are measured relative to them. The solid and hollow circles and triangles are the displacements measured from the anterior and posterior images respectively, before and after corrections were applied. Arrows appear in those fractions where a correction was made, the orientation of the arrow indicating the direction of the correction. The first displacement deemed unacceptable by the radiotherapist occurred in the anterior field of fraction 3 and was corrected before completion of the treatment. A total of nine corrections were applied to the anterior field and only one correction was made to the posterior field.

Figure 3-3 shows that initial displacements over 10 mm were common in the anterior and posterior fields of course I.

3.2.3 Image Calibration

All displacements measured use a standard coordinate system employed at our center as shown in Fig. 3-4. Lateral and cranio-caudal displacements of the anterior and posterior beams lie along the X_T and Y_T axes respectively while antero-posterior displacements of the lateral beams lie along the Z_T axis. These are measured on the portal images as displacements in the X_d, Y_d coordinates.

The images captured by the BEAMVIEW^{PLUS} EPID have a size of 512 x 480 and pixels have a 2:3 aspect ratio. The horizontal image dimension was interpolated before analysis to give a 1:1 aspect ratio resulting in asquare pixel image having a size of 664 x 480. In order to obtain a quantitative measure of setup displacement, images were calibrated by using the known field dimensions to determine the effective pixel size at isocenter. The 180 mm field width was measured 400 times in images of the anterior and posterior fields in course I of treatment and the results are plotted in Fig. 3-5. The mean field width was found to be 404.4 pixels with an associated standard deviation of 2.0 pixels giving a single pixel width of 0.445 ± 0.002 mm. For course I images, the craniocaudal fields edges extended outside the field of view of the EPID so therefore only lateral field displacements could be measured. The same calibration procedure was used for course II images giving a pixel size of 0.45 x 0.45 mm^2.

3.2.4 Field Displacements

After completion of both phases of treatment, the portal images were transferred to an IBM compatible PC for analysis. The software package Portal Image Processing System (PIPS) was used to display the treatment images and to analyze setup displacements using a mouse operated measuring tool that can be calibrated to the known pixel dimensions.

Initial and corrected field displacements were determined by first selecting landmarks on the bony anatomy of the pelvis. In this study, lateral displacements in the AP and PA fields were measured by finding the distance between the edge of the left pelvic rim and the right field edge (as viewed from the anterior image) and comparing this value to the corresponding distance in the megavoltage simulation image. A line tangent to the selected landmark and parallel to the field edge marks the position of pelvic rim in the portal image. All setup displacements were determined using this tangent line thereby eliminating the effect of cranio-caudal displacements on the lateral displacement measurements. The antero-posterior displacements in the lateral fields were found by measuring the distance between the most anterior point on the first sacral vertebra to the anterior field edge. As for the anterior and posterior fields, a line tangent to the selected landmark is used for determining displacements in the lateral fields. Since the craniocaudal field size exceeded the VEPIDs field of view in course I, the Y_T field displacements could not be measured. Craniocaudal displacements in the anterior fields for phase II of the treatment were found by measuring the distance between base of the pelvic rim at symphysis pubis and the caudal field edge, while the same displacements in the lateral fields were found by measuring the distance between the femoral head and the cranial field edge.

3.3 Results

Tables 3-2 through 3-7 list the measured displacements for the anterior, posterior and lateral fields for the two courses of treatment. Set up displacements measured from the simulator fractions are enclosed in brackets and are not included in the statistical analysis. In two fractions "intra-field corrections" were applied, that is, a setup correction was made at the beginning of the second field in a parallel-opposed pair. These fraction are marked with a "*". Measurements were performed on both localization and verification images and out of the possible 120 fields (30 fractions each with 4 fields) 1 left lateral, 1 right lateral and 2 anterior fields were not acquired due to malfunctions with the acquisition system and are marked with a "-". Measurements performed on the verification images are recorded either under a "yes" or "no" column indicating whether a correction was made to the patient set up. If no correction was made, the difference between the measured displacement from the verification and localization images was calculated and placed in the L-V(N) column. Tables 3-8 through 3-13 list results for the anterior, posterior and lateral fields with and without corrections over the two courses of treatment. The results are derived from displacements measured from the verification portal images except where a correction has been applied in which case the initial set up displacement is measured from the corresponding localization image.

3.3.1 Determination of the Action Level

Figure 3-6a shows a histogram of X_T displacements for the anterior fields of course I and II of treatment before corrective intervention. Each bin has a width of 1 mm, the dark bins indicating those displacements that were deemed acceptable by the radiotherapist while the light bins show the displacements that triggered corrective action. Although the intended action level for initiating a setup correction was 5 mm, no electronic

measurement device was available at the time of treatment and the senior therapist had to visually estimate set up displacement from the localization image acquired at the start of treatment. Analysis of Fig. 3-6a indicates that in practice the action level for setup corrections was about 7 mm, as shown by the vertical dotted lines. Figure 3-6b shows a histogram of the X_T displacements for the posterior fields of course I and II before corrective intervention. Whereas 12 measured displacements were larger than 7 mm in the anterior field, only 5 displacements exceeded 7 mm in the posterior field, and none were greater than 8 mm. This indicates that the patient's position had been verified and, if necessary, corrected in the prior anterior field, and so the posterior field setup was more accurate. Of the 5 measurements exceeding 7 mm, four were deemed to be acceptable (false negative decision) and one triggered a setup correction (true positive decision). It may be that the false negative decisions indicate a reluctance on the therapist's part to correct the posterior field after the anterior field had already been corrected. Figure 3-7 shows the combined X_T displacements for the anterior and posterior fields of course I and II of treatment before corrective intervention. The data have been fitted to a Gaussian distribution having a mean and standard deviation of -1.5 and 7.9 mm respectively. Of the total 54 measured displacements, 68.5% (37/54) were within the ±7 mm tolerance limits and did not require corrective action. Conversely, 31.5% (17/54) were greater than the tolerance limit and triggered corrections to the patient setup. The shaded area under the fitted curve corresponds to 38% of the total area, in reasonable agreement with the experimental result.

3.3.2 Transverse Displacements (X_T vs. Z_T) in Course I

Displacements measured in all four fields of a box treatment can be analyzed in a number of different ways. Measurements in AP and PA fields yield data on setup displacements in the coronal (X_T-Y_T) plane, while measurements in lateral fields provide data on displacements in

the saggital (Z_T-Y_T) plane. Combining measurements from orthogonal fields yields data on displacements in the transverse (Z_T-X_T) plane. Comparing successive measurements of the same setup, such as localization and verification images in a single field, or images from opposing pairs when no setup corrections have been applied, yields data on the measurement error. When a correction is applied, the final setup error should be zero, and any deviation from this is due to a combination of the measurement error and the accuracy with which a correction can be applied in practice.

Figure 3-8 shows two transverse plane displacement plots derived from X_T and Z_T displacements listed in Tables 3-2 and 3-3 for the AP, PA and lateral fields of course I (excluding the simulation fraction). Figure 3-8a shows displacements measured from images of the anterior and left lateral fields, which were the first fields set up in the two parallel opposing pairs of fields used in the four field box technique. 26% (9/35) were deemed unacceptable and were corrected. The relatively large number of corrections is an indication of the difficulty of aligning the treatment beam to skin marks on an obese patient. Tables 3-8 and 3-9 show that initial X_T and Z_T displacements in the anterior and left lateral fields had standard deviations of 11.6 and 1.3 mm respectively. The anterior field had displacements ranging between -18.1 to 20.5 mm, however the deviation for those fractions with and without correction was reduced to 5.0 mm as a result of corrective intervention. The Z_T deviation remained the same as no corrections were deemed necessary in the lateral fields. The initial transverse displacements measured from the posterior and right lateral fields, shown in Fig. 3-8b, have smaller standard deviations of 3.9 and 2.3 mm. Note the large reduction in initial setup displacement from the anterior to the posterior pair of parallel opposing fields. Only 1 of the 37 fields monitored in the posterior and right lateral fields was deemed unacceptable and was corrected. Before intervention, the anterior field had 8 fractions with displacements greater than 10 mm and 10 fractions with displacements greater than 5 mm. This was

reduced to 1 and 4 displacements respectively after the application of intra-treatment corrections.

3.3.3 Transverse Displacements (X_T vs. Z_T) in Course II

Figures 3-9a and 3-9b are two transverse plane displacement plots derived from measurements listed in Tables 3-4 and 3-5 for the AP, PA and lateral fields of course II (excluding the simulation fraction). Figure 3-9a shows displacements measured from images of the anterior and left lateral fields and Fig. 3-9b shows displacements measured from images of the posterior and right lateral fields. Out of the 18 fractions monitored in the anterior and left lateral fields, 3 were corrected, while no corrections were were required for the posterior or right lateral fields. Tables 3-10 and 3-11 show that initial X_T and Z_T displacements in the anterior and left lateral fields had standard deviations of 9.4 and 1.5 mm respectively. The X_T deviation was reduced to 5.6 mm after correction while the Z_T deviation remained unchanged as no corrections were made to this field. The anterior field had 3 fractions with displacements greater than 10 mm and 6 fractions with displacements greater than 5 mm before intervention, and only 1 and 4 displacements respectively after the application of intra-treatment corrections. Once again it is apparent that the posterior and right lateral fields benefit from corrections made to the preceding fields.

3.3.4 Coronal Displacements (X_T vs. Y_T) in Course II

The displacement plots shown in Fig. 3-9c and 3-9d are derived from X_T and Y_T measurements listed in Tables 3-4 and 3-6 for the AP and PA fields from course II of the treatment (excluding the simulation fraction). Out of the 18 fractions monitored, 3 X_T displacements in the anterior field were corrected, and it is again apparent that the

posterior field benefits from corrections made to the anterior field. Tables 3-12 and 3-13 show that Y_T displacements had standard deviations of 2.2 mm or less and that greatest variation of movement occurred in the anterior field which ranged between -9.9 and -2.9 mm. A 6.3 mm systematic shift is also apparent in the anterior field and although 7 initial displacements were greater than 5 mm, no corrective action was triggered.

3.3.5 Saggital Displacements (Y_T vs. Z_T) in Course II

Figures 3-9e and 3-9f are two displacement plots derived from Y_T and Z_T measurements listed in Tables 3-5 and 3-7 from the left and right lateral fields from course II (excluding the simulation fraction). No corrections were deemed necessary although 7 measured displacements were greater than 5 mm. Tables 3-11 and 3-13 show that Z_T and Y_T displacements ranged from -4.0 to 0.4 mm and -5.3 to 1.3 mm in the right lateral fields and from -8.4 mm to -3.1 mm and -7.5 mm to -1.3 mm in the left lateral fields and respectively. This is significantly less than the X_T displacements which ranged between -12.3 to 17.6 mm for the anterior field in course II showing that this patient was much more prone to daily set up errors in the lateral direction.

3.3.6 Consistency Tests

Consistency of the measured X_T, Y_T and Z_T field displacements was checked by applying the Kolmogorov-Smirnov (K-S) Statistical Test[13] to redundant data sets as measured from two distinct fields such as craniocaudal displacements in the anterior and lateral fields or from two parallel opposing fields. The test was also applied to displacements measured from a localization and verification image pair for the same field for those fractions where no correction was applied.

Table 3-14 lists the K-S test *D* statistic and corresponding probabilities of the null hypothesis (see appendix) for X_T, Y_T and Z_T displacements measured from the pairs of orthogonal and parallel opposing fields in course I & II of treatment excluding the simulator fraction and those fractions where an intra-field adjustment was made. Small *D* values along with large probabilities indicate that the cumulative distribution functions (CDFs) of the two data sets are similar and it is highly probable that the two distributions are drawn from the same parent distribution. X_T displacements measured in the AP and PA fields of course I showed a significant correlation having a *D* value equal to 0.20 and a confidence level of better than 90%. Y_T and Z_T displacements in the right and left lateral and the anterior and right lateral fields of course II showed little correlation suggesting a difficulty in measuring displacements in these directions.

Table 3-15 lists the K-S test *D* statistic and probabilities for displacements measured from localization and verification images of the same field in course I & II of treatment excluding the simulator fraction and those fractions where a correction was applied. The largest correlation occurred for the X_T measurements in the anterior and posterior fields of course II while the Y_T and Z_T displacements showed much less correlation once again suggesting a difficulty in measuring displacements in these directions.

3.3.7 Measurement Error

The measurement accuracy was estimated by considering displacements measured from localization (L) and verification (V) image pairs acquired for the same field and fraction when no corrective action was taken. The two images represent two views of patient set up which were acquired in succession of each other. Tables 3-2 through 3-7 list the differences (L-V(N) column) for each field over both courses of treatment along with the associated standard deviation σ. The measurement error is given by,

$$\sigma_m = \sqrt{\frac{\sigma^2}{2}} \qquad (1)$$

which includes contributions from two separate measurement errors associated with locating the field edge and the selected anatomical landmark. Equation (1) neglects any contribution from an error that may arise due to any lateral patient movement that may haved occurred between acquisition of the localization and verification images. Out of plane rotations may also contribute to σ and as an example, consider a rotation about a Y_T (cranio-caudal) axis centered within the patient. Large out of plane rotations were not observed in this study however, it is reasonable to suspect that rotations as large as 5^o may go unnoticed by the therapists resulting in the position of a bony landmark such as the edge of the pelvic rim shifting with respect to the field edge. Assuming the width from the right to left edge of the pelvic rim is 15.0 cm and that anatomical landmarks can be identified with exact precision in megavoltage images, a 5^o rotation would result in a landmark translation of 0.3 mm, therefore introducing only a minimal error. Exact location of selected landmarks is difficult when performed off images formed by projection shadows. A well defined edge or point in one image may appear substantially different in a second projection with slightly altered angle of incidence making exact location of a selected landmark difficult. It is acknowledged that σ_m may contain a contribution from all of these errors.

Z_T displacements in course II showed the largest measurement errors having values of 1.6 and 1.9 mm in the left and right lateral fields respectively. X_T displacements in the anterior and posterior fields of course II showed the smallest error having values of 0.4 and 0.8 mm respectively. Y_T displacements in the anterior, posterior, left and right lateral fields showed intermediate measurement errors of 1.4, 1.3, 1.1 and 1.3 mm respectively.

On average for all fields over both courses of treatment the measurement error was found to be 2.1 mm.

3.3.8 Correction Error

The correction error associated with treatment intervention was estimated by considering displacements measured from the verification (V) images for those fractions where corrective action was taken. The intent of corrective action is to align the patient to the prescribed position as given by the simulator image, therefore reducing the displacement to zero. However, deviations occur due to the therapist's judgment of the magnitude and direction of the displacements. Tables 3-2 through 3-8 list the displacements measured from the verification image (Verify V Yes column) after a correction was applied. The correction error is given by,

$$\sigma_c = \sqrt{\sigma^2 - 2\sigma_m^2} \qquad (2)$$

where σ_m is the measurement error described in the previous section. Using the average measurement error, the average correction error for all fields over both courses of treatment was found to be 5.7 mm

3.3.9 Results of Corrective Intervention

Figures 3-10 and 3-11 summarize the results of the intra-treatment correction technique as applied to this patient. Figure 3-10a shows the distribution of X_T displacements measured in the anterior and posterior fields over both courses of treatment before any corrective intervention was taken. This shows how the patient would have been treated without verification. The Figure 3-10b shows the distribution of displacements after

corrective intervention, where the standard deviation was reduced from 7.9 to 4.7 mm. Figures 3-11a and 3-11b show the distribution of Y_T and Z_T displacements over both courses of treatment respectively with deviations of 2.4 and 2.1 mm respectively. The smaller deviations as compared to the X_T displacements indicate that the patient was more stable along the Y_T and Z_T directions. However, no corrective action was taken for 20 of the Y_T and Z_T displacements which were over the 5 mm tolerance level set prior to treatment suggesting that estimation of errors in these directions is difficult.

3.3.10 Treatment Time

Megavoltage simulation increased the treatment time for the first fraction about 25 minutes. Subsequent fractions were scheduled in the usual 15 minute time slots allotted for these types of treatments at our center. On average, treatment intervention introduced an additional 1.5 minutes per fraction for those fractions that required correction or a total of 19.5 minutes for both courses of treatment. However, 31 displacements over 5 mm did not trigger any corrective action. If suitable software tools had been available these measurements would have triggered corrective action, and would have added an additional 47 minutes to the entire course of treatment.

3.4 Conclusions

In the absense of xray simulation, Megavoltage simulation is a viable alternative for obese patients as the electronic portal imager provides adequate image quality for pelvic fields of patients with large separations, and allows the clinician to delineate the target volume directly from the portal images.

Skin marks can be unreliable when aligning these patients in the treatment beam, as they do not align with the bony anatomy in any predictable way. Each fraction should therefore be monitored by comparing a localization image, acquired at the start of each treatment, to the "simulator" image and applying intra-treatment corrections if necessary.

Intra-treatment corrections increased the accuracy of target volume irradiation substantially in this study. Before corrections were applied, 10% of the initial set up displacements were greater than 10 mm and 41% greater than 5 mm. After corrective intervention, only 2% of the displacements were greater than 10 mm and 32% were greater than 5 mm. Although the tolerance for corrective action was set to 5.0 mm, the therapist had to visually estimate displacements from the images as no electronic measurement device was available at the time of treatment, and as many as 31 displacements over the 5 mm tolerance limit did not trigger any corrective intervention. This can be explained with the aid of Fig. 3-6a which shows that the tolerance level for corrective action actually employed by the therapists was about 7 mm. Using this actual action level, 27% and 11% of the measured displacements were greater than 7 mm before and after corrective intervention respectively.

Intra-treatment corrections also had the effect of reducing initial setup displacements of the second field of a parallel opposing pair of treatment fields used in the four field box technique. This is most apparent in Fig. 3-8 which shows the results for course I of treatment. Displacements ranged from -18.1 to 20.5 mm in the anterior field before corrective intervention. Treatment of the anterior field always preceded the posterior field which showed displacements ranging from -8.0 to 8.7 mm before corrections. A smaller number of corrections are required in the posterior field, or in the second of an opposing pair of lateral fields.

The Kolmogorov-Smirnov test applied to the same displacements measured from different fields shows that only the X_T displacements in course I are likely to be samples from the same parent distribution having a D value of 0.20 and a confidence level of 93%. When applied to displacements measured from localization and verification images of the same field, the X_T displacements in the anterior and posterior fields of course II showed the best correlation having D values of 0.17 and 0.25 and confidence levels of 100% and 96% respectively. It is apparent from the K-S test results that a difficulty exists in measuring displacements in the Y_T and Z_T directions.

The average measurement and correction error for all fields over both courses of treatment were found to be 2.1 and 5.7 mm respectively. Both assume that the error associated with finding a field edge or anatomical landmark is equal and that no patient movement occurred between image acquisition.

Intra-treatment intervention has been shown to significantly reduce the initial patient set up while only minimally increasing treatment time. The time required for the first treatment fraction was increased due to the megavoltage simulation procedure, however subsequent corrections required only an additional 1.5 minutes per fraction adding a total of 19.5 minutes to the entire course of treatment.

In the treatment of obese patients, the megavoltage simulation technique can be used if conventional simulation is not possible and in conjunction with intra-treatment intervention, can ensure acceptable accuracy in the delivery of dose to the prescribed treatment volume.

Appendix

The Kolmogorov-Smirnov (K-S) statistical test is used for analysis of unbinned data distributions that are functions of a single variable. The K-S test is applied by determining the normalized cumulative distribution function (CDF) $S_{N1}(x)$ and $S_{N2}(x)$ to two data sets. The only restrictions on $S_{N1}(x)$ and $S_{N2}(x)$ are that they be equal at x = 0 and x = 1. The behavior of $S_{N1}(x)$ and $S_{N2}(x)$ between the limits of 0 and 1 may differ depending on the similarity of the parent distributions of the two data sets. Figure 3-9a shows two CDFs assembled from the X_T displacements in the anterior and posterior fields of course I excluding the simulator fraction or fraction 7 which involved an intra-field adjustment. The anterior field data set includes both corrected and uncorrected fractions while the posterior data set only includes those fields where no correction was applied. Figure 3-9b shows the difference between the two CDFs and makes it much easier to identify the K-S D value for the distributions.

The K-S D value is defined as the maximum value of the absolute difference between $S_{N1}(x)$ and $S_{N2}(x)$ and is given by,

$$D = \max_{0<x<1} \left| S_{N1}(x) - S_{N2}(x) \right|$$

The K-S statistic is useful because its distribution can be approximated in the case of the null hypothesis, therefore giving the significance of any non zero observed value of D.

The calculation of the significance involves a monotonic function of a single variable Q_{KS}, which is given by,

$$Q_{KS}(\lambda) = 2\sum_{j=1}^{\infty}(-1)^{j-1}e^{-2j^2\lambda^2}$$

and has the limiting values $Q_{KS}(0)=1$ and $Q_{KS}(\infty)=0$.

The significance level of an observed value of D is then given by,

$$Prob = Q_{KS}\left[\sqrt{\frac{N_1 N_2}{N_1+N_2}}D\right]$$

where N_1 and N_2 are the number of independent data points in the two data sets. Large values of D and/or small values of *Prob* indicate that the CDFs of the two data sets differ significantly from each other and probably do not originate from the same parent distribution.

References

1. J. Rosenman, S. Sailer, G. Sherouse, E. Chaney and J. Tepper, "Virtual simulation: Initial clinical results," Int. J. Radiat. Oncol. Biol. Phys. **20,** 843-51 (1991).

2. G. W. Sherouse and E. L. Chaney, "The portable simulator," Int. J. Radiat. Oncol. Biol. Phys. **21,** 475-482 (1991).

3. D. P. Ragan, T. He, C. F. Mesina and V. Ratanatharathorn, "CT-based simulation with laser patient marking," Med. Phys. **20,** 379-380 (1993).

4. M. Hiraoka, M. Mitsumori, K. Okajima, Y. Nagata, M. Takahashi, M. Nakata and M. Abe, "Use of a CT simulator in radiotherapy treatment planning for breast conserving therapy," Radiother. Oncol. **33,** 48-55 (1994).

5. C. A. Perez, J. A. Purdy, W. Harms, R. Gerber, J. Mathews, P. R. Grigsby, M. L. Graham, B. Emami, H. K. Lee, J. M. Michalski and S. Baker, "Design of a fully integrated three-dimensional computed tomography simulator and preliminary clinical evaluation," Int. J. Radiat. Oncol. Biol. Phys. **30,** 887-897 (1994).

6. J. Leong and D. Shimm, "A method for consistent precision radiation therapy," Radiother. Oncol. **3,** 89 (1985).

7. W. De Neve, F. van den Heuvel, M. De Beukeleer, M. Coghe, L. Thon, P. De Roover, M. Van Lancker and G. Storme, "Routine clinical on-line portal imaging followed by immediate field adjustment using a tele-contolled patient couch," Radiother. Oncol. **24,** 45-54 (1992).

8. A. Ezz, P. Munro, A. T. Porter, J. Battista, D. A. Jaffray, A. Fenster and S. Osborne, "Daily monitoring and correction of radiation field placement using a video-based portal imaging system: A pilot study," Int. J. Radiat. Oncol. Biol. Phys. **22,** 159-65 (1992).

9. W. De Neve, F. van den Heuvel, M. Coghe, D. Verellen, M. De Beukeleer, A. Roelstraete, P. De Roover, L. Thon and G. Storme, "Interactive use of on-line

portal imaging in pelvic radiation," Int. J. Radiat. Oncol. Biol. Phys. **25,** 517-524 (1993).

10. P. M. Evans, J. Q. Gildersleve, C. Rawlings and W. Swindell, "Technical note: The implementation of patient position correction using a megavoltage imaging device on a linear accelerator," Brit. J. Radiol. **66,** 833-838 (1993).

11. J. Gildersleve, D. P. Dearnaley, P. M. Evans, M. Law, C. Rawlings and W. Swindell, "A randomised trial of patient repositioning during radiotherapy using a megavoltage imaging system," Radiother. Oncol. **31,** 161-168 (1994).

12. M. G. Herman, R. A. Abrams and R. R. Mayer, "Clinical use of on-line portal imaging for daily patient treatment verification," Int. J. Radiat. Oncol. Biol. Phys. **28,** 1017-1023 (1994).

13. W. H. Press, B. P. Flannery, S. A. Teukolsky and W. T. Vetterling, *Numerical recipes in C: The art of scientific computing,* (Cambridge University Press, New York, 1988).

Course	Field Size (cm^2)			
	Anterior	Posterior	Right Lateral	Left Lateral
I	22 x 18	22 x 18	22 x 12	22 x 12
II	15 x 18	15 x 18	15 x 10	15 x 10

Table 3-1 Prescribed field sizes set by the radiation oncologist during the first treatment fractions of courses I and II.

	X_T Displacements (mm) Anterior Field				X_T Displacements (mm) Posterior Field			
Fraction	Local L	Verify V		L-V(N)	Local L	Verify V		L-V(N)
		No	Yes			No	Yes	
1	(2.2)		(0.0)		(6.8)	(0.0)	(6.8)	
2	-	-	-	-	0.9	2.0		-1.1
3	15.1		6.0		-0.9	4.1		-5.0
4	15.1		3.7		-0.4	2.8		-3.2
5	-13.0		1.7		0.4	0.6		-0.2
6	2.2	0.8		1.4	-6.2	-3.5		-2.7
7*	20.5		15.1		-6.2	-5.3		0.9
8	-1.3	-0.4		-0.9	-8.0		-4.9	
9	-	-	-	-	-0.4	-0.6		0.2
10	-1.3	0.5		-1.8	0.9	2.8		-1.9
11	3.6	6.4		-2.8	4.9	8.7		-3.8
12	-8.4	-4.0		-4.4	-9.3	-2.7		-6.6
13	1.3	4.2		-2.9	-2.7	-0.4		-2.3
14	-16.3		-3.6		0	0.9		-0.9
15	-1.3	-0.8		-0.5	-6.7	-3.6		-3.1
16	-18.1		-5.4		-7.1	-5.0		-2.1
17	-7.2		-1.8		-5.8	-3.6		-2.2
18	-17.7		4.2		0	2.3		-2.3
19	-10.4		-0.8		-4.4	-1.3		-3.1
20	-4.9	-3.1		-1.8	-4.0	-1.8		-2.2
Mean			2.1	-1.7			-4.9	-2.3
σ			6.2	1.8				1.8

( ) not included in analysis
- image not acquired
* intra-field adjustment

Table 3-2 X_T displacements measured in the anterior and posterior fields of course I.

Fraction	Z_T Displacements (mm) Left Lateral Field				Z_T Displacements (mm) Right Lateral Field			
	Local L	Verify V		L-V(N)	Local L	Verify V		L-V(N)
		No	Yes			No	Yes	
1	(-10.7)		(0.0)		(2.6)		(0.0)	
2	-3.1	-3.0		-0.1	-3.1	-2.2		-0.9
3	-5.3	-1.5		-3.8	-2.2	-1.3		-0.9
4	-1.3	-1.5		0.2	-0.9	0.9		-1.8
5	-6.7	-4.7		-2.0	-3.6	-3.9		0.3
6	-4.4	-2.5		-1.9	-1.8	-5.7		3.9
7	-4.9	-2.9		-2.0	-5.8	-1.2		-4.6
8	-1.3	-1.1		-0.2	-1.8	-1.1		-0.7
9	-	-	-	-	-1.3	2.0		-3.3
10	-4.0	-3.2		-0.8	-3.6	-3.9		0.3
11	-5.8	-4.3		-1.5	-0.9	0.2		-1.1
12	-4.4	-3.8		-0.6	-4.0	-3.4		-0.6
13	-7.1	-4.3		-2.8	-4.0	-5.0		1.0
14	-2.2	-3.4		1.2	-4.9	-2.9		-2.0
15	-2.2	-3.4		1.2	-2.2	-2.9		0.7
16	-3.1	-5.7		2.6	-2.2	-5.7		3.5
17	-4.0	-4.3		0.3	-3.1	-1.3		-1.8
18	-0.9	-0.6		-0.3	-1.3	0.1		-1.4
19	-3.1	-3.4		0.3	-4.0	-2.3		-1.7
20	-4.9	-2.9		-2.0	-4.0	-5.2		1.2
Mean				-0.7				-0.5
σ				1.6				2.1

( ) not included in analysis
- image not acquired

Table 3-3 Z_T displacements measured in the left and right lateral fields of course I.

Fraction	X_T Displacements (mm) Anterior Field				X_T Displacements (mm) Posterior Field			
	Local L	Verify V		L-V(N)	Local L	Verify V		L-V(N)
		No	Yes			No	Yes	
1	(11.9)		(0.0)		(-3.0)		(0.0)	
2*	17.6		11.9		2.2	1.7		0.5
3	-1.8	-2.6		0.8	-5.3	-5.4		0.1
4	-6.0	-5.3		-0.7	-8.0	-7.1		-0.9
5	-4.9	-5.3		0.4	-6.2	-5.4		-0.8
6	2.7	1.8		0.9	-2.2	-3.6		1.4
7	-5.3	-5.7		0.4	-6.7	-7.1		0.4
8	11.9		-0.9		-2.2	-1.8		-0.4
9	-12.3		-4.8		-5.8	-8.0		2.2
10	-3.1	-3.1		0.0	3.1	0.8		2.3
Mean			2.1	0.3				0.5
σ			8.7	0.6				1.2

( ) not included in analysis
* intra-field adjustment

Table 3-4 X_T displacements measured in the anterior and posterior fields of course II.

Fraction	Z_T Displacements (mm) Left Lateral Field				Z_T Displacements (mm) Right Lateral Field			
	Local L	Verify V		L-V(N)	Local L	Verify V		L-V(N)
		No	Yes			No	Yes	
1	(5.7)		(0.0)		(13.2)		(0.0)	
2	-4.0	-6.2		2.2	0.9	-2.7		3.6
3	-4.4	-6.2		1.8	7.6	-1.3		8.9
4	-1.1	-3.1		2.0	3.1	0.4		2.7
5	0.4	-4.9		5.3	-	-	-	-
6	-1.3	-5.3		4.0	3.1	-0.5		3.6
7	-2.2	-4.0		1.8	4.9	-2.2		7.1
8	-0.4	-8.4		8.0	2.7	-1.8		4.5
9	-4.9	-5.3		0.4	1.1	-1.8		2.9
10	-2.7	-5.3		2.6	-4.0	-4.0		0.0
Mean				3.1				4.2
σ				2.3				2.7

( ) not included in analysis
- image not acquired

Table 3-5 Z_T displacements measured in the left and right lateral fields of course II.

Fraction	Y_T Displacements (mm) Anterior Field				Y_T Displacements (mm) Posterior Field			
	Local L	Verify V		L-V(N)	Local L	Verify V		L-V(N)
		No	Yes			No	Yes	
1	(-3.0)		(0.0)		(-2.6)		(0.0)	
2	-1.1	-6.6		5.5	-1.3	-4.9		3.6
3	1.8	-3.5		5.3	0.0	-3.5		3.5
4	0.5	-7.5		8.0	-2.7	-2.2		-0.5
5	-1.3	-7.5		6.2	-1.3	-3.5		2.2
6	4.5	-5.3		9.8	0.0	-2.2		2.2
7	-1.3	-7.1		5.8	2.7	-3.5		6.2
8	-1.3	-6.4		5.1	-1.8	-3.8		2.0
9	-0.4	-2.9		2.5	-2.2	-3.8		1.6
10	-4.5	-9.9		5.4	-3.1	-6.8		3.7
Mean				6.0				2.7
σ				2.0				1.8

( ) not included in analysis

Table 3-6 Y_T displacements measured in the anterior and posterior fields of course II.

Fraction	Y_T Displacements (mm) Left Lateral Field				Y_T Displacements (mm) Right Lateral Field			
	Local L	Verify V		L-V(N)	Local L	Verify V		L-V(N)
		No	Yes			No	Yes	
1	(-7.0)		(0.0)		(-7.5)		(0.0)	
2	0.0	-1.3		1.3	-1.3	-0.9		-0.4
3	-1.1	-1.8		0.7	0.9	1.3		-0.4
4	-2.2	-3.8		1.6	0.0	-2.6		2.6
5	-0.4	-3.1		2.7	-	-	-	-
6	-3.1	-4.0		0.9	-1.3	-2.6		1.3
7	-1.3	-1.8		0.5	1.3	0.0		1.3
8	-4.4	-2.2		-2.2	0.0	-1.8		1.8
9	-0.4	-4.0		3.6	-3.1	-2.2		-0.9
10	-6.2	-7.5		1.3	-0.9	-5.3		4.4
Mean				1.2				1.2
σ				1.6				1.8

( ) not included in analysis
- image not acquired

Table 3-7 Y_T displacements measured in the left and right lateral fields of course II.

	Mean (mm)	σ *(mm)*	*Range (mm)*	Number of Displacements >10 mm	Number of Displacements > 5 mm
Anterior Field Before Correction	-1.7	11.6	-18.1 to 20.5	8	10
Anterior Field After Correction†	-1.3	5.0	-5.4 to 15.1	1	4
Posterior Field Before Correction	-0.6	3.9	-8.0 to 8.7	0	4
Posterior Field After Correction†	-0.5	3.7	-5.3 to 8.7	0	3

† Results for all fields with and without corrections

Table 3-8 X_T displacements in the AP / PA fields of Course I.

	Mean (mm)	σ *(mm)*	*Range (mm)*	Number of Displacements > 10 mm	> 5 mm
Left Lateral Field (No Correction)	-3.1	1.3	-5.7 to -0.6	0	1
Right Lateral Field (No Correction)	-2.4	2.3	-5.7 to 2.0	0	3

Table 3-9 Z_T displacements in the lateral fields of Course I.

	Mean (mm)	σ *(mm)*	*Range (mm)*	Number of Displacements >10 mm	> 5 mm
Anterior Field Before Correction	0.3	9.4	-12.3 to 17.6	3	6
Anterior Field After Correction†	-1.6	5.6	-5.7 to 11.9	1	4
Posterior Field (No Correction)	-4.0	3.5	-8.0 to 1.7	0	5

† Results for all fields with and without corrections

Table 3-10 X_T displacements in the AP / PA fields of Course II.

	Mean (mm)	σ *(mm)*	*Range (mm)*	Number of Displacements > 10 mm	> 5 mm
Left Lateral Field (No Correction)	-5.4	1.5	-8.4 to -3.1	0	6
Right Lateral Field (No Correction)	-1.7	1.3	-4.0 to 0.4	0	0

Table 3-11 Z_T displacements in the lateral fields of Course II.

	Mean (mm)	σ *(mm)*	*Range (mm)*	Number of Displacements > 10 mm	> 5 mm
Anterior Field (No Correction)	-6.3	2.2	-9.9 to -2.9	0	7
Posterior Field (No Correction)	-3.8	1.4	-6.8 to -2.2	0	1

Table 3-12 Y_T displacements in the AP / PA fields of Course II.

	Mean (mm)	σ *(mm)*	*Range (mm)*	Number of Displacements > 10 mm	> 5 mm
Left Lateral Field (No Correction)	-3.3	1.9	-7.5 to -1.3	0	1
Right Lateral Field (No Correction)	-1.8	2.0	-5.3 to 1.3	0	1

Table 3-13 Y_T displacements in the lateral fields of Course II.

	Course I		Course II		Course II		Course II		Course II	
	AP/PA	RL/LL	AP/PA	RL/LL	AP/PA	RL/LL	AP/RL	AP/LL	PA/RL	PA/LL
	X_T	Z_T	X_T	Z_T	Y_T	Y_T	Y_T	Y_T	Y_T	Y_T
D	0.20	0.28	0.50	0.80	0.67	0.38	0.86	0.67	0.63	0.33
Prob.	0.93	0.49	0.27	0.00	0.04	0.63	0.00	0.04	0.09	0.70

Table 3-14 Kolmogorov-Smirnov statistic applied to the same displacement as measured from two separate fields.

	Course I				Course II				Course II			
	AP	PA	RL	LL	AP	PA	RL	LL	AP	PA	RL	LL
	X_T	X_T	Z_T	Z_T	X_T	X_T	Z_T	Z_T	Y_T	Y_T	Y_T	Y_T
D	0.38	0.35	0.22	0.33	0.17	0.25	0.88	0.67	0.89	0.78	0.50	0.44
Prob.	0.63	0.24	0.77	0.27	1.00	0.96	0.00	0.04	0.00	0.01	0.27	0.34

Table 3-15 Kolmogorov-Smirnov statistic applied to displacements measured from localization and verification images of the same field excluding those fractions were a correction was applied

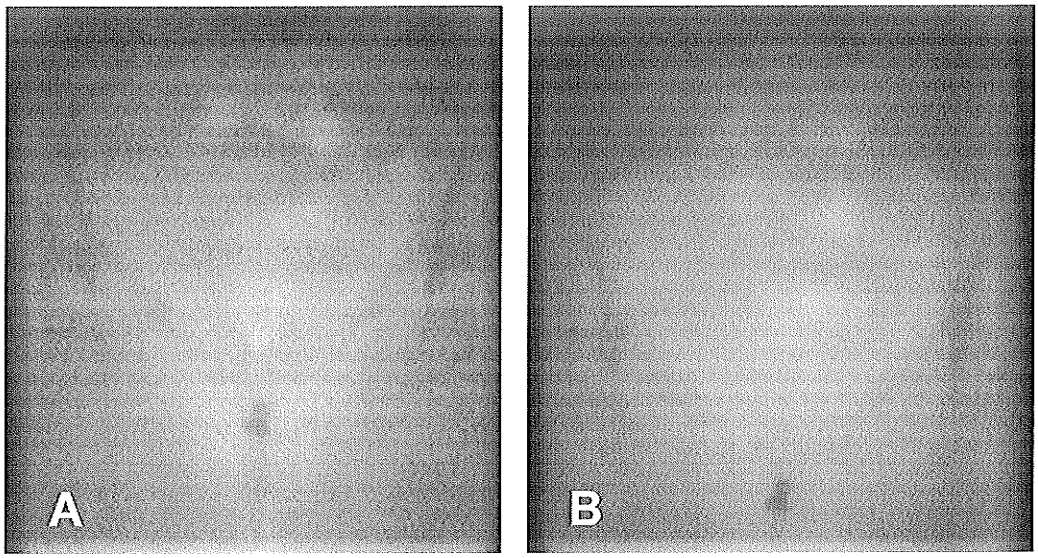

Figure 3-1 (A) An initial localization image acquired of the anterior field during the first (simulation) fraction for course I. After review by the oncologist, field size and position were specified and the patient was realigned accordingly. The approved image (B) serves as the prescription to which subsequent images are compared.

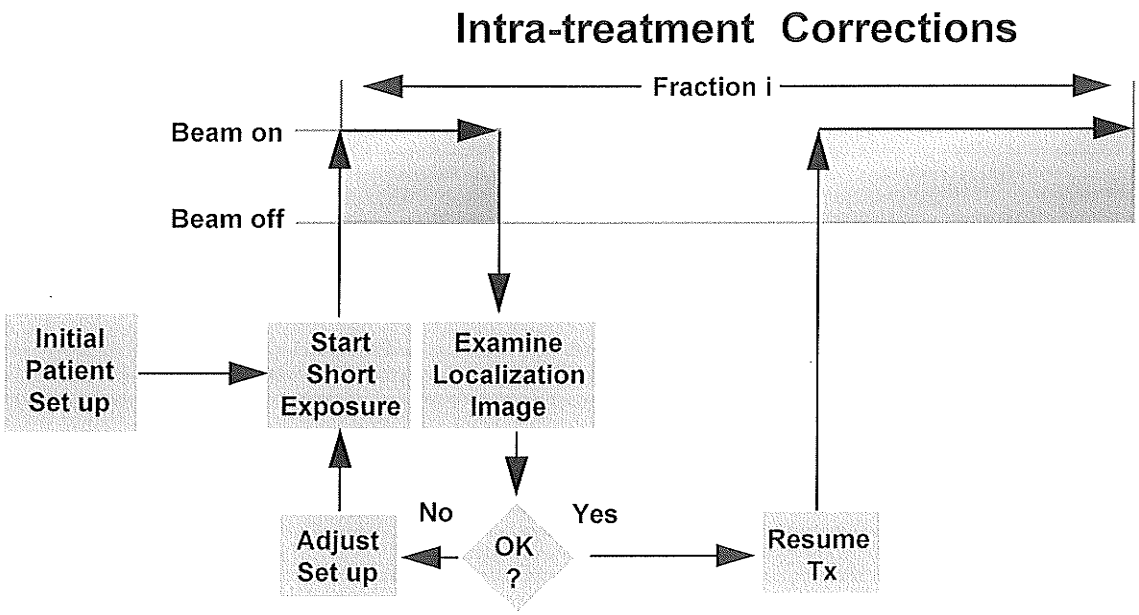

Figure 3-2 A schematic diagram showing the intra-treatment verification procedure.

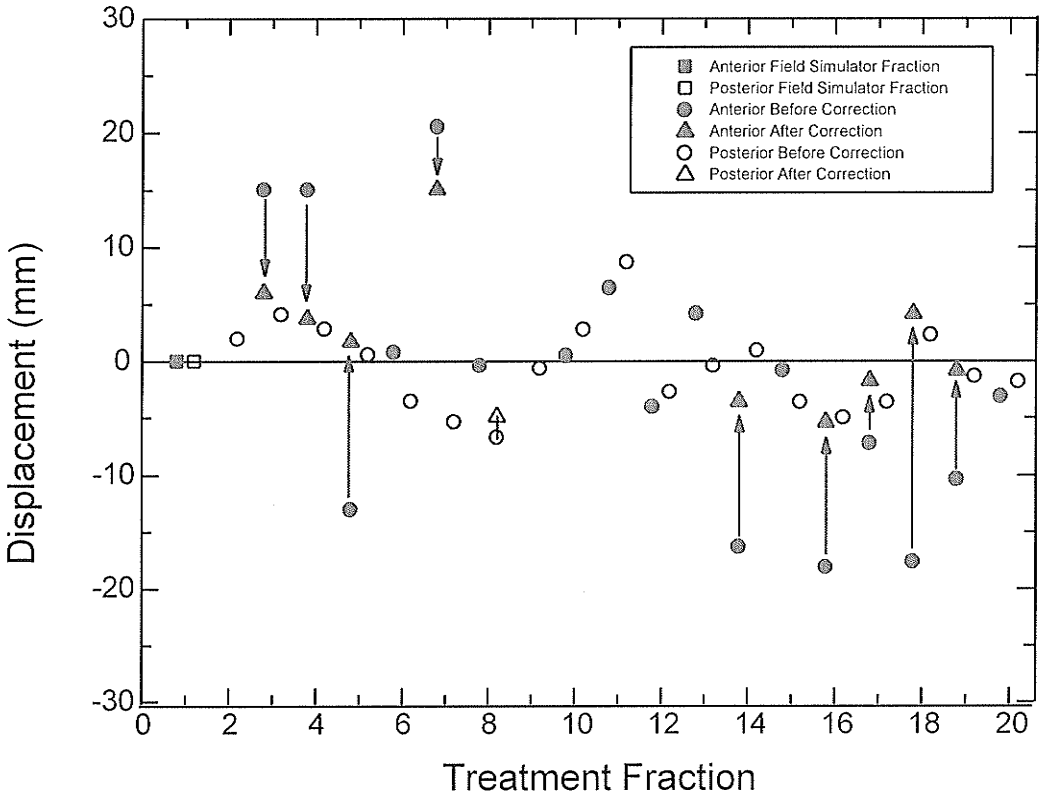

Figure 3-3 A displacement plot for the anterior and posterior fields of course I showing measured displacements prior to and after intra-treatment corrections. The arrows indicate the direction of a corrective action.

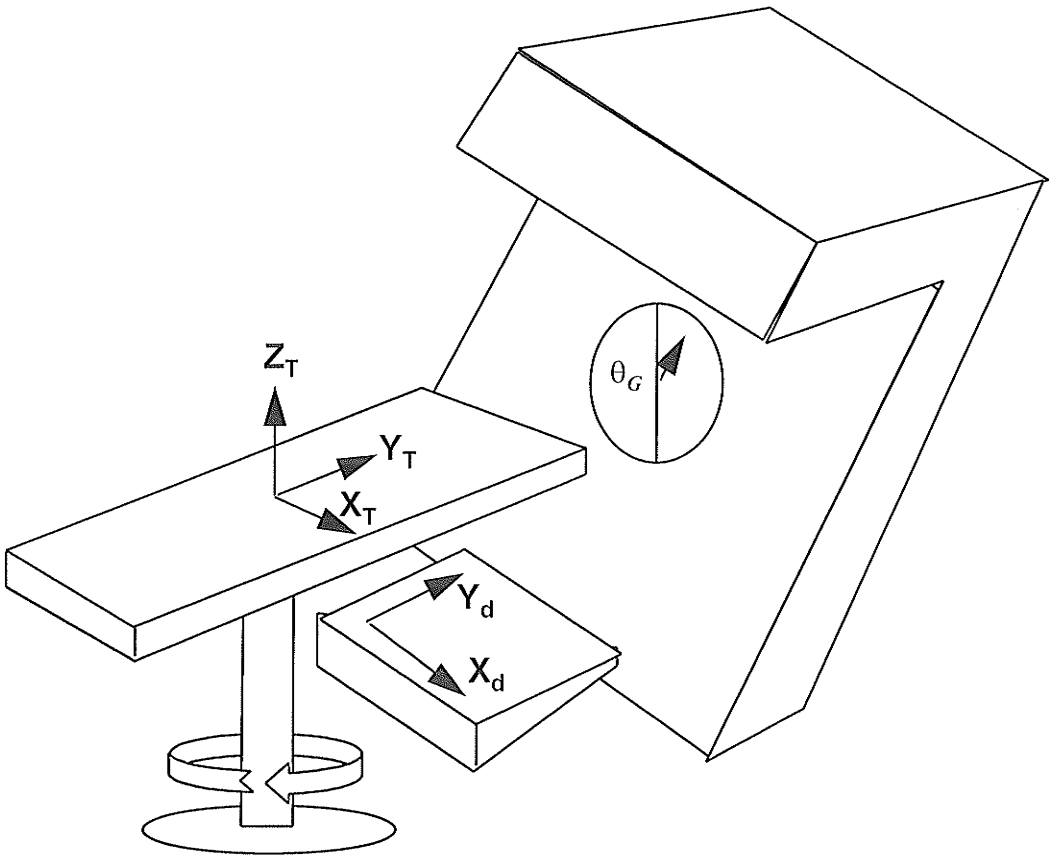

Figure 3-4 The coordinate system used for measuring setup displacements. X_T, Y_T and Z_T are treatment couch coordinates relative to the isocenter, and X_d and Y_d are coordinates of the portal imaging device.

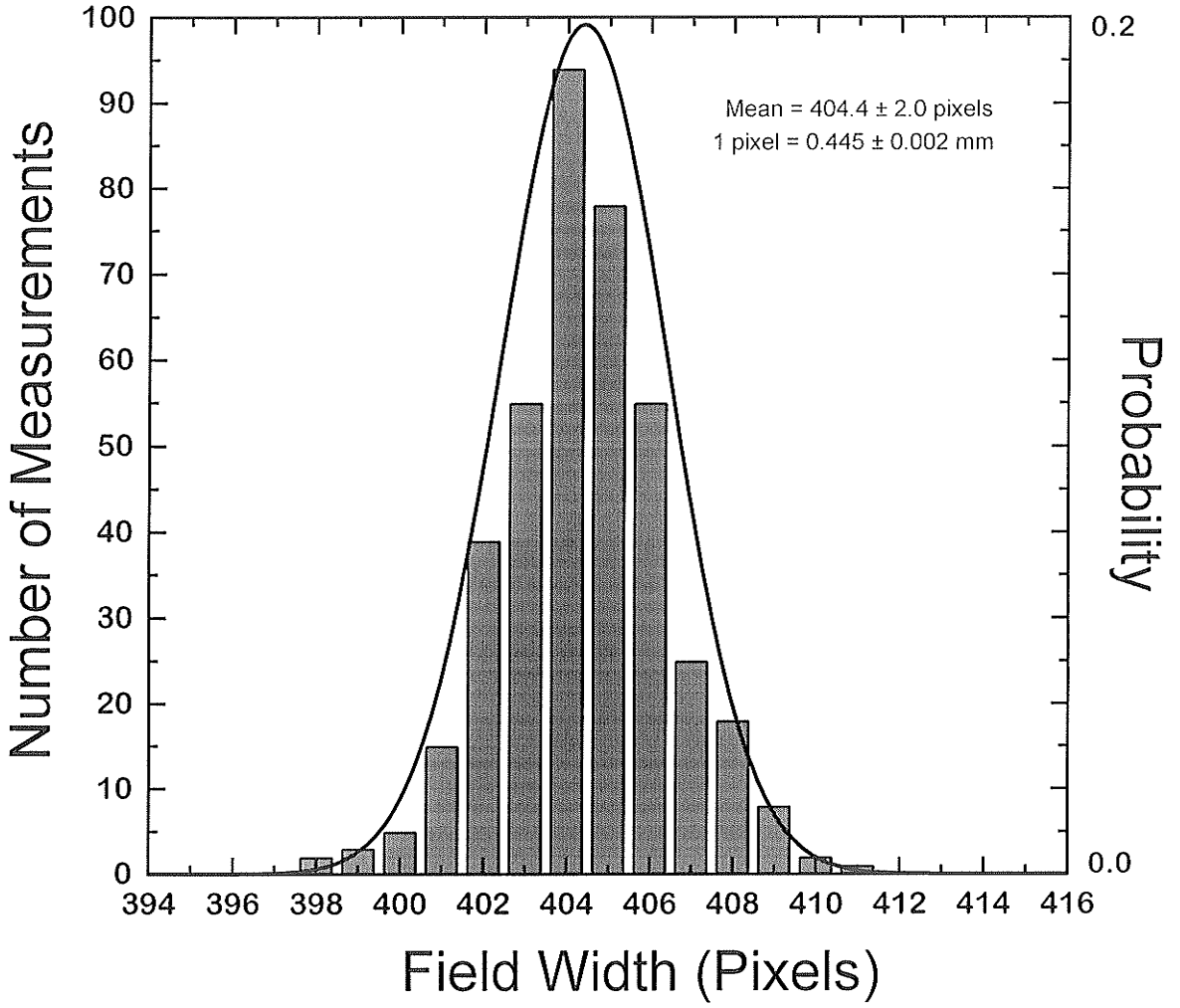

Figure 3-5 Images were calibrated by equating field dimensions in pixels to the known field size in mm. A histogram of the results shows that the width of a pixel was 0.445 ± 0.002 mm.

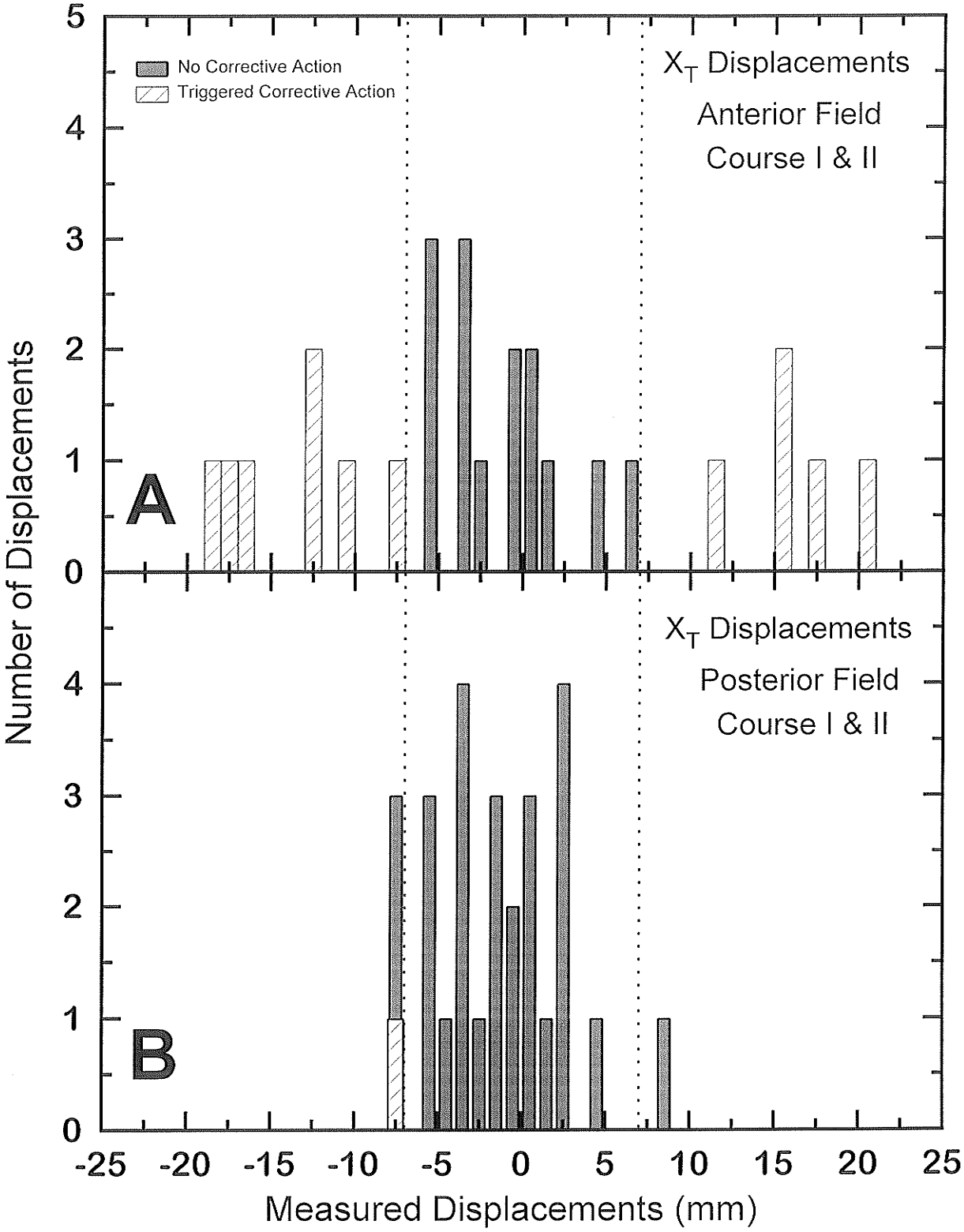

Figure 3-6 A histogram of X_T displacements for (A) the anterior fields and (B) the posterior fields of course I and II of treatment before corrective intervention.

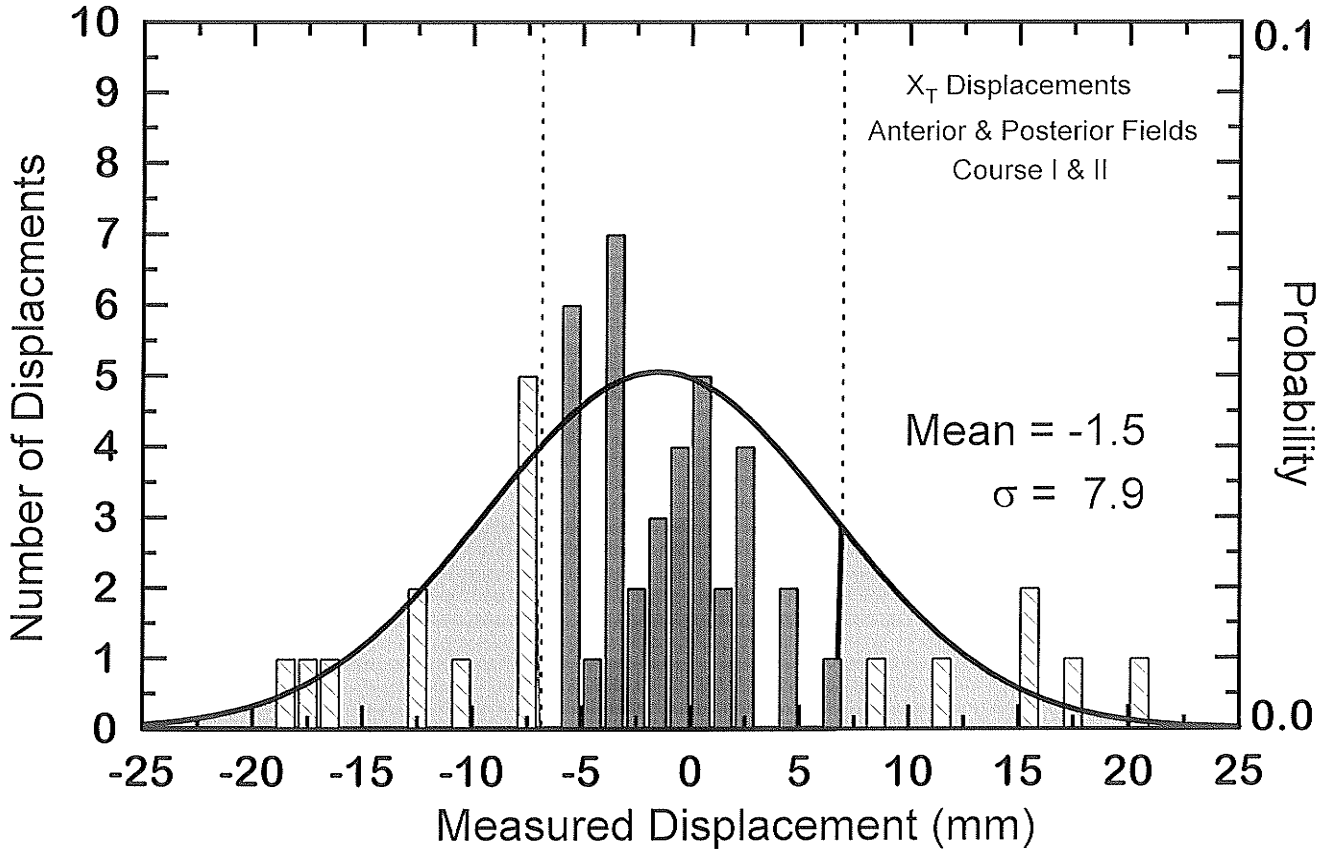

Figure 3-7 The X_T displacements for the anterior and posterior fields of course I and II of treatment before corrective intervention was taken.

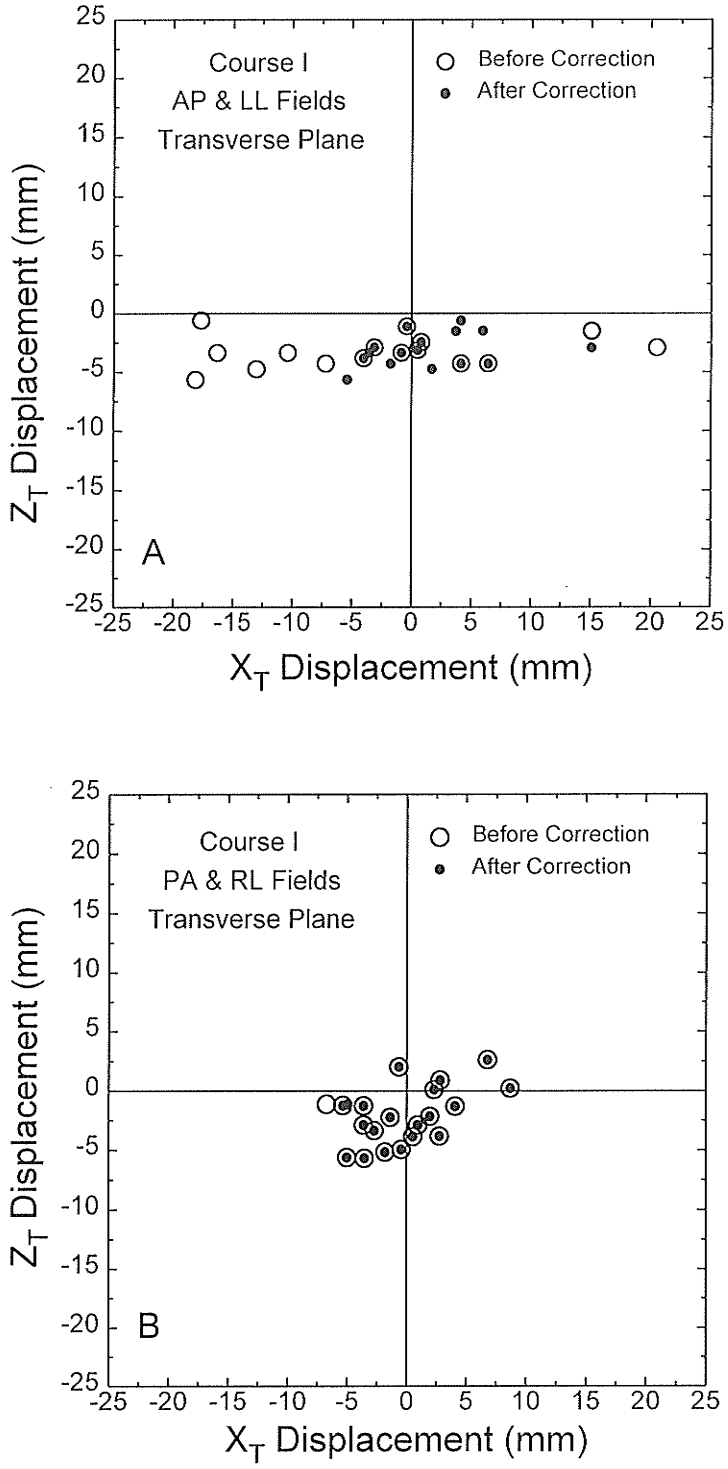

Figure 3-8 Two dimensional displacement plots in the transverse plane derived from measurements of the AP, PA and lateral fields of course I, excluding the simulation fraction. See text for details.

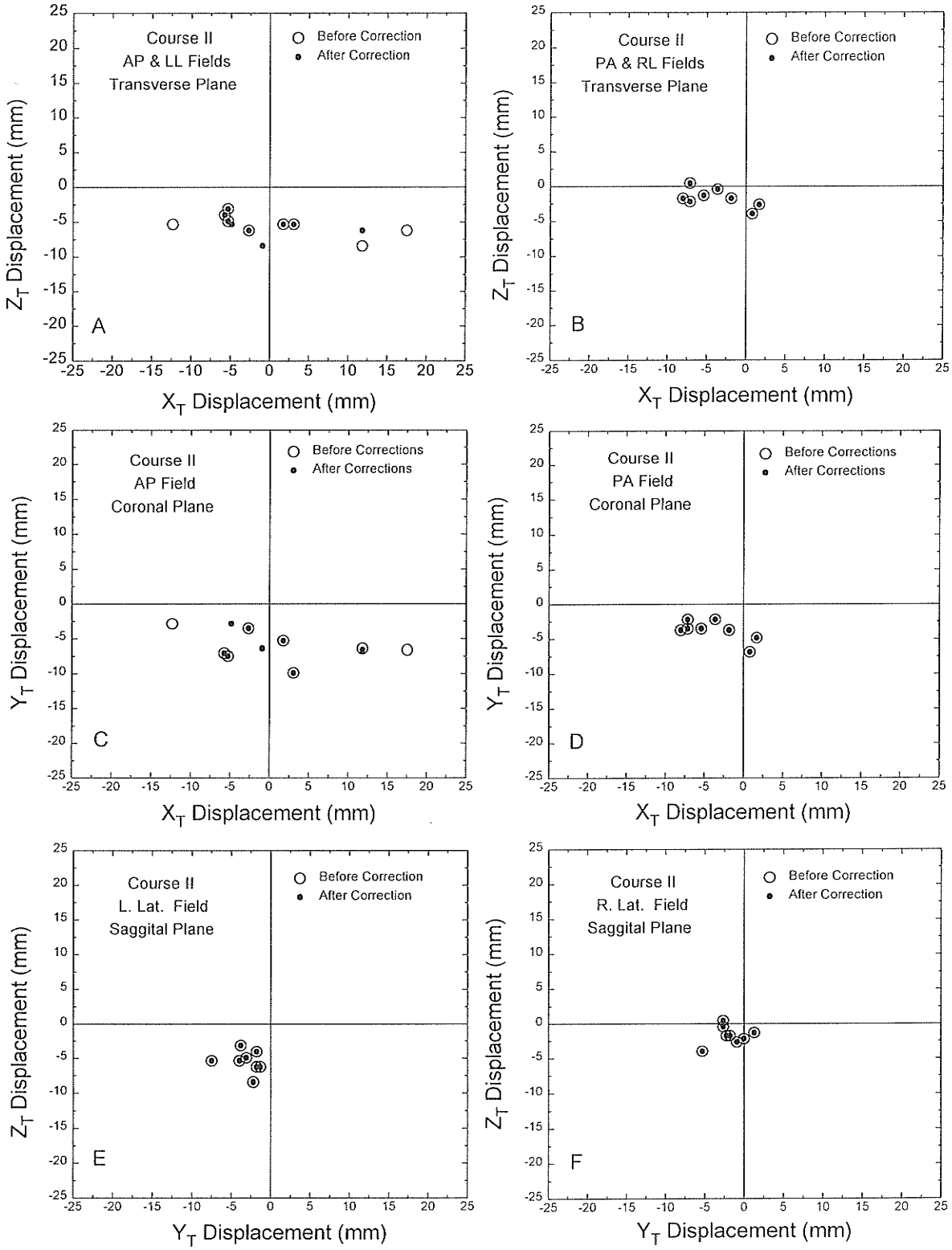

Figure 3-9 Displacement plots derived from measurements of the AP, PA and lateral fields of course II, excluding the simulation fraction. See text for details.

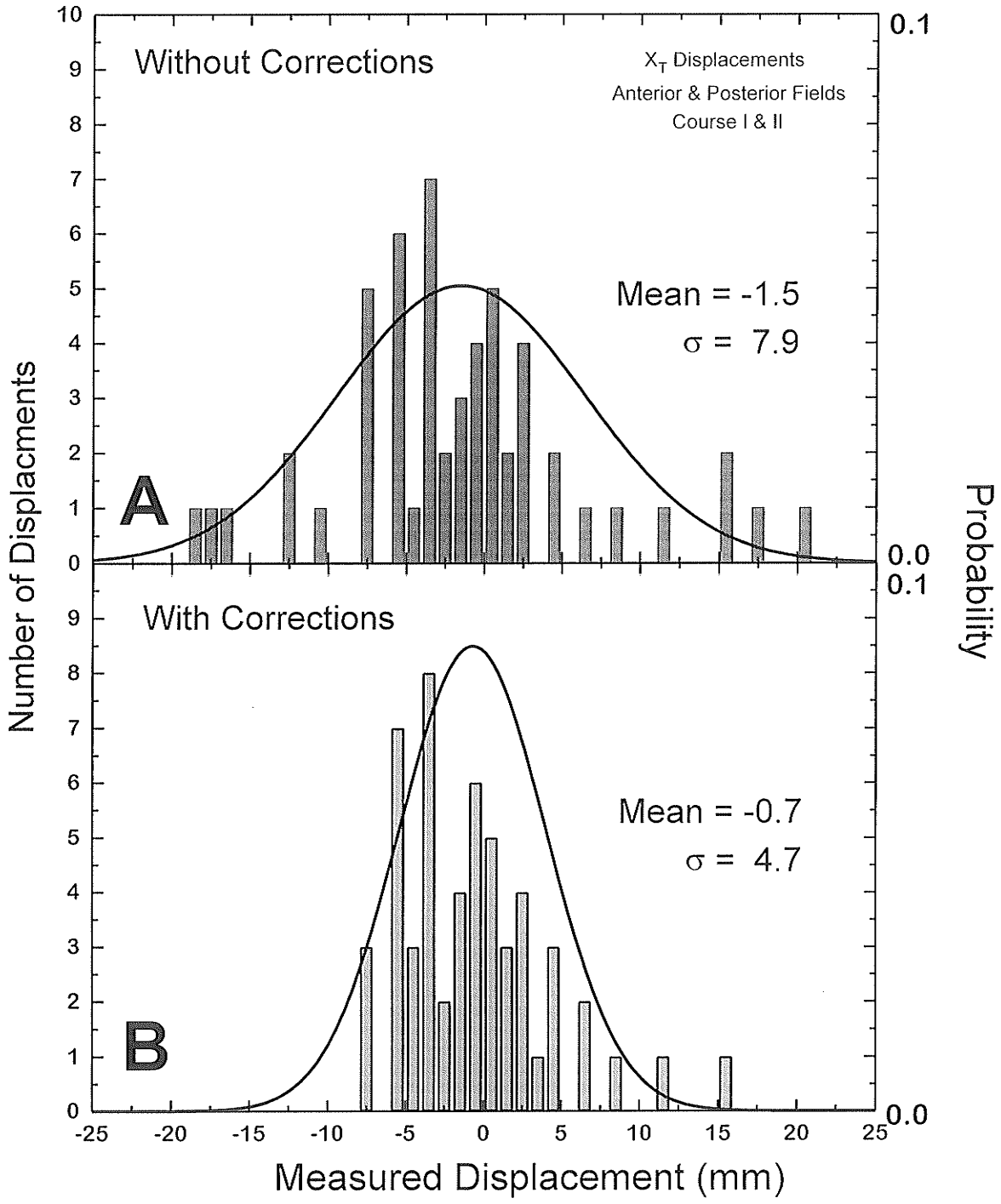

Figure 3-10 The distribution of measured X_T displacements for all treatment fractions excluding the simulator fraction (A) before corrective action was taken and (B) after corrections were applied.

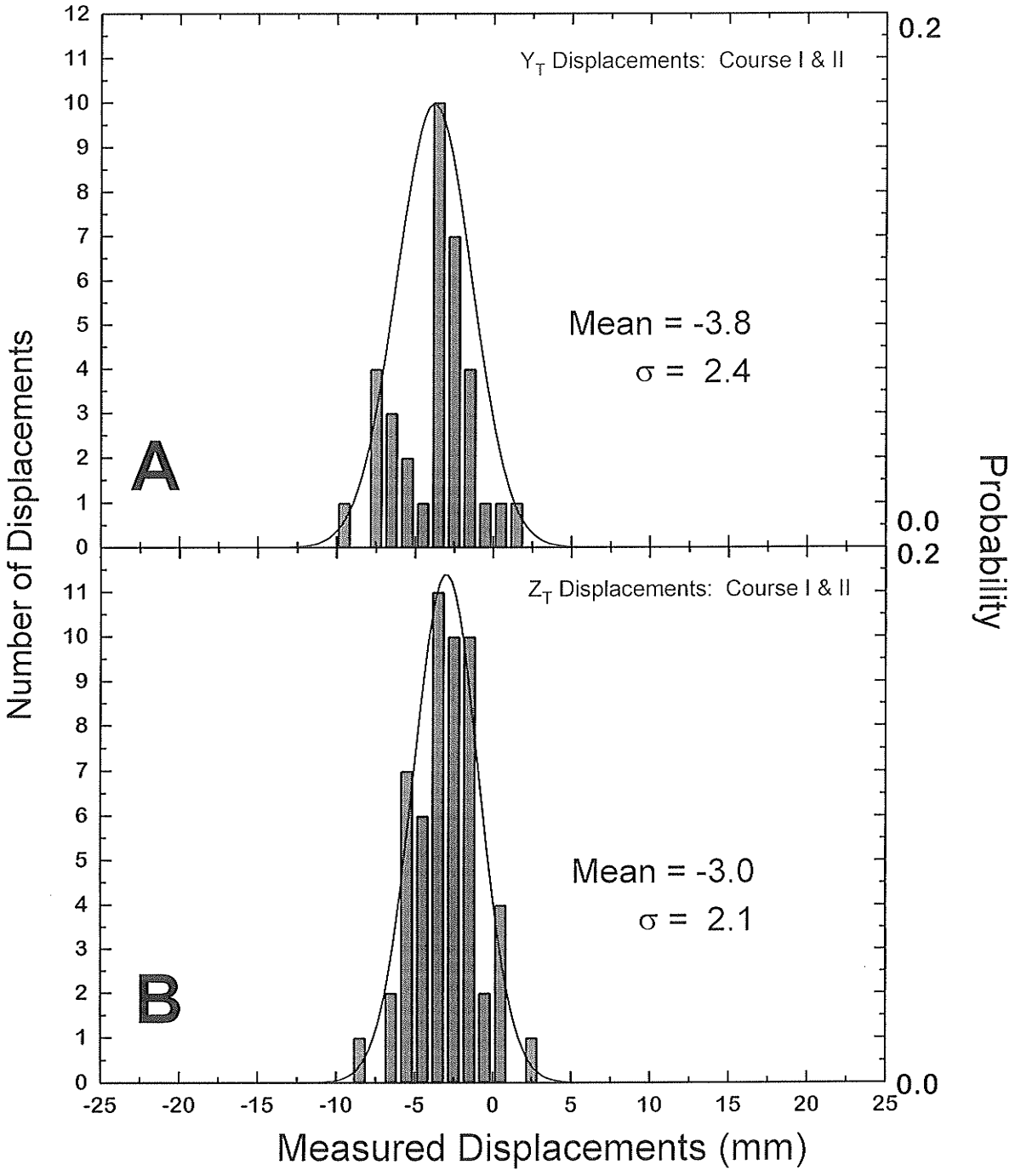

Figure 3-11 The distribution of measured (A) Y_T and (B) Z_T displacements for all treatment fractions excluding the simulator fraction. No corrective action was deemed necessary for displacements measured in these directions.

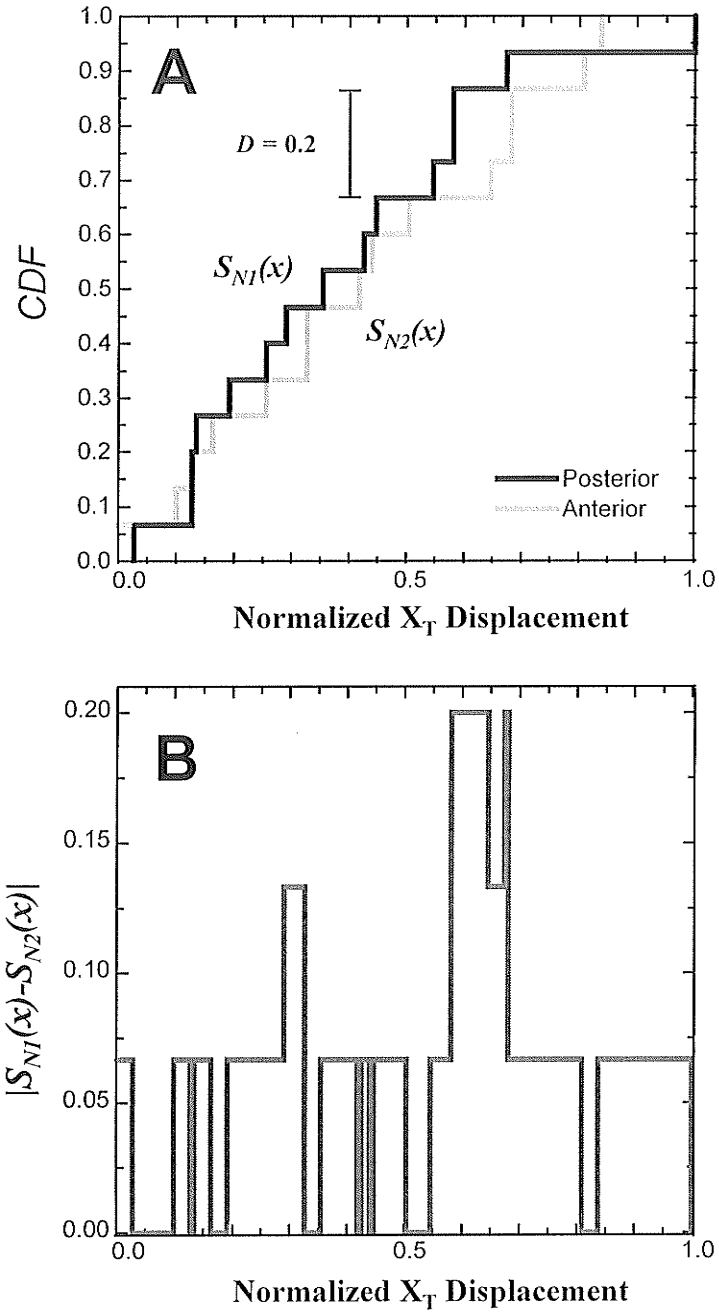

Figure 3-12 (A) A plot of the Kolmogorov-Smirnov statistical test applied to the X_T displacements in the anterior and posterior fields of course I and (B) the absolute difference between the two distributions.

Chapter 4

Tumor localization through the detection of radio-opaque implanted markers

4.1 Introduction

The effectiveness of a radiotherapy treatment ultimately depends on the accuracy and the reproducibility of the dose delivered to the target volume during a protracted fractionation schedule. Many factors can give rise to discrepancies between the prescribed and delivered distributions to the target volume, such as systematic or random field placement errors as well as machine parameter and human errors, all of which may decrease local tumor control[1,2] and increase normal tissue complication[3]. Through the routine acquisition of portal films or electronic portal images, a number of studies[4-8] have shown that these types of errors can be significantly reduced, so that the ±5% limit on accuracy of the delivered target dose recommended[9] by ICRU report 24 may be achievable.

Ideally, electronic images or portal films of patient set up are acquired during treatment and are compared to a simulator film at which time a decision is made possibly involving corrective intervention in the form of intra or inter-treatment corrections.

Intra-treatment correction involves acquiring a portal film or image with a small fraction of the daily dose, at which time the treatment is stopped. The image is compared to a simulator film and a decision is made as to the accuracy of patient setup. If setup is deemed acceptable, the remainder of the treatment dose is delivered. If setup is deemed unacceptable, the patient is repositioned in the treatment beam and a second portal film or image is acquired.

The inter-treatment correction involves acquiring a portal film or image with the entire daily dose and if patient setup is deemed unacceptable, a correction made at the start of the next treatment fraction.

Bony landmarks are commonly used as reference points when verifying patient setup as tumor volumes are not easily visualized on megavoltage images. However, the position of the tumor may not be rigidly fixed with respect to the underlying bony anatomy. Recent studies[10-12] involving patients being treated for localized prostate cancer found large day to day variations in the position of the tumor in relation to the underlying bony anatomy. A megavoltage portal film study conducted by Balter et al.[13] measured the movement of the prostate with respect to the bony anatomy in 10 patients over the course of treatment. The maximum measured displacement was 7.5 mm although typical displacements were in the range 0 to 4 mm. A CT based study conducted by Ten Haken et al.[14] also observed movement of the prostate and found that it is directly related to the

level of rectal and bladder filling, the consequences of which are increased dose to the rectum and bladder and a decreased dose to the prostate and seminal vesicles.

The deleterious effects of unpredictable prostate movement can adversely affect the outcome of a radiotherapy treatment. Therefore some investigators[12,13,15] are studying the effectiveness of radio-opaque implanted markers as an aid in identifying inter-treatment movements of the prostate gland over the course of radiotherapy. The results show that the information provided by the implant markers can be used to determine optimally sized margins for any particular patient.

The use of radio-opaque markers is not limited to sites involving the prostate but have also been used in areas where extreme accuracy is required in tumor volume localization. Jones et al.[16] use gold wires and titanium screws, which are embedded in the skull of a patient, to accurately localize brain lesions for stereotactic radiotherapy. The markers serve as a reference coordinate system from which the position of the lesion is determined through a CT or angiographic imaging procedure. The same markers are imaged with an orthogonal pair of diagnostic x-ray films just prior to treatment. A computer program uses the marker coordinate information to calculate the couch translations and rotation necessary to bring the tumor to the prescribed location in the beam. The accuracy in dose delivery of this method in the clinical setting can only estimated but similar megavoltage phantom studies using two film methods have been conducted[17,18] and demonstrate sub-millimeter accuracy in target localization.

Although the use of radio-opaque markers is attractive in the sense that the accuracy to which a patient may be set up is quite good, the prolonged processing and analysis procedures limit their routine use. Jones et al.[16] state that a typical treatment takes about 45 minutes as compared to conventional treatments which are performed in about 10-15 minutes.

The increase in availability of electronic portal imaging devices (EPIDs) has opened up a variety of new possibilities for verification techniques incorporating radio-opaque markers. The digital image data provided by an EPID is accessible immediately after image acquisition allowing the host computer to rapidly calculate the necessary translations and rotations required to align the patient in the treatment beam therefore allowing the intra-treatment form of correctional intervention to be applied. Complete automation for intra-treatment verification would involve the acquisition of short localization images at the start of each fraction, detection of the radio-opaque markers within the images, calculation of the required translations / rotations and delivery of the remaining dose to the target volume. This entire procedure would not be expected to take much longer than a conventional treatment, therefore minimizing discomfort to the patient while maximizing the therapeutic benefit as a result of the greater precision in target volume localization.

Although the implementation of EPIDs seems to be the next logical step towards complete automation, radio-opaque markers visible on diagnostic films are difficult to see in megavoltage portal images. Increasing the size of radio-opaque implants can increase their visibility in portal images but this option may not always be clinically acceptable.

The remainder of this chapter examines a digital image processing technique that has been developed for detecting radio-opaque markers in megavoltage portal images. A variety of markers were chosen including the titanium screws used by Jones et al. in their high precision stereotactic treatments. A phantom was constructed into which the markers were embedded and treatment conditions were simulated by enclosing the phantom in a tissue equivalent buildup material. A range of phantom images were acquired with different doses of radiation and each was analyzed for accuracy in marker location using a computer algorithm designed specially for this purpose.

4.2 Materials and methods

A contrast detail phantom was constructed for this study from a 17 x 17 x 1.2 cm^3 Delrin (Acetal) plate in which several radio-opaque markers are embedded as shown in Fig. 4-1. The six steel ball bearings have diameters 1.6, 3.2, 4.8, 6.4, 7.9 and 9.5 mm and are situated above a tungsten bar which locates their absolute positions on the megavoltage images of the phantom. The three tungsten pins each have a length of 6.4 mm and diameters of 1.6, 2.4 and 3.2 mm and are oriented with their major axis perpendicular to

the plane of the phantom. The three gold pins each have a diameter 1.8 mm and length 3.2 mm and are aligned orthogonal to each other with two lying in the plane of the phantom. The two titanium screws have a 4 mm head diameter, a 3 mm diameter barrel and a length of 5 mm. Inserted in the center of each titanium screw is a 1 mm diameter by 3 mm long gold pin whose purpose is to increase contrast of the screws in megavoltage images (Z(Au) = 79 Z(Ti) = 22). Also embedded in the phantom are three tungsten rings which were not used in this study.

Testing was performed on a Siemens dual energy KD2 linear accelerator equipped with a BEAMVIEW^{PLUS} on-line portal imaging system*. Treatment conditions were simulated by inserting the contrast detail phantom between two 10 cm slabs of tissue equivalent material and aligning it to isocenter as shown if Fig. 4-2. The tissue equivalent material simulates scattering properties encountered in conventional radiotherapy treatments and introduces a considerable amount of noise into the digital images.

The linac was configured for a 15 x 15 cm^2 field and images were acquired at energies of 6 and 23 MV (dose rates of 200 and 300 cGy/min at isocenter respectively). Automatic analysis of patient setup would require the acquisition of acceptable quality localization images at the start of each treatment session by delivering a small fraction of the daily dose. These images are usually acquired by averaging a number of video frames to improve the signal to noise ratio. For this study, images containing averages of 16, 32,

* Siemens Medical Systems, Concord, CA.

48, 64, 80, 96, 112 and 128 video frames were acquired with nominal and actual phantom doses as listed in Table 4-1, where the nominal and phantom doses are defined as the dose to the phantom in the absence and presence of the tissue equivalent material respectively. The phantom dose can be determined following the isocentric dosimetric calculation technique outlined in Khan[19] and using tabulated data measured for the treatment linac for the configuration shown in Fig. 4-2,

$$Dose(cGy) = Dose\,Rate(cGy/min)\cdot t(min)\cdot S_c(E,r)\cdot TPR(E,r,d) \qquad (1)$$

where $S_C(E,r)$ and $TPR(E,r,d)$ are the collimator scatter factor and tissue phantom ratio measured as a function of energy E, field size r and depth d. Referenced to the RS-170 standard[†] video rate of 30 frames per second, t specifies the length of time required to average the single video frames to form the localization image. For the configuration shown in Fig. 4-2, the collimator scatter factors were found to be 1.03 for both the 6 and 23 MV beams while the tissue phantom ratios were found to be 0.8 and 0.9 for 6 and 23 MV respectively. Verification images acquired with nominal doses of 1.0 Gy for both 6 and 23 MV (phantom doses of 0.82 and 0.93 Gy for 6 and 23 MV respectively) served as the reference images to which all measurements of marker placement were compared. Reproducibility of the measurements was tested by analyzing a series of similar images acquired in rapid succession under identical conditions. The detection algorithm was

[†] 30 frames per second non-interlaced video mode.

tested for susceptibility to noise in regions of a phantom image containing no marker and the number of false occurrences was recorded. Clinical images that contained radio-opaque markers were also analyzed to test performance of the detection algorithm in the presence of anatomical structure within an image.

All deviations of the measured coordinates with respect to the reference coordinates use the standard coordinate system employed at our center as shown in Fig. 4-3.

4.3 The marker detection algorithm

Detection of the implanted markers can be performed either in the spatial or frequency domain. Spatial domain techniques require the convolution of an operator mask with the image containing the markers. The operator mask performs some operation that examines pixel intensities in small neighborhood about it's central pixel and marker pixels are flagged only if a predefined selection criteria is satisfied. Frequency domain techniques involve transforming a marker template and search image into the frequency domain by applying a Fourier Transform. Conveniently, a cross-correlation between the search image and the marker template can be carried out in the frequency domain by applying the correlation theorem[20] which is given by,

$$f(x,y) \circ g(x,y) \Leftrightarrow F^{*}(u,v)G(u,v) \qquad (2)$$

where $f(x,y)$ is the search image, $g(x,y)$ is the marker template image and "$\circ$" represents a correlation in the spatial domain. $F^*(u,v)$ is the complex conjugate of the Fourier Transform of the search image and $G(u,v)$ is the Fourier Transform of the marker template. The correlation theorem as given in Eqn. (2) shows that a correlation $(f(x,y) \circ g(x,y))$ in the spatial domain is equivalent to a simple product in the frequency domain $(F^*(u,v)G(u,v))$. Coordinates of local maxima in the correlation distribution indicate regions of strong correlation between the search image and template and therefore correspond to possible marker positions. Jones and Boyer[21] have investigated a Fourier Transform based cross-correlation technique when applied to prescription and treatment portal images of a Rando head phantom. Images of the phantom were acquired in the correct treatment position and in positions with known translations. The results of the study indicate that this method was able to accurately track one and two dimensional translations.

Although frequency domain techniques have the advantage of reducing the cross-correlation procedure to a simple product in the frequency domain, they have the disadvantage of the extra overhead and processor time involved in performing the Fourier Transform. However, Fast Fourier techniques have been developed which reduce the number of operations required to perform the transform but also require the dimensions of both the search image and template to be powers of 2. In general, the approximate position of a marker within the search image is known and a reasonable square region of interest (ROI) with size 2^n, may be selected about the expected location. This would

considerably reduce the time required to perform the transform as the entire image would not have to be searched. A disadvantage of the spatial domain technique is that the convolution of the operator mask with the search image is also time consuming. However, if a reasonably sized ROI is selected about the expected marker location, detection time can be reduced considerably. The spatial domain technique has the added advantage that it may be easily implemented and optimized on any personal computer and does not require the application of a frequency domain transform. In the study that follows, a spatial domain technique will be developed and tested as a possible means of marker detection in megavoltage images.

The detection algorithm is applied to a ROI about an expected marker position in an image. The ROI is searched to determine which pixels correspond to a point on the marker. The first stage of the detection algorithm consists of smoothing the search ROI with a 3 x 3 average filter to moderate the effects introduced by noise. On a megavoltage image, pixels that correspond to the marker will be darker than the surrounding pixels in a small neighborhood. Pixels that belong to the marker are found by applying an 11 x 11 convolution mask[22] as shown in Fig. 4-4. The central pixel in the mask is tested for gradient against 8 pixels on the mask perimeter. If the gray value of the central pixel is less than all it's 8 neighbors, it is flagged as a possible pin pixel.

The coordinates of all possible pin pixels are recorded and subsequently filtered to eliminate those pixels that have been included as a result of noise. The filtering is

accomplished by convolving a 5 x 5 mask with each flagged pixel in the search region and counting the number of connected neighbors (NCN). NCN is defined here as the number of flagged pixels within the search region that are in contact with the central pixel in the mask. Flagged pixels within the search region not having at least 11 connected neighbors are assumed to be a result of noise and are removed from the collection. If no pixels remain after filtering, the NCN requirement is reduced by 2 and the originally flagged pixels are filtered once again. This process is repeated until at least one marker pixel is found or until a NCN criteria of less than 5 is surpassed. If no pixels are found with at least 5 connected neighbors, the algorithm concludes that there is no marker in the search region.

The remaining marker pixels are used to determine the center of gravity coordinate of the marker by weighting their contributions depending on gray value. The rationale for pixel weighting arises because darker pixels correspond to more central regions of the marker and are less likely to be flagged as a result of noise as compared to the lighter pixels that lie along the edge of the marker. The weighted marker coordinates are given by,

$$x_p = \frac{\sum_{i=1}^{n}(255-m_i)x_i}{\sum_{i=1}^{n}(255-m_i)} \qquad y_p = \frac{\sum_{i=1}^{n}(255-m_i)y_i}{\sum_{i=1}^{n}(255-m_i)} \tag{3}$$

where n is the number of flagged pixels in the ROI about marker p, m_i is the gray value and (x_i,y_i) is the coordinate of flagged pixel I. The image acquisition hardware used for this study sets the value of a black pixel to 0 and a white pixel to 255.

4.4 Results

Images of the contrast detail phantom, acquired at energies of 6 and 23 MV, are shown in Fig. 4-5. Figures 4-5a and 4-5b were acquired at an energy of 6 MV with phantom doses of 1.46 (16 frame average) and 0.82 Gy respectively. The images shown in Figs. 4-5c and 4-5d were acquired at 23 MV with phantom doses of 2.47 (16 frame average) and 0.93 Gy respectively. Marker coordinates measured off the reference images, Figs. 4-5b and 4-5d, are used as the reference values to which all other measurements are compared. It is obvious from Fig. 4-5 that high levels of noise are found in the 16 frame images which makes it difficult to see the smaller markers. It was decided to select two markers for analysis of the algorithm, the first marker chosen is the tungsten pin labeled #1 in Fig. 1 and is visible in the 16 frame images acquired at both energies. The second marker chosen was the titanium screw used by Jones and is labeled #2 in Fig. 1. The screw is visible in neither of the 6 or 23 MV 16 frame images and barely visible in the reference images.

4.4.1 Reproducibility

Reproducibility of the pin detection algorithm was tested by acquiring ten consecutive 16 frame images of the contrast detail phantom at both 6 and 23 MV. No adjustments were made to the phantom position or linac between acquisitions and any differences in the results are due to variations in random noise found in the images. The reproducibility of measurements would therefore be expected to deteriorate with increasing levels of noise. For this reason, the reproducibility of the algorithm was tested on the 16 frame average images as they contained the highest levels of noise of all images acquired and would therefore be expected to return an upper limit on the accuracy of the detection algorithm.

Table 4-2 and 4-3 show the results of the reproducibility test for markers 1 and 2 respectively. The 23 MV images of marker 1 show the best results with standard deviations of 0.13 and 0.18 in the x and y directions respectively. The more accurate results in this case can be attributed to the phantom dose of 2.47 cGy associated with the 16 frame, 23 MV images and therefore the better photon statistics resulting in an improved signal to noise ratio. This increase in accuracy is not noticed for marker 2, the standard deviation for 23 MV is actually larger than in the corresponding 6 MV image. Although marker 2 is not visible in either the 6 or 23 MV 16 frame images, there is a slight pixel intensity variation at it's position which is not clearly visible. The algorithm was still able to locate the marker in each image with a sub-millimeter accuracy.

4.4.2 Marker Positional Accuracy

Marker positional accuracy was tested by measuring the coordinates of markers 1 and 2 from the 16, 32, 48, 64, 80, 96, 112 and 128 frame averaged images and comparing these results to those measured from the reference images.

Tables 4-4 and 4-5 show the results of the positional accuracy test for markers 1 and 2 respectively. Marker 1 showed maximum deviations from the reference coordinate equal to 0.18 and 0.44 mm for the 6 and 23 MV images respectively while no deviations were found in those images averaged from 48 frames or more. Marker 2 showed slightly larger maximum deviations of 0.40 and 0.91 mm for the 6 and 23 MV images respectively. For the range of frame averaged images tested, the deviations measured for marker 2 did not converge to the reference value as they did for marker 1. This is due to the small signal associated with marker 2 which makes it more susceptible to random noise in the images. However, the sub-millimeter precision is quite adequate for determining the marker location.

4.4.3 False Marker Detection

The influence of noise alone may also trigger false marker detections. To test the algorithms susceptibility to noise, a ROI was setup over a region of the phantom image

that did not contain any radio-opaque marker. The same ROI was analyzed for the entire range of frame averaged images and the number of false detections was monitored.

Table 4-6 shows the number of false detections observed in the 6 and 23 MV images. The algorithm performed the poorest on the 16 frame average image acquired at 6 MV. Two false positive were obtained while in the entire range of 23 MV images, only 1 false positive result was observed. This is to be expected as the 23 MV (300 cGy/min) beam has better photon statistics than the 6 MV (200 cGy/min) beam. A total of 5 false positive responses were observed in the 6 MV images as compared to only 1 in the 23 MV images. From tables 4-1 and 4-6, the minimum phantom dose required per image, at which no false positive responses were observed, was found to be 7.32 cGy at 6 MV and 4.94 cGy at 23 MV.

4.4.4 Clinically Significant Results

The contrast detail phantom constructed for use in this study is convenient for testing a variety of radio-opaque markers but cannot simulate the random superposition of anatomical structure found in clinical images. A preliminary test was performed using a small clinical phantom constructed with a Styrofoam SM block containing a combination radio-opaque markers as shown in Fig. 4-6. The block was placed at a SSD about 90 cm on the skin of a 72 year old patient being treated for cancer of the prostate at 23 MV. Figures 4-7a and Fig. 4-7b show the anterior localization and reference images acquired

with tumor doses of about 1.2 and 46 cGy respectively. Table 4-7 lists the deviations in measurements between the localization and reference images for markers 1 through 5 as shown in Fig. 4-7. Sub-millimeter accuracy was found for all markers in the particular test which approximates the clinical situation to a higher degree than by simply acquiring images of the contrast detail phantom described earlier. However, implanted radio-opaque markers may behave differently than the ideal situation set up here and therefore more analysis is required.

4.5 Conclusions

Radio-opaque implanted markers are currently under investigation in an attempt to verify treatment accuracy in sites where tumor volumes move with respect to the underlying bony anatomy or in sites where high precision is required. The location of lesions can be identified with respect to radio-opaque markers by the careful analysis of an orthogonal set of films of the target volume just prior to treatment. However this process is time consuming and makes it impractical for routine daily use. The complete automation of this verification procedure would require the acquisition of a pair of orthogonal portal images of acceptable quality which can at present be provided by an EPID. Automatic detection of implant markers within the treatment volume can also be carried out in a rapid manner using the EPIDs host computer.

A marker detection algorithm has been developed and has been applied to phantom images containing a variety of radio-opaque markers. Preliminary testing has shown that sub-millimeter accuracy in marker detection is achievable by forming an image with a small fraction of the daily dose and the amount of dose required to form an acceptable image depends on the selection of a suitable radio-opaque marker.

Noise seems to be the largest contributing factor to erroneous results returned from the detection algorithm and this is noticeable to a greater extent in the low dose rate images due to the poorer photon statistics.

Proper implementation of the detection algorithm for any particular EPID and any beam energy would require a calibration procedure. This would consist of tuning the algorithm by analyzing background regions within the treatment field that contain no markers. The detection parameters of the algorithm (mask size, mask weighting and the required number of connected neighbors) should then be adjusted until the number of false observations recorded is reduced to some acceptable value thereby minimizing the sensitivity of the algorithm to noise. For example, increasing the requirement on the number of connected neighbors decreases the sensitivity of the algorithm to noise, however small markers may be overlooked in the process. The mask weighting may be adjusted by requiring the central pixel to be greater than some multiple of the surrounding pixels thereby decreasing sensitivity to noise.

Detection of the radio-opaque markers in clinical images also showed sub-millimeter accuracy although a somewhat artificial situation was implemented to test the algorithm. However, by placing the markers on the exterior surface of the patient, markers were nevertheless still superimposed over anatomical structures showing the ability of the algorithm to pick the marker out of a complex background.

The continued development of EPID technology through the use of high quality CCD cameras will no doubt allow the acquisition of much higher quality images with smaller doses of radiation. A greater precision in marker detection will be achievable which will ultimately lead to greater tumor control probabilities along with less patient discomfort.

References

1. M. Goitein and J. Busse, "Immobilization error: Some theoretical considerations," Radiology **177,** 407-412 (1975).

2. A. Dutreix, "When and how can we improve precision in radiotherapy," Radiother. Oncol. **2,** 275-292 (1984).

3. K. Mah, J. Van Dyk, T. Keane and P. Y. Poon, "Acute radiation-induced pulmonary damage: A clinical study on the response to fractionated radiation therapy," Int. J. Radiat. Oncol. Biol. Phys **13,** 179-188 (1987).

4. J. E. Marks, A. G. Haus, H. G. Sutton and M. L. Griem, "The value of frequent treatment verification films in reducing localization error in the irradiation of complex fields," Cancer **37,** 2755-2761 (1976).

5. R. W. Byhardt, J. D. Cox, A. Hornburg and G. Liermann, "Weekly localization films and detection of field placement errors," Int. J. Radiat. Oncol. Biol. Phys. **4,** 881-887 (1978).

6. I. Rabinowitz, J. Broomberg, M. Goitein, K. McCarthy and J. Leong, "Accuracy of radiation field alignment in clinical practice," Int. J. Radiat. Oncol. Biol. Phys. **11,** 1857-1867 (1985).

7. S. E. Griffiths, G. G. Khoury and A. Eddy, "Quality control of radiotherapy during pelvic irradiation," Radiother. Oncol. **20,** 203-206 (1991).

8. W. De Neve, F. van den Heuvel, M. Coghe, D. Verellen, M. De Beukeleer, A. Roelstraete, P. De Roover, L. Thon and G. Storme, "Interactive use of on-line portal imaging in pelvic radiation," Int. J. Radiat. Oncol. Biol. Phys. **25,** 517-524 (1993).

9. ICRU Report #24, *Determination of absorbed dose in a patient irradiated by beams of X or Gamma rays in radiotherapy procedures*, (International Commission on Radiation Units and Measurements, Washington, D.C., 1976).

10. C. Beard, M. R. Bussiere, M. E. Plunkett, N. Coleman and P. Kijewski, "Analysis of prostate and seminal vesicle motion," Int. J. Radiat. Oncol. Biol. Phys. **27,** 136 (1993).

11. J. D. Forman, C. F. Mesina, T. He, E. Ben-Josef, C. Pelizzari, S. Vijayakumar and G. T. Chen, "Evaluation of changes in the location and shape of the prostate and rectum during a seven week course of conformal therapy," Int. J. Radiat. Oncol. Biol. Phys. **27,** 222 (1993).

12. J. Balter, H. M. Sandler, K. Lam, R. L. Bree, A. S. Lichter and R. K. Ten Haken, "Measurement of prostate motion over the course of radiotherapy," Int. J. Radiat. Oncol. Biol. Phys. **27,** 222 (1993).

13. J. M. Balter, H. M. Sandler, K. Lam, R. L. Bree, A. S. Lichter and R. K. Ten Haken, "Measurement of prostate movement over the course of routine radiotherapy using implanted markers," Int. J. Radiat. Oncol. Biol. Phys. **31,** 113-118 (1995).

14. R. K. Ten Haken, J. D. Forman, D. K. Heimburger, A. Gerhardsson, D. L. McShan, C. Perez-Tamayo, S. L. Schoeppel and A. S. Lichter, "Treatment planning issues related to prostate movement in response to differential filling of the rectum and bladder," Int. J. Radiat. Oncol. Biol. Phys. **20,** 1317-1324 (1991).

15. H. M. Sandler, R. L. Bree, P. W. McLaughlin, H. B. Grossman and A. S. Lichter, "Localization of the prostatic apex for radiation therapy using implanted markers," Int. J. Radiat. Oncol. Biol. Phys. **27,** 915-919 (1993).

16. D. Jones, D. A. Christopherson, J. T. Washington, M. D. Hafermann, J. W. Rieke, J. J. Travaglini and S. S. Vermeulen, "A frameless method for stereotactic radiotherapy," Br. J. Radiol. **66,** 1142-1150 (1993).

17. K. L. Lam and R. K. Ten Haken, "Improvement of precision in spatial localization of radio-opaque markers using the two-film technique," Med. Phys. **18,** 1126-1131 (1991).

18. K. L. Lam, R. K. Ten Haken, D. L. McShan and A. F. Thornton, "Automated determination of patient setup errors in radiation therapy using spherical radio-opaque markers," Med. Phys. **20,** 1145-1152 (1993).

19. F. M. Khan, *The Physics of Radiation Therapy,* (Williams & Wilkins, London, 1994).

20. R. C. Gonzalez and R. E. Woods, *Digital Image Processing,* (Addison-Wesley Publishing Company, New York, 1992).

21. S. M. Jones and A. L. Boyer, "Investigation of an FFT-based correlation technique for verification of radiation treatment setup," Med. Phys. **18,** 1116-1125 (1991).

22. K. B. Luchka and R. Gordon, *A Mathematical Approach to Biology, Chapter 13: Solitary mechanical waves during early embryonic development. Jean, R.V. (ed.),* (Steven Wuerz Publishing, Winnipeg, Mb., 1995).

Frames Averaged	Dose (cGy) @ 6 MV		Dose (cGy) @ 23 MV	
	Nominal	Phantom	Nominal	Phantom
16	1.78	1.46	2.67	2.47
32	3.56	2.93	5.33	4.94
48	5.33	4.39	8.00	7.42
64	7.11	5.85	10.67	9.89
80	8.89	7.32	13.33	12.36
96	10.67	8.78	16.00	14.83
112	12.44	10.24	18.67	17.30
128	14.22	11.71	21.33	19.78

Table 4-1 The nominal and actual dose to the contrast detail phantom.

Trial #	Marker #1: Deviation from Reference			
	6 MV		23 MV	
	x (mm)	y (mm)	x (mm)	y (mm)
1	0.06	-0.18	0.00	-0.04
2	0.11	0.53	0.00	0.22
3	-0.06	-0.40	0.23	0.09
4	0.57	0.44	0.06	0.09
5	-0.06	-0.18	0.00	0.04
6	-0.68	0.97	0.06	-0.04
7	-0.06	-0.09	0.06	-0.22
8	-0.51	-0.26	0.00	0.00
9	0.00	0.35	-0.29	0.44
10	0.00	-0.26	-0.06	-0.04
Mean	-0.06	0.09	0.01	0.05
σ	0.34	0.45	0.13	0.18

Table 4-2 Reproducibility test for marker #1.

Trial #	Marker #2: Deviation from Reference			
	6 MV		23 MV	
	x (mm)	y (mm)	x (mm)	y (mm)
1	0.00	-0.35	0.46	-0.62
2	0.00	-0.31	-0.34	0.35
3	0.34	-0.26	-0.23	0.88
4	-0.40	0.48	-0.06	0.31
5	0.00	-0.13	0.40	-0.84
6	0.17	0.48	0.68	0.26
7	-0.17	-0.53	-0.23	-0.09
8	-0.86	-0.13	0.17	-0.04
9	-0.51	-0.26	0.29	0.13
10	-0.11	0.00	-0.34	-1.10
Mean	-0.15	-0.10	0.08	-0.07
σ	0.35	0.34	0.37	0.61

Table 4-3 Reproducibility test for marker #2.

Frames Averaged	Marker #1: Deviation from Reference			
	6 MV		23 MV	
	x (mm)	y (mm)	x (mm)	y (mm)
16	0.00	0.00	-0.06	-0.04
32	0.00	-0.18	-0.29	0.44
48	0.00	0.00	0.00	0.00
64	0.00	0.00	0.00	0.00
80	0.00	0.00	0.00	0.00
96	0.00	0.00	0.00	0.00
112	0.00	0.00	0.00	0.00
128	0.00	0.00	0.00	0.00
Mean	0.00	-0.02	-0.04	0.05
σ	0.00	0.06	0.10	0.16

Table 4-4 Marker #1 positional accuracy.

Frames Averaged	Marker #2: Deviation from Reference 6 MV x (mm)	6 MV y (mm)	23 MV x (mm)	23 MV y (mm)
16	-0.40	0.26	-0.91	-0.53
32	-0.23	-0.09	0.29	0.13
48	0.17	-0.09	0.11	-0.13
64	-0.06	-0.22	0.23	-0.22
80	0.06	-0.18	0.23	-0.22
96	0.40	0.00	0.29	-0.26
112	0.11	0.00	0.11	-0.13
128	0.06	0.13	0.17	-0.13
Mean	0.01	-0.02	0.06	-0.19
σ	0.25	0.16	0.40	0.18

Table 4-5 Marker #2 positional accuracy.

Frames Averaged	False Positives 6 MV	23 MV
16	2	1
32	1	0
48	1	0
64	1	0
80	0	0
96	0	0
112	0	0
128	0	0

Table 4-6 The number of false positive marker detections in a background ROI.

Marker #	Deviation from Reference x (mm)	y (mm)
1	0.23	-0.13
2	0.34	-0.18
3	0.29	0.84
4	-0.34	-0.09
5	-0.63	0.09
Mean	-0.02	0.11
σ	0.44	0.42

Table 4-7 Evaluation of marker placement in clinical images.

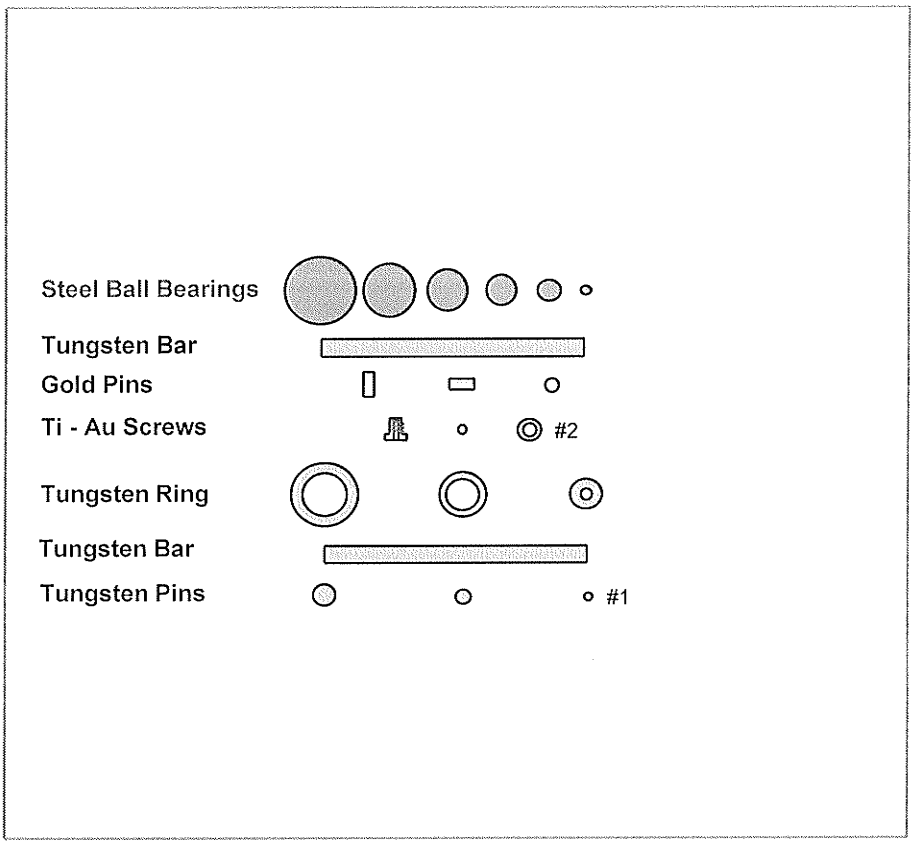

Figure 4-1 A schematic diagram of the contrast detail phantom.Markers labelled #1 and 2 were analyzed in this study. See text for the sizes of the radio-opaque markers.

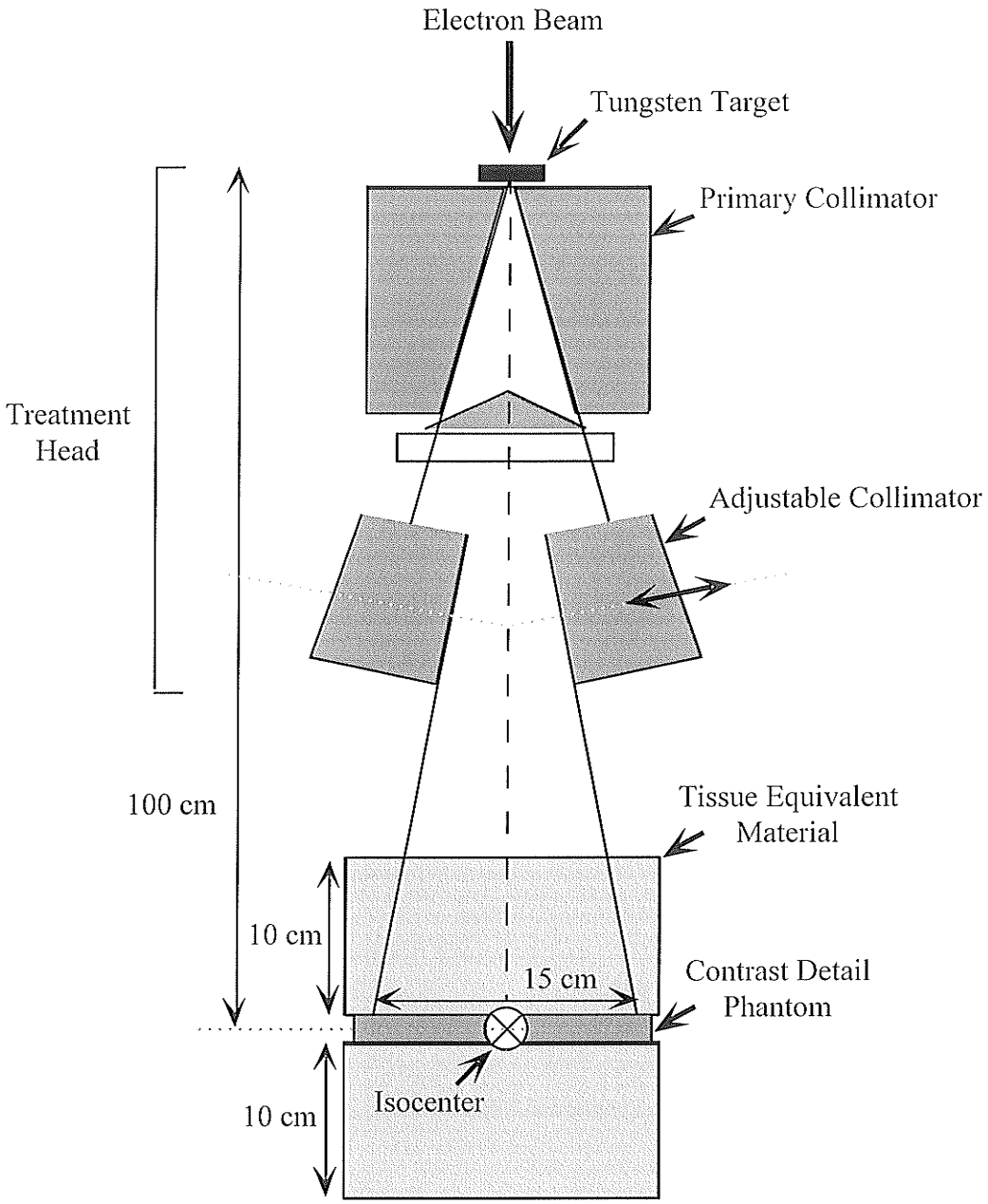

Figure 4-2 Images of the contrast detail phantom were acquired by placing it between two 10 cm blocks of tissue equivalent material and placing the center of the phantom at isocenter.

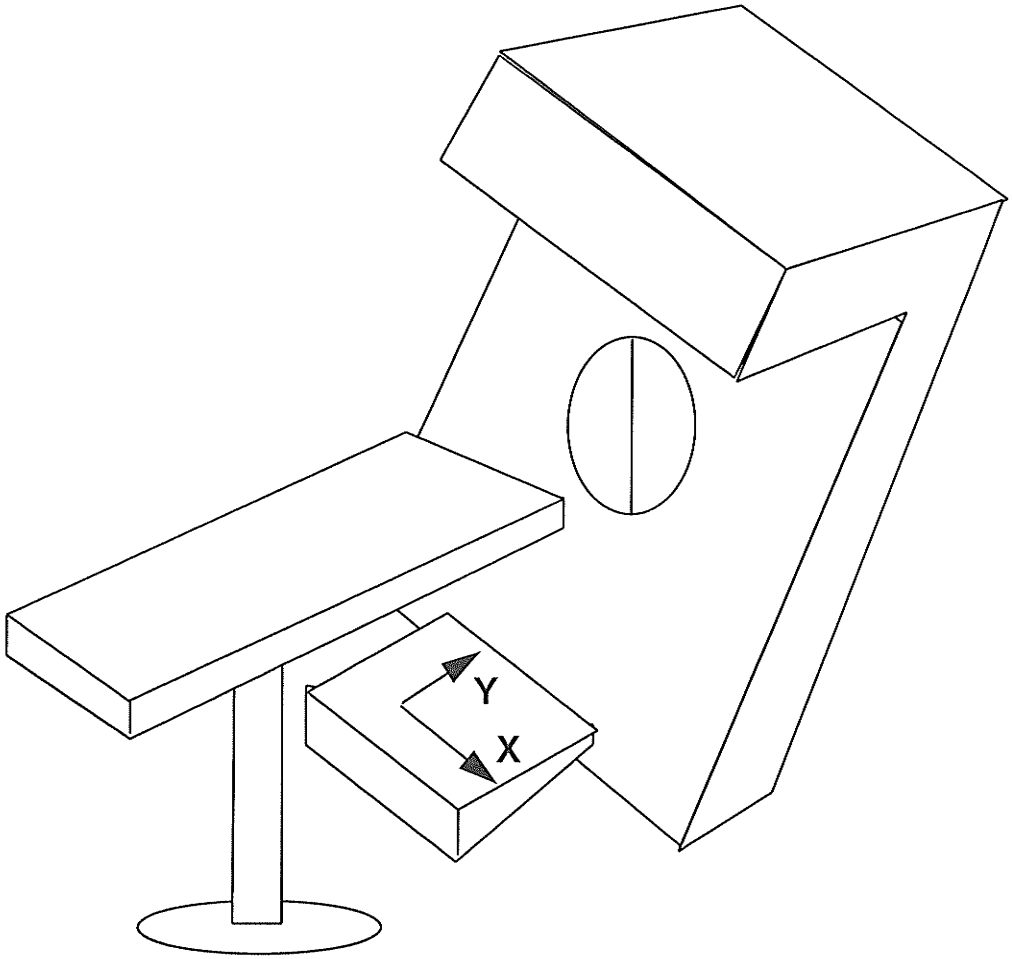

Figure 4-3 Deviations in the marker coordinates are measured with respect to a standard coordinate system used at our center.

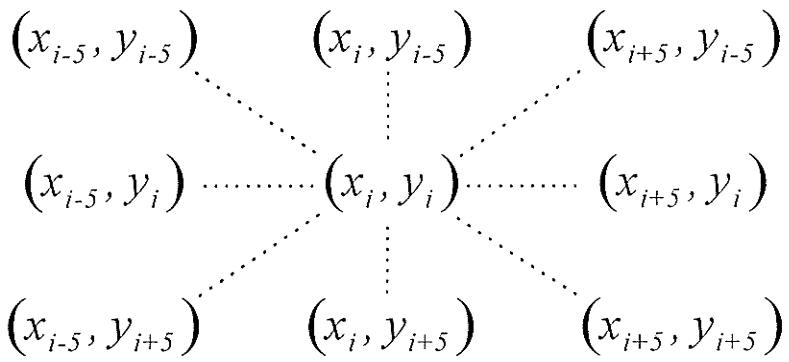

Figure 4-4 An 11 x 11 convolution mask used for detecting radio-opaque markers in megavoltage images.

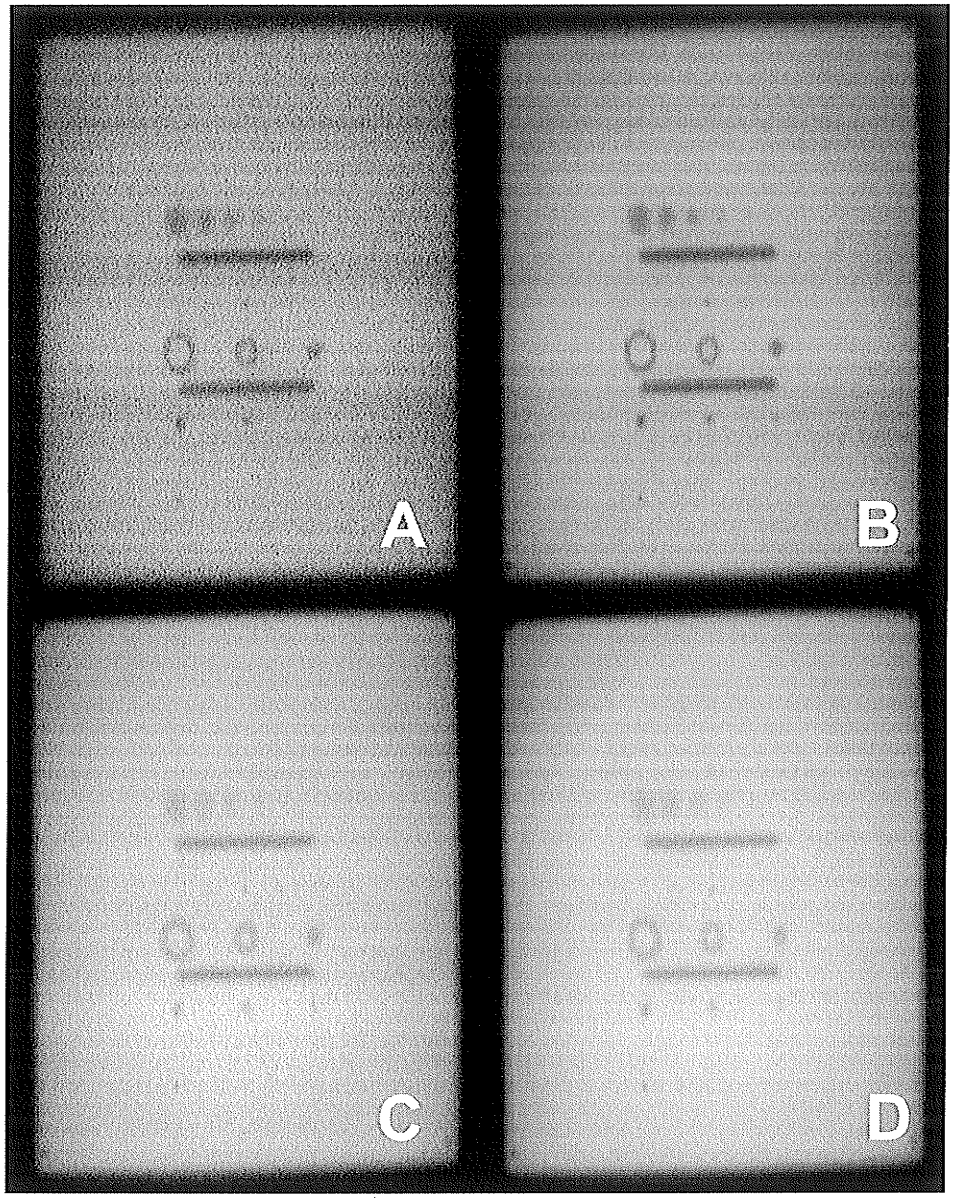

Figure 4-5 Images of the contrast detail phantom acquired at (A) 6 MV 1.46 cGy , (B) 6 MV 82.4 cGy, (C) 23 MV, 2.47 cGy and (D) 23 MV, 92.7 cGy.

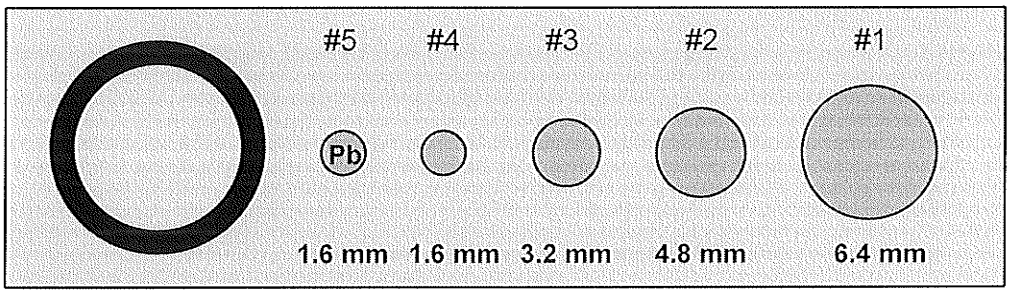

Figure 4-6 A small phantom containing 4 steel ball bearings with diameters ranging in size from 1.6 mm to 6.4 mm and 1 lead shot with diameter 1.6 mm. The phantom was placed on the skin of the patient just prior to treatment at an SSD of about 90 cm. The tungsten ring was used to mark absolute position of the other markers.

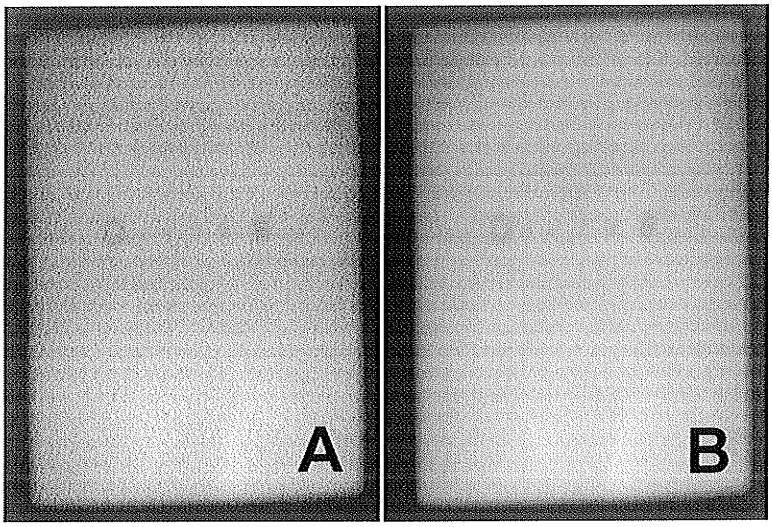

Figure 4-7 The clinical phantom was placed on the skin of a patient being treated for prostate cancer. (A) shows an anterior localization image acquired with about 1.2 cGy of dose. (B) shows the corresponding reference image acquired with 46 cGy of dose.

Chapter 5

Routine daily testing of radiation and light field congruence

5.1 Introduction

Radiation treatment machines, such as linear accelerators and cobalt units, employ a light field to delineate the position of the radiation field on the patient's surface. Since the light field is used for adjusting patient position prior to treatment, it must be a true predictor of the radiation field or else the treatment beam could be misdirected resulting in a suboptimal dose delivery to the target volume. Consequently rigorous quality control checks are mandatory to verify the congruence of the light and radiation fields and are routinely carried out on all treatment linear accelerators (linacs) usually on a monthly basis. With the increasing use of electronic portal imaging devices (EPIDs), it is becoming possible to use them, and their associated computers, to replace conventional methods for determining light/radiation field congruence. Conventionally ready-pack film is used for quality control tests of light/radiation field congruence. With the conventional method, the light field borders are marked on the film cover with a pencil, or by placing coins or other radio-opaque markers on the surface of the film, or by making pin holes through the cover and film. After exposure to the megavoltage beam, the film is developed, the light field edge marks are joined by ruler and pencil, and the radiation field edges are determined either visually or by scanning with a densitometer. Visual inspection of the film shows how well the radiation and light fields coincide, but not before considerable time and effort have been expended. Moreover, the conventional test is highly qualitative and interpretation of the results can be influenced by the radiation field penumbra, the symmetry of the field, the brightness and degree of blurriness of the light field, and the experience of the person performing the test[1].

A number of test tools have been proposed to improve the accuracy and reduce the labor of the light/radiation field congruence measurement. Freeman[2] used a 20x30 cm^2 radiolucent plate 2 mm thick into which a 15x20 cm^2 rectangle was engraved and filled with lead. Visual observance of the radiation field alignment with the rectangle indicated the degree of light/radiation field congruence. McCullough[3] designed an "edge tolerance test tool" consisting of a flat plate with imbedded lead markers which form shadows on the simulator or portal film, and can be used for visualization of the relative shift between the light and radiation fields. Double exposures were used to ensure that the markers could be seen on the portal films. Wielopolski et al.[4] proposed a fluorescent screen mounted on gimbals and viewed by a remote CCD camera. Images of both the light and radiation fields could be compared on a TV monitor. They suggested that computer analysis could be used to determine light/radiation field congruence, but do not report any results. Kirby[5] also proposed a gimbal-mounted test phantom consisting of a Perspex plate with inlaid lead wires which should be carefully aligned with the axis of rotation of the gantry. Their approach differs from Wielopolski's in that the plate is viewed by the video-based electronic portal imaging device (VEPID) mounted on the accelerator, which becomes part of the test apparatus. Images of the light field are acquired with the VEPID's fluoroscopic screen removed, and portal images of the radiation field are acquired with the screen installed. Visual inspection of the images permits the determination of any discrepancies between the light and radiation fields, as long as the EPID is stable while the screen is being changed.

The remainder of this chapter describes a semi-automatic test which provides an objective and quantitative measure of alignment between the light and radiation fields[6,7] which can be used with both VEPIDs and with scanning liquid ionization chamber portal imaging devices. The test consists of placing a special phantom at isocenter, aligning it to the

light field, and acquiring a megavoltage portal image with the VEPID. The image is analyzed automatically, and any misalignment is reported in terms of predetermined action levels indicating **"go"**, **"warning"** or **"no go"** decisions. In principle, images of the light field phantom could also be acquired on film, digitized and then analyzed in the same way, thus allowing treatment machines not equipped with an EPID to be checked. Two algorithms are compared and have been implemented on a PC computer for analyzing the phantom image and determining the light/radiation field congruence. The two methods differ in technique but give similar results when put through a rigorous test program. Routine daily testing is possible as the effort and time required for the automated techniques are minimal allowing the tests to be performed as part of daily quality assurance procedures.

5.2 Materials and methods

A light field phantom was constructed from a 17x17 cm^2 Delrin (Acetal) plate with a 15x15 cm^2 square inscribed on the upper surface. In the center and offset to each corner of the inscribed square of the phantom are 1/16" diameter tungsten pins angled to allow for beam divergence at isocenter. Figure 5-1 shows a schematic diagram of the light field phantom. The outer pins are numbered 1-4, while the Center pin is not used in the present study. This design is similar to the "edge tolerance test tool" described by McCullough[3], but the approach described here is original in that it uses an EPID to acquire a megavoltage image of the phantom, which is then analyzed automatically to determine the degree of light/radiation field congruence.

Testing was performed on a Siemens KD2 linear accelerator equipped with a BEAMVIEW^{PLUS} video-based electronic portal imaging system* at energies of 6 and 23

*Siemens Medical Systems, Concord, CA.

MV (dose rates of 200 and 300 cGy/min respectively). The experimental procedure consists of placing the light field phantom at isocenter and configuring the linac for a 15x15 cm^2 field. The phantom is manually adjusted so that the marks on its upper face coincide with the light field from the treatment accelerator. Electronic portal images of the phantom are acquired and transferred to a PC computer for analysis. The 8-bit images are 512x480 $pixels^2$, with each pixel representing about 0.6x0.5 mm^2 at isocenter. A Portal Image Processing System[8] (PIPS) has been developed to facilitate rapid analysis of the portal images. The software displays the magnitude and direction of any shift of the light field with respect to the radiation field in graphical form and issues warnings if the shift exceeds preset action levels. A recent AAPM Task Group Report[9] suggests that light/radiation field congruence should be within 2 mm on the field edge or 1% of the field width, therefore action levels of 2 and 4 mm are set to issue "**warning**" and "**no go**" decisions respectively.

The two algorithms were each tested for reproducibility, sensitivity to noise, and positional accuracy with respect to a known displacement. Daily light field congruence tests were conducted over a period of several weeks, and the test has also been compared to the conventional film method.

5.3 Image analysis

Comparison of the light and radiation fields requires an accurate and reproducible method to determine the location of each. The radiation field can be located in the portal image by a suitable edge detection algorithm, since the phantom is effectively transparent at megavoltage energies, and the edges of the beam collimators defining the field are clearly visualized. The position of the light field is determined by detecting the four outer pins, whose positions are known relative to the 13x13 cm^2 square marked on the surface of the

phantom which defines the light field. However, there are several different approaches that can be taken to detect the pins and compare their positions with the field edge and two algorithms have been developed in order to evaluate the influence of the mathematical method on the final results. Algorithm I uses the complete contour of the radiation field to determine its center of gravity, which is then compared to the center of gravity of the pins (and hence the light field). Algorithm II determines the distance from each pin to the nearest field edge. While algorithm I involves more data relating to the radiation field, its global approach may be somewhat sensitive to image distortions. Algorithm II, on the other hand, should be less sensitive to distortions, but may give a less accurate determination of the field edge. Hence the need for a comparison of the two approaches.

5.3.1 Algorithm I

The input for Algorithm I is an image of the light field test phantom. The 50% dose contour is mapped by searching for those pixels along the radiation field edge that are approximately half the maximum pixel intensity found on the image. The edge of the radiation field is traversed making use of an 8-directional chain code[10] to determine the previous and subsequent position of the contour until the curve closes on itself. The coordinates of the field contour (x_i, y_i), are recorded and are used to find the center of gravity (x_{cog}, y_{cog}) of radiation field,

$$x_{cog} = \frac{1}{n}\sum_{i=1}^{n} x_i \qquad y_{cog} = \frac{1}{n}\sum_{i=1}^{n} y_i \tag{1}$$

where n is the total number of contour points along the edge. The field contour coordinates are also used to find the area enclosed within the field edge[11] as a check to ensure that the proper field size is set on the linac.

The tungsten pins are detected by applying an 11 x 11 pixel gradient mask operation on a region of interest (ROI) around the expected pin location and each pixel is tested to determine which corresponds to a point on the pin. In a megavoltage image, pixels that correspond to the pin will be darker than the surrounding area, and can be found by checking if the gray value of the central pixel in the mask is less than the pixels in the neighborhood. The central pixel as shown in Fig. 5-2, is tested against the 8 pixels on the perimeter of the mask and if its value is the lowest it is marked as a candidate pin pixel.

Candidate pin pixels are eliminated if they are due to noise by checking if each marked pixel in the search region has at least 11 connected neighbors[10]. If not, it is deemed a noisy pixel and is removed from the list of candidates. The remaining marked pixels are used to determine the weighted center of gravity (x_p, y_p) of the pin:

$$x_p = \frac{\sum_{i=1}^{n}(255-m_i)x_i}{\sum_{i=1}^{n}(255-m_i)} \quad y_p = \frac{\sum_{i=1}^{n}(255-m_i)y_i}{\sum_{i=1}^{n}(255-m_i)} \tag{2}$$

where n is the number of marked pixels in the ROI about pin p, m_i, is the gray value, and (x_i,y_i) are the coordinates of marked pixels i respectively. The rationale for weighting the pixels is that darker pixels correspond to the central regions of the pin whereas lighter pixels lie on the edge of the pin and should be given less weight in determining the pins coordinates.

The coordinates of the four corner pins are used to determine the location of the light field. Two straight line equations are derived using the coordinates of each pair of diagonally opposed pins, with an intersection point (x_{int} , y_{int}). The displacement d of the light field with respect to the radiation field can then be determined from

$$(x_d, y_d) = (x_{int} - x_{cog}, y_{int} - y_{cog}) \tag{3}$$

$$d = \sqrt{(x_d^2 + y_d^2)} \tag{4}$$

where x_d and y_d are the coordinates of the displacement between the light field with respect to the radiation field. The four pin coordinates are also used to determine any rotation of the light field relative to the radiation field using a simple geometric calculation. A final check involves the peripheral distances between each of the outer pins which should be close to 130 mm, and any large deviation would indicate that a distortion may exist in the image and that the results may be invalid.

5.3.2 Algorithm II

The input for Algorithm II is an image of the light field test phantom. The coordinates of the field edge in a region near each of the tungsten pins are found by scanning either a horizontal or vertical line and searching for the pixel with maximal gradient along the line. Gradient is determined by applying a 3rd nearest neighbor mask to each pixel along the scan line. Therefore eight points along the field edge are found, two on each side of a square field. A straight line equation is derived from the two points on each side of the square and the intersection points of the four lines determines the approximate corner points of the field. A ROI is established inside each corner of the field and is searched for possible pin pixels.

The pins are detected by applying the gradient mask shown in Fig. 5-3, on each of the four ROIs. The method and reasoning for the pin detection is the same as for Algorithm I although the gradient mask is slightly different. A 7 x 7 cross mask is used (intersecting row and column each of 7 pixels) and if the gray value of the central pixel is less than the 4 pixels on the perimeter of the mask, it is considered to be a candidate pin pixel. In a method similar to that described for Algorithm I, the coordinates of all candidate pin pixels are filtered to eliminate pixels that are due to noise, which is indicated by less than four connected neighbors. The remaining marked pixels are used to determine the weighted center of gravity (x_p, y_p) of the pin,

$$x_p = \frac{1}{n}\sum_{i=1}^{n} x_i \qquad y_p = \frac{1}{n}\sum_{i=1}^{n} y_i \tag{5}$$

where n and (x_i, y_i) are the number and coordinates of the candidate pin pixels, respectively. Pin position with respect to the nearest field edge is determined by searching along horizontal and vertical scan lines from the pin to the field edge. The scanning lines are first smoothed with a 1x5 or a 5x1 averaging filter to reduce sensitivity to noise. The coordinate of the pixel (x_{max}, y_{max}) with maximum gradient along each scan line is recorded. The position vector of pin p from the nearest field edge is then given by,

$$(\delta x_i, \delta y_i) = (x_p, y_p) - (x_{max}, y_{max}) \tag{6}$$

where i=1, 2, 3, 4, correspond to pin 1, 2, 3, 4 respectively.

The phantom rotation is evaluated with respect to the field edge using the straight line edge equations and the coordinates of the tungsten pins. The four coordinates $(\delta x_i, \delta y_i)$

are corrected for any rotation before the phantom displacement is determined. The displacement d of the light field with respect to the radiation field is then given by,

$$(x_d, y_d) = \tfrac{1}{2}(\delta x_1 + \delta x_4 - \delta x_2 - \delta x_3, \delta x_1 + \delta x_2 - \delta x_3 - \delta x_4) \quad (7)$$

$$d = \sqrt{(x_d^2 + y_d^2)} \quad (8)$$

5.4 Results

A series of experimental tests was performed to evaluate the reproducibility, sensitivity to noise, and positional accuracy of both algorithms. In addition, daily measurements were carried out over a period of 84 days to test the methodology under routine clinical conditions.

Figure 5-4 is a typical PIPS screen display, showing the portal image of the phantom, the straight lines fitted to opposing diagonal pairs of pins, and the results window with a plot of the displacement. The two circles indicate the action levels at 2 and 4 mm.

5.4.1 Reproducibility

Reproducibility of both algorithms was tested by aligning the phantom in the light field of the linac and acquiring ten consecutive phantom images at 6 and 23 MV. No adjustments were made to the phantom position or linac between acquisitions, and any differences in the results must be due to the noise in the images, or to the manner in which the algorithms determine the field edge and pin positions. Table 5-1 shows the results for the test. For images acquired at 6 MV the largest standard deviation is 0.16 mm, and for 23 MV it is 0.34 mm. While the higher dose rate at 23 MV should reduce the

relative noise level, the wider beam penumbra will affect the accuracy of field edge delineation. There is no significant difference in reproducibility between the two algorithms.

5.4.2 Noise Sensitivity

The sensitivity of the two algorithms to noise was tested by generating a perfect phantom image by computer simulation and adding to it varying degrees of Gaussian noise. The perfect image consisted of a uniform square with simulated pins, and was blurred with a 5 x 5 averaging filter until a profile taken across the field edge closely approximated that of a typical portal image. The magnitude of the added noise should be similar to the noise present in typical portal images of the phantom, and this was determined by acquiring two similar images and performing an image subtraction[12] to eliminate contributions from fixed pattern noise and from low frequency background variations in pixel intensity. The variance of pixel values within a region of interest (ROI) in the subtracted image is given by,

$$\sigma_{sub}^2 = \sigma_1^2 + \sigma_2^2 \qquad (9)$$

where σ_1^2 and σ_2^2 are the noise variances in the two original images. If it is assumed that the two variances are equal, the standard deviation of the noise is therefore found from

$$\sigma = \frac{\sigma_{sub}}{\sqrt{2}} \qquad (10)$$

It was found that the standard deviation of noise in a typical portal image was equal to about 7 gray levels for images acquired at 6 MV and 6 gray levels for images acquired at 23 MV. With this in mind, Gaussian noise with standard deviations of 1, 2, 3, 4, 5, 6, 7, and 8 gray levels was added to the perfect image and all nine images were analyzed by both algorithms. Table 5-2 shows the results of the test. Algorithm I gives a mean deviation from the true value of 0.06 and 0.03 mm in the x and y directions respectively, with standard deviations of 0.05 mm. Algorithm II gives slightly poorer results, particularly in the x direction, where the mean deviation is 0.20 mm with standard deviation of 0.13 mm. This small sensitivity to noise in the image will have no significant effect on the results of a light/radiation field congruence test since the action levels are set at 2 and 4 mm.

5.4.3 Positional Accuracy

Positional accuracy was tested by aligning the phantom in the light field of the linac and acquiring an image in the usual manner. The phantom was then displaced a distance of 1 mm (measured with a micrometer) in the lateral direction and a second image of the phantom was acquired. This procedure was repeated for a total of 10 positions having displacements of -2, -1, 0, 1, 2 mm in both the lateral (x) and longitudinal (y) directions. The measured displacement of the light field with respect to the radiation field was normalized to the zero position and all other displacements were adjusted relative to this value. The measured, average and maximum displacements about the expected position are shown in Table 5-3. Algorithm I demonstrates mean deviations of 0.07 and 0.04 mm from the correct values in the x and y directions respectively, with a maximum of 0.11 mm. Again algorithm II gives slightly poorer results, with mean deviations of 0.19 and 0.20 mm and a maximum deviation of 0.34 mm. However even this maximum value is only about one half of a pixel width.

5.4.4 Daily Tests

The main goal of this work was to develop an objective and reproducible technique for rapidly checking light/radiation field congruence on a daily basis. The test is intended to be performed by radiation therapists as part of their routine daily QA before the start of treatments on each day. Preset threshold levels will warn the operator if alignment is unacceptable. Two threshold values for relative field displacements are set to 2 mm and 4 mm. If a measurement lies inside the 2 mm limit, a **"go"** decision is returned to the operator and treatments are permitted. If a measurement lies outside the 2 mm limit but within the 4 mm threshold, a **"warning"** is returned telling the operator that a misalignment in light/radiation field congruence has been detected and that the responsible physicist or service engineer should be notified. Treatments are allowed to continue in this situation. If a measurement lies outside the 4 mm threshold, a "**no go**" decision is displayed to the operator and no treatments are allowed until the treatment unit is serviced to correct the problem.

Light/radiation field congruence tests were performed at 6 and 23 MV on a daily basis over a 84 day trial period. Figure 5-5a shows the displacements determined by algorithm I at both energies, and Fig. 5-5b shows the results for algorithm II. The mean displacements for each algorithm, and the difference between the two algorithms, are given in Table 5-4. The standard deviations of the difference in x and y displacements were 0.19 and 0.13 mm at 6 MV and 0.13 and 0.11 mm at 23 MV. This shows that although the two algorithms use different methods to determine the field displacement, the results are in agreement with each other to an accuracy better than 0.2 mm. Note that although the phantom was not repositioned between image acquisitions at 6 and 23 MV, there is a shift in average displacements in the y direction of about 0.2 mm as measured

by both algorithms. The dependence of field displacement on energy may be due to a slight movement of the radiation beam focal spot at the different energies. The current fed to the focusing coils of the linac changes for each selected beam energy, and therefore a movement in the position of the focal spot is the most likely the cause of this shift. This observation suggests that light/radiation field congruence checks should be done at both energies of a dual energy machine.

5.4.5 The Conventional Film Method

It is natural to ask how the proposed automated test compares with conventional film measurements. Ten trials of the conventional film method were performed by an experienced dosimetrist to determine the light/radiation field deviation. Since the automated technique requires manual adjustment of the phantom in the light field, and since this is dependent on the skill of the operator, both an experienced medical physicist and experienced radiation therapist made ten measurements with the phantom. For each of these measurements the phantom was readjusted in the light field to simulate consecutive daily tests. The linac, collimators and light field were not adjusted throughout the entire test series. Images of the test phantom were acquired at an energy of 6 MV and displacements were analyzed with Algorithm I. The results of the comparison are summarized in Table 5-5 and show no significant differences between the conventional method and the automated method, or between the different operators. The spread of the mean displacements is 0.09 and 0.16 mm in the x and y directions respectively, with standard deviations up to 0.61 mm.

5.5 Conclusions

A quality control test has been developed which automatically determines the degree of congruence between the light and radiation fields using a video based electronic portal imaging device and a specially designed phantom. Two algorithms have been developed, and although they are different in their methodology, they both give similar results when compared to each other and to the conventional film method. Both algorithms determine known displacements with acceptable levels of accuracy, and both have been shown to be insensitive to noise in the images at levels likely to be encountered in portal imaging. The results indicate that algorithm I demonstrates superior performance in the sensitivity and reproducibility tests and similar performance to algorithm II in the reproducibility test. There was no significant difference in a comparison with film, and no significant difference when the phantom was placed in the light field by a physicist or a therapist. The results for the automated technique show that it is an acceptable replacement for the conventional film technique, with similar accuracy and greatly increased speed and convenience. The test requires only minutes to complete and returns a "**go**", "**warning**" or "**no go**" message to the operator depending on the measured deviation between the light and radiation fields. The objectivity, reproducibility and convenience of the automated test procedure should prove to be a benefit in routine quality assurance of the light/radiation field congruence.

References

1. A. Ho, B. Thomadsen and B. Paliwal, "On visual interpretation of light localization/radiation field coincidence films," Med. Phys. **22,** 237-238 (1995).

2. D. K. Freeman, "Testing coincidence of x-ray and light beam," Med. Phys. **11,** 78 (1984).

3. E. C. McCullough and K. P. McCollough, "Improving agreement between radiation-delineated field edges on simulation and portal films: The edge tolerance test tool," Med. Phys. **20,** 375-76 (1993).

4. L. Wielopolski, I. Waldman, I. J. Zedek and G. A. Bush, "A novel comprehensive quality control instrument for medical accelerators," Med. Phys. **22,** 799-801 (1995).

5. M. C. Kirby, "A multipurpose phantom for use with electronic portal imaging devices," Phys. Med. Biol. **40,** 323-34 (1995).

6. K. B. Luchka, G. Gluhchev, R. Rajapakshe, D. Chen and S. Shalev, "Assessing radiation and light field coincidence with an electronic portal imaging system", 3rd International Workshop on Electronic Portal Imaging, San Francisco, 1994.

7. S. Shalev, K. B. Luchka, G. Gluhchev and R. Rajapakshe, "A quality control procedure for light field accuracy", Proc. L. H. Gray Conference on Quantitative Imaging in Oncology, Newcastle-upon-Tyne, 1995.

8. S. Shalev, G. Gluhchev, D. Chen, R. Rajapakshe and K. B. Luchka, "Processing and analysis of portal images on a PC computer," Med. Phys. **22,** 1017 (1995).

9. AAPM Radiation Therapy Task Group No. 40, "Comprehensive QA for radiation oncology: Report of AAPM Radiation Therapy Committee Task Group 40," Med. Phys. **21,** 581-16 (1994).

10. R. C. Gonzalez and R. E. Woods, *Digital Image Processing,* (Addison-Wesley Publishing Company, New York, 1992).

11. H. Freeman, "On the encoding of arbitrary geometric configurations," IRE Trans. Elec. Comp. 260-68 (1961).

12. R. Rajapakshe and S. Shalev, "Noise analysis in real-time portal imaging. I. Quantization noise," Med. Phys. **21,** 1263-1268 (1994).

	Algorithm I				Algorithm II			
Energy (MeV)	X_m	σ_x	Y_m	σ_y	X_m	σ_x	Y_m	σ_y
6	-1.16	0.09	-0.77	0.09	-1.42	0.16	-0.52	0.06
23	-0.62	0.28	-0.53	0.20	-0.88	0.34	-0.34	0.24

Table 5-1. Reproducibility tests for 10 consecutive images of the light field phantom without adjusting the phantom position or linac between acquisitions. X_m and Y_m are the mean displacements in the x and y directions with standard deviations σ_x and σ_y.

	Displacement (mm)			
Added Noise	Algorithm I		Algorithm II	
	X	Y	X	Y
0	0.00	0.00	0.00	0.00
1	0.00	0.00	0.00	0.00
2	0.00	0.00	0.24	-0.10
3	-0.06	-0.05	0.33	-0.21
4	-0.15	-0.07	0.31	-0.09
5	-0.10	-0.05	0.28	-0.09
6	-0.07	-0.11	0.32	0.02
7	-0.06	-0.03	0.30	-0.11
8	-0.10	0.05	0.19	0.08
Mean	-0.06	-0.03	0.20	-0.06
σ	0.05	0.05	0.13	0.09

Table 5-2. Noise sensitivity tests were performed using a perfect phantom image with added Gaussian noise having deviations ranging from 0 to 8 gray levels.

True Displacement (mm)	Measured Displacement (mm)			
	Algorithm I		Algorithm II	
	X	Y	X	Y
2	1.97	2.09	1.84	1.87
1	0.91	1.05	1.02	0.75
0	0.00	0.00	0.00	0.00
-1	-0.97	-0.99	-0.77	-1.26
-2	-1.89	-2.00	-1.66	-2.16
Avg. Deviation	0.07	0.04	0.19	0.20
Max. Deviation	0.11	0.09	0.34	0.26

Table 5-3. Positional accuracy test for known displacements of the phantom.

	Algorithm I				Algorithm I				Algorithm (I - II)			
Energy (MV)	X_m	σ_x	Y_m	σ_y	X_m	σ_x	Y_m	σ_y	X_m	σ_x	Y_m	σ_y
6	-1.14	0.38	0.30	0.45	-1.13	0.31	0.22	0.44	0.01	0.19	-0.08	0.13
23	-0.86	0.35	0.50	0.43	-1.08	0.37	0.55	0.42	-0.22	0.13	0.05	0.11

Table 5-4. Results of daily tests performed over an 84 day test period. X_m and Y_m are the mean displacements in the x and y directions with standard deviations σ_x and σ_y.

	Dosimetrist		Physicist		Therapist	
	X	Y	X	Y	X	Y
Mean	-0.83	0.15	-0.92	-0.23	-0.90	-0.01
σ	0.61	0.34	0.40	0.32	0.24	0.55

Table 5-5. Comparison of the conventional film technique performed by a dosimetrist and the automated method applied by a physicist and a radiation therapist. Images of the test phantom were acquired at an energy of 6 MV and analyzed to determine displacement with algorithm I.

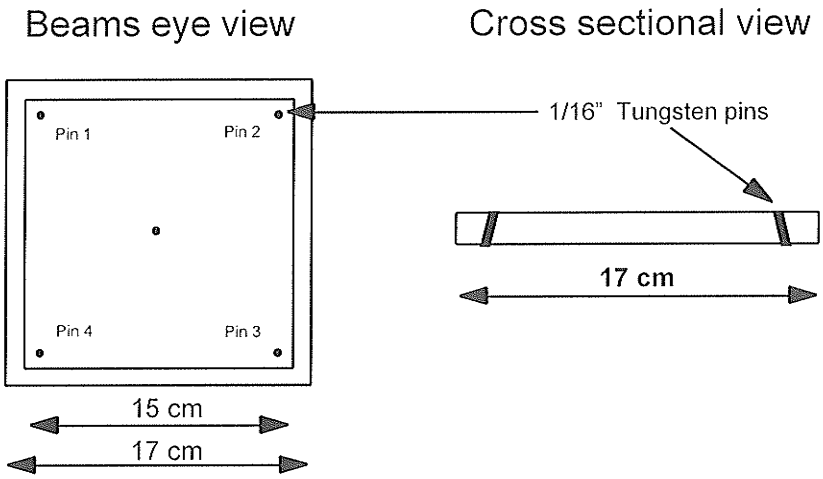

Figure 5-1 A schematic diagram of the light field phantom.

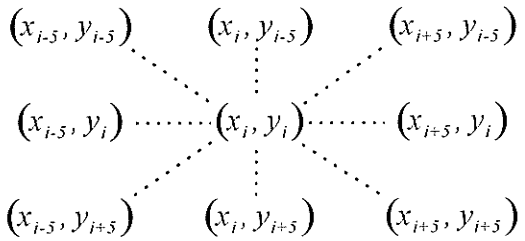

Figure 5-2 A 11 x 11 gradient operator mask used in Algorithm I.

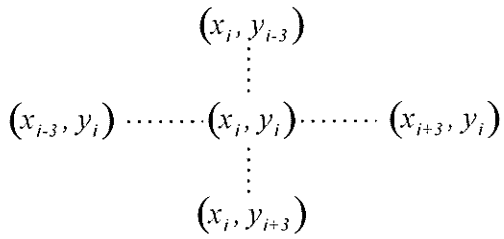

Figure 5-3 A 7 x 7 gradient operator mask used in Algorithm II.

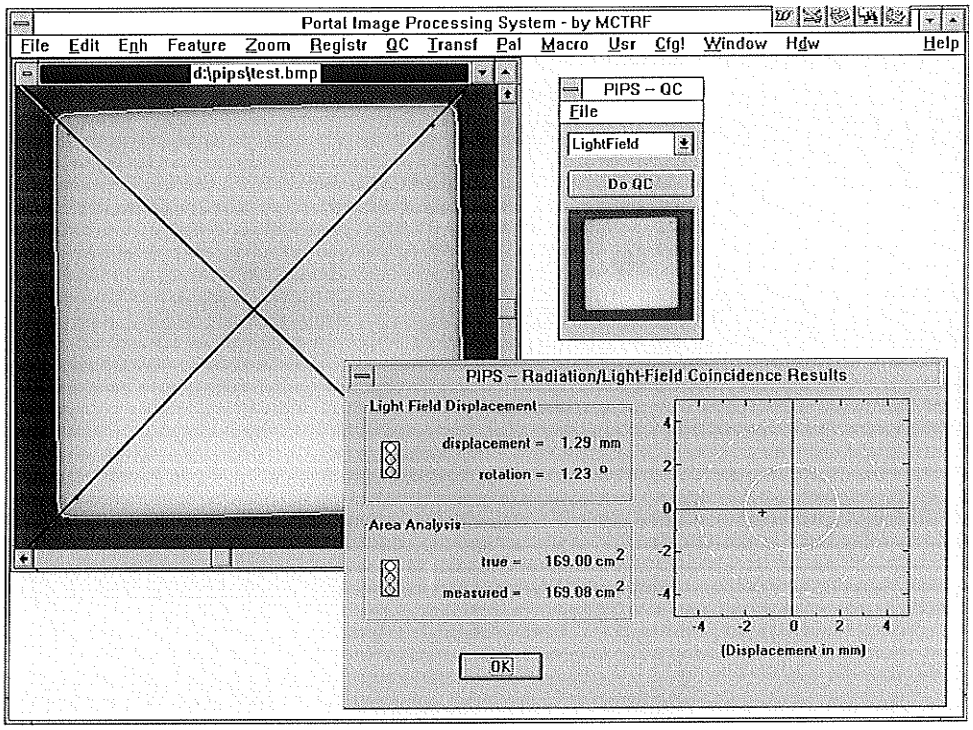

Figure 5-4 A typical screen display from the Portal Image Processing System showing the analysis of a light field phantom image and the graphical display of light/radiation field coincidence.

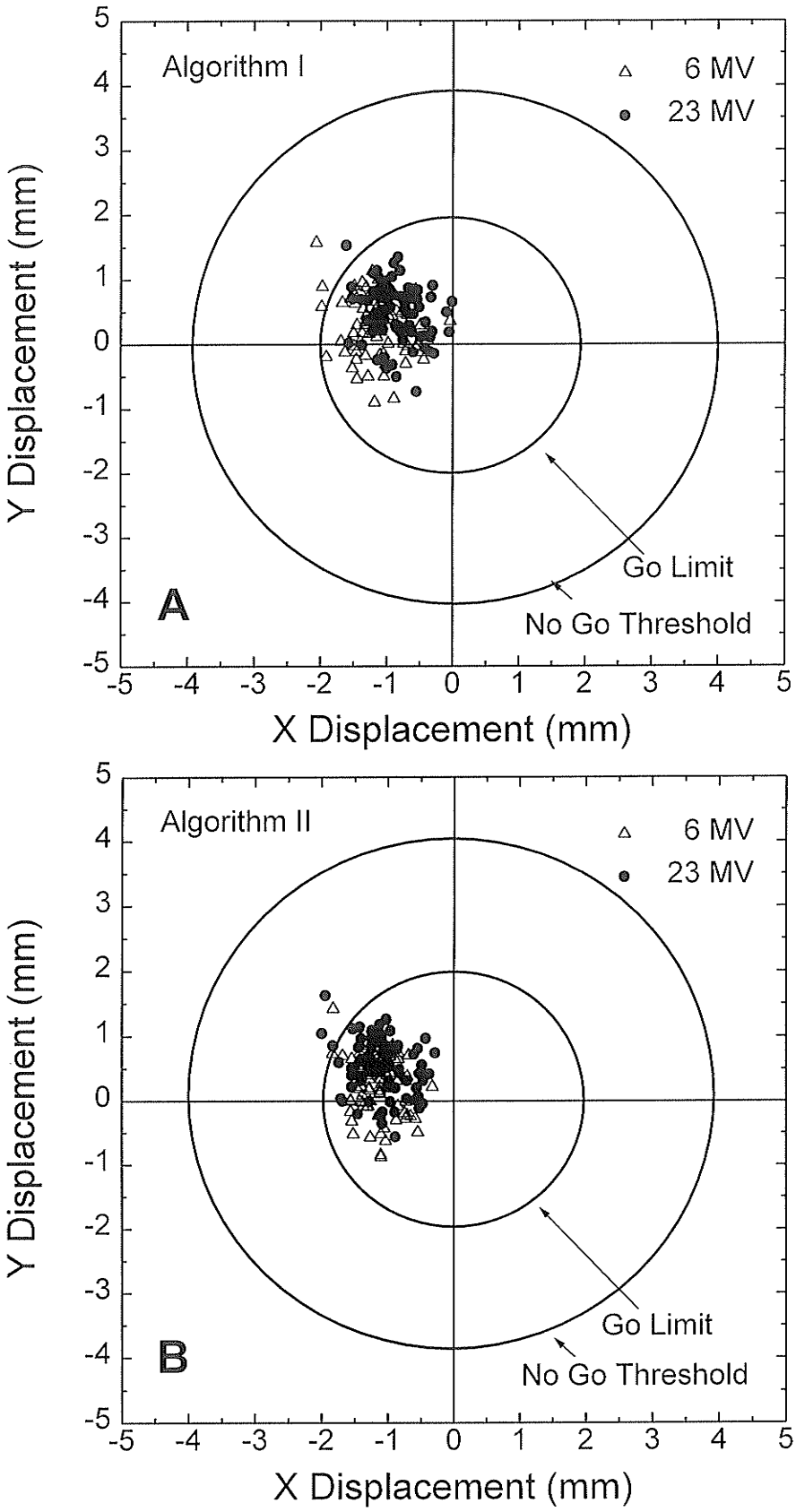

Figure 5-5 A two dimensional displacement plot recording radiation light field coincidence on a daily basis over an 84 day test period as measured by (A) Algorithm I and (B) Algorithm II. The two circles are have radii of 2 and 4 mm and determine the "Go" limit and "No Go" threshold for any measured displacement.

Chapter 6

Summary

The efficacy of radiotherapy ultimately depends on the dosimetric and geometric accuracy to which the target volume is irradiated over the course of treatment. Random and systematic positioning errors that occur during treatment setup may result in either under or over dosage to the tumor volume and surrounding normal tissue. Conventionally, treatment accuracy is monitored by comparing portal films of patient setup to diagnostic simulator films. However, due to the poor quality, high cost and increased work load associated with portal films, they are usually acquired on the first treatment fraction and possibly on a weekly basis thereafter.

A variety of electronic portal imaging devices (EPIDs) have been developed which facilitate routine monitoring of patient treatments by acquiring and displaying portal images in near real time with only a fraction of the daily dose of radiation allowing immediate corrective intervention to those treatment fractions showing unacceptable setup displacements.

Digital images and portal films both suffer from poor contrast due to the high energy x-rays that form them. However, the availability of digital data associated with the electronic images allows the possibility of rapid contrast enhancement through the use of

standard digital image processing techniques. Many image processing techniques have been applied to electronic portal images but with moderate success. This has prompted the development of a composite processing technique called "Sequential Processing" which has shown encouraging results when applied to megavoltage portal images. In this technique, a selective contrast limited adaptive enhancement technique is applied in combination with noise reduction and edge sharpening filters.

The "Sequential Processing" technique was optimized by analyzing images of a specially designed high contrast spatial resolution phantom. Optimization was performed on each stage of the technique using a figure of merit based on characteristics common to portal images such as spatial resolution, contrast and noise. It was found that optimized parameters for images acquired at 6 MV were different than those for images acquired at 23 MV. Although the optimized sequential enhancement technique showed a dramatic improvement to the contrast of clinical images at both treatment energies, a more detailed analysis is required to determine clinical efficacy of the procedure.

EPIDs are normally used for either inter-treatment evaluation of systematic setup errors or intra-treatment correction of random displacements and, in most cases, the current portal image is compared with a simulator film on which the prescribed field outline has been marked. However, in some circumstances it is not possible to acquire a simulation of the patient as in the case of very obese patients. An alternative approach, called Megavoltage Simulation, has been developed for this class of patient. Megavoltage

Simulation is carried out during the first treatment fraction with a radiation oncologist present to adjust patient setup by viewing a series of localization portal images. When the position is judged to be correct, a simulation portal image is acquired and the remaining treatment dose administered. This is repeated for each field. On subsequent treatments, the radiation therapists evaluate, and if necessary, adjust the patient's position by comparing localization images with the pre-approved "simulation" image.

Portal images were acquired throughout two courses of therapy of a 42 year old female diagnosed with stage IIb cancer of the cervix and who weighed 150 kg. After completion, all images were analyzed to determine the initial and corrected field displacements. It was found that the portal imager provided an adequate image quality for pelvic fields of patients with large separations and that skin marks can be unreliable when aligning obese patients in the treatment beam. It was also found that intra-treatment intervention increased the accuracy of target volume irradiation. Without corrections, 10% of the initial set up displacements would have been greater than 10 mm, 21% greater than 7 mm and 41% greater than 5 mm. With the application of intra-treatment corrections, only 2% of the displacements were greater than 10 mm, 11% were greater than 7 mm and 32% were greater than 5 mm. It was also found that the second field treated in a parallel opposed pair (i.e. anterior/posterior or left/right lateral) had lower setup displacements and did not require verification or correction. In the treatment of obese patients, the megavoltage simulation technique can replace conventional

techniques to ensure acceptable accuracy in the delivery of dose to the prescribed treatment volume.

Tumor volumes are not easily visualized in megavoltage images and therefore bony landmarks are commonly used as reference points when verifying patient setup assuming the position of the tumor remains fixed with respect to them. However this is not always the case as recent studies involving patients being treated for prostate cancer have shown. Large day to day variations were measured and found to be directly related to the level of rectal and bladder filling leading to increased doses to the rectum and bladder and a decreased doses to the prostate and seminal vesicles. This unpredictable movement has produced considerable interest into the use of radio-opaque implant markers to monitor boundaries of the prostate within the treatment field over the course of therapy.

A specially designed algorithm has been developed to detect radio-opaque markers in megavoltage portal images. Several radio-opaque markers were embedded into the phantom which was enclosed in 20 cm of tissue equivalent material to simulate treatment conditions. Images of the phantom were acquired with small doses of radiation and select markers were analyzed for positional accuracy as compared to a reference image. A clinical experiment was also performed by placing several markers on the skin of a patient being treated for cancer of the prostate. Images of this configuration were acquired and analyzed in the same manner as in the phantom tests. It was found that random noise was the largest contributing factor to deviations in the results returned from

the detection algorithm. However in both the clinical and phantom tests, sub-millimeter accuracy in marker position was attainable as measured from images formed with doses that are small fractions of those normally delivered in a typical treatment.

Eventually EPIDs will become standard equipment in all radiotherapy clinics and their applications will go beyond treatment verification. EPIDs can greatly simplify the routine quality assurance tests performed on treatment accelerators. One example is the testing of radiation light field coincidence. Projected light fields are used on treatment simulators and linacs to delineate the size and position of the radiation beam. Any discrepancy between these fields will lead to a systematic field placement error, with possibly serious implications with regard to the accuracy of the delivered dose distribution in the patient. Conventionally film has been used for regular quality control tests of light and radiation field congruence, but this is a time consuming method and is not suitable for daily checks. A new method has been developed that uses a specially designed test phantom, an EPID and a personal computer to test for radiation and light field congruence on treatment accelerators. The test phantom must be aligned in the light field of a treatment linac and imaged. A computer program then automatically analyzes the image and determines coincidence between the two fields. The final result of the test is a "go", "warning" or "no go" decision depending on the level of coincidence between the two fields. This automated method gives results comparable to the conventional film method and routine daily testing is possible as the effort and time required are minimal allowing the test to be performed as part of the routine start-up procedures.